Development of Qualitative and Quantitative Adverse Outcome Pathways for Acetylcholinesterase Inhibition Leading to Neurodegeneration

by

Dennis Sinitsyn

A Thesis Presented in Partial Fulfillment
of the Requirements for the Degree
Master of Science

Approved April 2023 by the
Graduate Supervisory Committee:

Karen Watanabe, Chair
Natalia Vinas
Stephen Wirkus

ARIZONA STATE UNIVERSITY

May 2023

ABSTRACT

Acetylcholinesterase (AChE) inhibition by chemical toxicants such as organophosphates, nerve agents, and carbamates can lead to a series of adverse health outcomes including seizures, coma, and death. An adverse outcome pathway (AOP) is a framework that describes a series of biologically measurable key events (KEs) leading from some molecular initiating event (MIE) to an adverse outcome (AO) of regulatory significance, all developed and hosted in the AOP Wiki. A quantitative AOP (qAOP) is a mathematical model that predicts how perturbations in the MIE affect KEs based on the key event relationships (KERs) that define the AOP. The purpose of this thesis was to expand upon the KERs that define the AOP for AChE inhibition leading to neurodegeneration in order to better understand the effects of AChE inhibitors and the risks they pose to ecosystems, wildlife, and human health. In order to reduce the resources and time spent for chemical toxicity testing, a qAOP was developed based on the available quantitative data and models that supported the AOP. A literature review for the collection of qualitative evidence and quantitative data in support of the AOP was performed resulting in further expansion of the relationships between key events (KERs) through construction of additional KER description pages. A model evaluation was performed by comparing the qAOP model predictions with experimental data, with a subsequent sensitivity analysis of unknown parameters. The qAOP model simulates the MIE through its fifth KE (KE 5) and KE 7. Model predictions compared to experimentally measured data either under- or overpredicting multiple KEs warranting additional refinement such as a formal parameter optimization. Overall, more data amenable to qAOP model development are needed. To aid qAOP model development, the presentation of data in the AOPWiki may be improved by presenting the quantitative data in the AOP Wiki in a tabular format and allowing for the hosting of mathematical models or raw data. With these recommendations in mind, and through continued AOP construction in the AOP Wiki, new qAOP models will be developed, ultimately supporting chemical risk assessment and the mitigation of effects upon exposed individuals and wildlife populations.

TABLE OF CONTENTS

Page

CHAPTER Page

LIST OF TABLES

LIST OF FIGURES

CHAPTER 1

DEVELOPMENT OF AN ADVERSE OUTCOME PATHWAY FOR ACETYLCHOLINSTERASE INHIBITION LEADING TO NEURODEGENERATION

1.1 Introduction

1.1.1 Inhibition of the Acetylcholinesterase Enzyme

Acetylcholine (ACh) is a neurotransmitter responsible for a variety of functions ranging from muscle contraction and heart function in the peripheral nervous system (PNS) to learning and memory consolidation in the central nervous system (CNS) (Kandel et al., 2013b). ACh initiates these processes through binding to either nicotinic (nAChRs) or muscarinic acetylcholine receptors (mAChRs). Maintaining proper concentrations of ACh is necessary to promote normal function, and removal of ACh from the extracellular space is primarily mediated by the enzyme acetylcholinesterase (AChE). Inhibition of AChE can therefore result in an accumulation of ACh and overactivation of ACh receptors, leading to symptoms ranging from difficulty breathing and fasciculations to seizures, coma, and death in the most severe cases (Sidell, 1994).

AChE can be inhibited by compounds such as organophosphates and carbamates. Organophosphates are potent inhibitors that cause irreversible AChE inhibition, while carbamates result in reversible inhibition (Čolović et al., 2013). Organophosphates are commonly used throughout the world in the form of pesticides, and a particularly hazardous set of organophosphates known as nerve agents, like sarin and soman, have been used in chemical warfare and terrorism (Yanagisawa et al., 2006). These compounds are capable of crossing the blood-brain barrier and irreversibly inhibiting AChE throughout the body and brain. Under *in vivo* conditions in rat models, the processes that occur following AChE inhibition can be separated into three phases. (i) Focal seizure onset and increased activity of cholinergic origin due to increased ACh. (ii) A transitory phase whereby spreading of the seizure affects other neurotransmitter systems like glutamate (Glu). (iii) The prolonged seizure activity becomes primarily non-cholinergic, ultimately becoming self-sustaining glutamatergically and can no longer be

attenuated with anticholinergic therapy (McDonough & Shih, 1997). Prophylactic treatment with reversible cholinesterase inhibitors for military personnel or early post-exposure treatment with atropine, a mAChR antagonist, for affected individuals can prevent the pathology from occurring. The treatment options, however, are limited, as atropine will only be successful if used within 10-15 minutes post-exposure, and there are few viable treatment options for longer untreated exposure periods (McDonough & Shih, 1997). Decreasing levels of brain AChE activity leads to an accumulation of ACh and a cascade of events that ultimately result in seizure activity as well as neurodegeneration and death (McDonough & Shih, 1997). AChE inhibitors such as these introduced into the environment pose risks to both human health, wildlife, and ecosystems. They can impact an organism's health through multiple biological pathways and understanding their effects on a population or individual level is necessary to evaluate their risk, as well as to successfully provide treatment options to those exposed to the chemical(s).

1.1.2 Adverse Outcome Pathways

Adverse Outcome Pathways (AOPs) were created to collect and organize information about toxicants' effects on organisms and biological pathways. Through this process of collection and organization, AOPs help us understand how changes at the molecular level initiate impacts on higher levels of biological organization. This framework facilitates both ecological and human health risk assessment for regulatory decision making and identifying potential effects upon individuals (Ankley et al., 2010). Given the serious consequences of AChE inhibition, an AOP for AChE inhibition leading to neurodegeneration (AOP 281) was developed by integrating existing information into a conceptual model that best describes these linked biological pathways. In doing so, this AOP will result in a better understanding of and ability to predict adverse effects of AChE inhibitors.

AOPs are available on the AOP Wiki, a website that stores and organizes the available information on AOPs in a wikilike format (Society for Advancement of AOPs, 2022). As per the Organization for Economic Co-operation and Development (OECD) User Handbook (OECD, 2018), an individual AOP is defined by a modular sequence of events and the relationships

between them, known as Key Events (KEs) and Key Event Relationships (KERs), respectively. An AOP begins with a KE known as the Molecular Initiating Event (MIE), a specific KE that involves a chemical toxicant's interaction with biology at the molecular level of organization. An AOP is built with KEs that progress toward increasing levels of biological organization, going from the molecular level to cells and tissues, organs and organ systems, and finally the individual and population (OECD, 2018). KEs ultimately lead to the final KE in the AOP known as the Adverse Outcome (AO), which describes an effect of regulatory relevance, such as an overall reduced reproductive capacity for a population or a disease state for an individual (OECD, 2018). KEs are specific biological responses in an organism that are both measurable and essential to an AOP. In an AOP, KE essentiality is defined as the ability to prevent or block subsequent (downstream) KEs and the AO by preventing or blocking the preceding (upstream) KE (OECD, 2018). A KER describes changes in a downstream KE in response to changes in an adjacent upstream KE, such as increased receptor activation (downstream KE) in response to increases in neurotransmitter concentration (upstream KE). These KEs and KERs are housed in the AOP Wiki in the form of description pages. KE and KER description documents summarize the processes and evidence, such as the methods used for KE measurement and its biological domain of applicability (taxonomic, life stage, and sex relevance), in support of the KE or KER. The AOP Wiki and the OECD User Handbook (OECD, 2018) also provide templates and guidelines to assist in the efficient development of an AOP (Society for Advancement of AOPs, 2022).

The AOP development process involves determining the most suitable KEs and KERs that define an AOP and is based on two factors that ultimately shape the final AOP conceptual model: (i) What is currently known about the involved biological pathways and (ii) what quantitative data are available that supports the specific relationship between two KEs. Compiling this information required an extensive literature review through available databases and search engines. Prior to my involvement in the development of AOP 281, a substantial amount of this work and development had already begun. Over 200 papers had been reviewed and collected for its development, with the KEs and KERs having been constructed (Conrow et al., 2019, 2020).

Figure 1.1 shows the prior iteration of the conceptual model describing AOP 281, which includes the MIE, 8 KEs, the AO, and 10 corresponding KERs. KER 1 is AChE inhibition leading to an excess of ACh in the synapse. KER 2 involves the accumulated ACh overactivating mAChRs within the brain. KER 3 involves the overactivated mAChR initiating focal seizures. KER 4 is the occurrence of focal seizures leading to increased glutamate. KER 5 involves the increased glutamate leading to overactivation of n-methyl-D-aspartate (NMDA) receptors. KER 6 involves the overactivated NMDA receptors leading to an excess of intracellular calcium. KER 7 is the excess intracellular calcium leading to status epilepticus. KER 8 involves status epilepticus resulting in a further release of glutamate, forming a positive feedback loop. KER 9 involves the excess intracellular calcium leading to cell death. Lastly, KER 10 involves the cell death leading to overall neurodegeneration in the brain. While the conceptual model had been created, AOP 281 development was still under progress, and necessitated further literature review and expansion of its KER description pages. As work on individual KEs have been done prior to my entry on the development of AOP 281, the KE information later in the chapter will be a brief summary of what is currently available in the AOP Wiki (Society for Advancement of AOPs, 2022).

Due to the AOP Wiki format, multiple authors with diverse scientific backgrounds may contribute to an AOP throughout its development, making it a collaborative process. Additionally, an AOP's modularity allows its KEs and KERs to be used by multiple AOPs as many biological pathways may intersect at one or even multiple points. In the context of AOP 281, this modularity allowed for modification and reuse of descriptions for both KER 1 (AChE inhibition leading to ACh accumulation), and KER 10 (Cell death leading to neurodegeneration) as seen in Figure 1.1. Additionally, reuse without modification of a description is also possible. For the current AOP (Figure 1.2), the material on the description pages for KERs 1 and 11 was written by authors unaffiliated with AOP 281, however owing to the modular nature of AOPs, the information provided in these KERs fit well for usage in AOP 281, although additional quantitative evidence was included in KER 1. Finally, the OECD handbook refers to AOPs as "living" documents that

grow or evolve over time (OECD, 2018). This applies to AOP 281 as well, as there have been multiple iterations of this AOP prior to the current conceptual model, with the most recent modification taking place in October of 2022 (see Figure 1.2). As new data become available, the sequence of KEs or KERs that define an AOP may change to adapt to the new information.

The additional work that led to the current conceptual model was motivated primarily by the need for quantitative data for the development of a quantitative AOP (qAOP); a mathematical model that would allow for the extrapolation of *in vitro* data to make predictions on the likelihood and severity of the AO in response to a measurable perturbation in the MIE. The qAOP and its development are discussed in Chapter 2. The section that follows describes the additional literature review conducted, methodologies for KER description development, and the adjustments that resulted in the most recent conceptual model.

1.2 Methods

1.2.1 Literature Review

A review of the available qualitative evidence and quantitative data in support of the KERs was conducted through databases and search engines such as Scopus, PubMed, and Google Scholar. The general searching strategy for each KER employed the use of variations of keyword pairs for adjacent KEs, such as “Status epilepticus” and “Calcium”, or “Generalized seizure activity” and “Calcium”. The search criteria remained general and was not limited to a specific timeline or set of journals. In certain instances, references from the present literature review and previously compiled papers led to the identification of additional suitable papers. Acceptable qualitative evidence for a KER includes studies which demonstrated a cause-and-effect relationship between the KE pair and included papers such as gene knock-out studies and receptor antagonist experiments which prevented the downstream KE. Acceptable quantitative data for KERs included dose-response or time-series data, computational models that predict changes in at least two adjacent KEs, and any values describing relevant enzyme and receptor-ligand kinetics for the appropriate KEs. Papers providing data for two or more non-adjacent KEs

were also collected for use in later quantitative AOP (qAOP) model development and evaluation, which is described in more detail in the next chapter.

The overall collection and organization of the articles were managed both through EndNote (The EndNote Team, 2013) and a shared Microsoft® Excel spreadsheet. Appendix A contains the spreadsheet and the collection of articles gathered during the literature review. The spreadsheet ordered articles depending on the KEs for which they provided information, as it contained columns for each KE in the AOP. Additional columns included the type of paper, chemicals, species, sex, age, exposure route and duration, and the tissue sample used if applicable. The spreadsheet's layout made determining the quantity of data available for any KER simple as the articles could be sorted by individual KEs.

1.2.2 Methods for AOP Development for the AOP Wiki.

The available scientific evidence gathered from the literature review was assembled into KER description pages according to the template and practices outlined in the OECD User's Handbook (OECD, 2018). The KER description sections were written to provide a brief overview of the relationship between the two KEs and includes information that was not otherwise provided in the individual KE descriptions. Biological plausibility sections were written to include information about what is known of the biology regarding the relationship, such as describing the function of AChE and its hydrolysis of ACh, while the empirical evidence section included any support for the KER such as cause-and-effect relationships. Experimental evidence or knowledge that conflicted with support for the KER were included in the uncertainties and inconsistencies section. A more detailed explanation of the sections can be found in the OECD User's Handbook (OECD, 2018). Additionally, when possible, a table of quantitative data was prepared containing a data summary following the recommendations outlined in Sinitsyn et al. (2022), and included information on which methods were used to measure each KE, the species utilized, and a brief summary of the data for each reference. The table also included previously developed mathematical models that encompassed at least the two related KE pairs for the KER as these facilitated qAOP model development.

Specialists in the field were brought in to review the construction of the AOP and through its most recent iteration. KER 7 from Figure 1.1 was discovered to lack literature evidence, and as a result I consulted with Demetrio Raldua, PhD (Institute of Environmental Assessment and Water Research, Spain) and Joyce Rohan, PhD (US Army Core of Engineers, Dayton, OH) to make appropriate modifications to the AOP. Specifically, a revised set of KERs were needed to better describe the biology, and as a result, adjustments to the set of KERs were made based on expert advice (D. Raldua, J. Rohan, personal communication, October 3, 2022).

1.3 Results

1.3.1 Literature Review

In total, I gathered and reviewed over 75 papers for the AOP, bringing the total to over 275 papers reviewed for its development. Both *in vivo* and *in vitro* evidence covered a broad variety of species and included human, cow, pig, fish, and bird data, however the majority of articles gathered involved rodents, primarily rats, in addition to mice, hamsters, and guinea pigs. While there was a relatively moderate amount of qualitative evidence to support each KER, there was significantly less quantitative data available.

1.3.2 AOP 281: AChE Inhibition Leading to Neurodegeneration

The current conceptual for AOP 281 is shown in Figure 1.2. KER 7 in Figure 1.1 was removed, and the current KERs 6 (NMDA receptor activation leading to SE) and 9 (SE leading to increased intracellular calcium) were added in its place as they were more suitable to support the AOP based on the existing evidence. Additionally, the KER numbering post-KER 5 was modified to account for these changes. NMDA receptor activation leading to increased intracellular calcium is now KER 8 while increased intracellular calcium leading to cell death and ultimately neurodegeneration is now KERs 10 and 11, respectively. KER 6 was created as evidence shows that NMDA receptor antagonism can prevent soman-induced status epilepticus (Sparenborg et al., 1992). KER 9 was created as NMDA receptor activation is not the only mechanism through which calcium influx into the neuron occurs, as channels such as voltage-dependent calcium

channels (VDCC) and release from intracellular calcium stores have also been shown to be involved (Deshpande et al., 2010; Deshpande et al., 2014; Pal et al., 1999). Further details on KER 6 and 9 can be found later in this chapter and in Appendix B.

In total, I produced three KER descriptions (KERs 5, 6, and 9) for AOP 281 and either edited or modified seven of the remaining KER descriptions by providing additional information or including a table of quantitative data pertinent to that particular KER. Listed below are summaries of the descriptions of the KEs and KERs that comprise the AOP. Appendix B contains the drafts of the KER descriptions I produced.

AChE Inhibition (MIE). AChE is an enzyme primarily responsible for the regulation of the neurotransmitter ACh and does so by removal of the transmitter from cholinergic synapses through hydrolysis (Kandel et al., 2013b). AChE is found in both the PNS and CNS and is involved in the regulation of muscle activity and neurological processes (Kandel et al., 2013b). AChE is inhibited by inhibitors such as organophosphates and carbamates, and results in permanent and reversible inhibition, respectively (Fukuto, 1990).

Acetylcholine Accumulation in Synapses (KE 1). ACh is a neurotransmitter found in both the PNS and CNS. It is released from neurons during an action potential and diffuses across cholinergic synapses to bind to either ionotropic nAChRs or metabotropic mAChRs, which ultimately results in the stimulation of the post-synaptic neuron or neuromuscular junction of muscle fibers receiving the ACh signal (Kandel et al., 2013b). Therefore, accumulation of ACh in these synapses can cause overstimulation of the affected neuron or muscle fiber through excess binding of ACh onto cholinergic receptors.

Activation of Muscarinic Receptors (KE 2). The mAChRs are a set of G-protein coupled metabotropic receptors of either excitatory or inhibitory subtypes, labeled M1 through M5 (Hulme et al., 1990). M1, M3, and M5 are considered excitatory while M2 and M4 mAChR are considered inhibitory with regard to modulation of neuron excitability (Haga, 2013). In the context of AOP 281, preventing the activation of mAChR through antagonists such as atropine were

demonstrated to reduce symptoms of organophosphate poisoning, and is used as standard treatment in conjunction with AChE reactivators (McDonough & Shih, 1997).

Occurrence of Focal Seizure (KE 3). The start of a focal seizure begins with excessive and hypersynchronous activity located within a small group of neurons in a localized region of the brain, called the focus (Kandel et al., 2013a). The affected neurons of the focus are in a hyperexcitable state and are more likely to fire in response to excitatory input. Initially, seizure activity is limited to a small region due to successful inhibition of the hyperexcitable neurons by neighboring inhibitory neurons, called the inhibitory surround (Kandel et al., 2013a). Failure of the inhibitory surround ultimately results in spreading of the seizure, a process known as secondary generalization (Kandel et al., 2013a).

Increased Glutamate (KE 4). Glu is an excitatory neurotransmitter and binds to both ionotropic and metabotropic receptors in the CNS and PNS. Ionotropic glutamatergic receptors include α-amino-3-hydroxy-5-methyl-4-isoxazolepropionic acid (AMPA) receptors, kainate receptors, and N-methyl-D-aspartate (NMDA) receptors (Kandel et al., 2013b). Increased extracellular Glu in the synapse can be a product of excessive activity such as during seizures (Lallement et al., 1992). Excessive extracellular Glu overstimulates the affected neurons through overactivation of glutamatergic receptors.

Overactivation of NMDA Receptors (KE 5). NMDA receptors are ligand and voltage-dependent ionotropic receptors. To fully activate, NMDA receptors require both Glu and glycine as ligands, and depolarization of the membrane to which the receptors are bound in order to release Mg^{2+} from the channel. NMDA receptors are unique relative to the other ionotropic Glu receptors as they are also permeable to Ca^{2+} and upon activation are responsible, in part, for calcium influx into the post-synaptic neuron (Choi, 1988).

Status Epilepticus (KE 6). After focal seizure onset, a seizure may progress by spreading throughout the brain and fail to terminate. Status epilepticus (SE) is defined as a condition of continuous seizure activity or intermittent seizure activity without recovery lasting for more than 5 minutes (Lowenstein & Alldredge, 1998). Status epilepticus induced through AChE inhibition is

unresponsive to anticholinergic treatment, showing the process is instead self-sustained through glutamatergic mechanisms (Lallement et al., 1999; McDonough & Shih, 1997).

Increased Intracellular Calcium Overload (KE 7). Intracellular Ca^{2+} acts as a secondary messenger for a variety of cellular functions, ranging from gene transcription and cellular development to controlled cell death through apoptosis (Berridge, 2012). Therefore, Ca^{2+} homeostasis is an integral and tightly regulated conserved process in cells (Case et al., 2007). Dysregulation of intracellular calcium and increasing concentrations beyond what the cell or neuron is capable of managing can lead to excitotoxic outcomes (Sattler & Tymianski, 2000).

Cell Injury / Death (KE 8). Cell death can be separated into multiple categories which include apoptosis and necrosis, with each event containing distinct morphological features. Apoptosis involves cellular shrinkage and fragmentation, while necrosis includes cellular swelling and lysis (Kroemer et al., 2009).

Neurodegeneration (AO). While cell death can be considered a form of neurodegeneration, this outcome also pertains to a more general loss of neuron structure and function. Neurodegeneration can be seen in many notable diseases such as Huntington's, Alzheimer's, Parkinson's disease, and amyotrophic lateral sclerosis (ALS), all of which are characterized by progressive neurodegeneration (Przedborski et al., 2003). Examples that do not include cell death are morphological changes in neurons such as distorted shape and size (Przedborski et al., 2003).

AChE Inhibition leads to ACh Synaptic Accumulation (KER 1). There is a significant amount of evidence in multiple species that demonstrates accumulation of ACh after AChE inhibition. For example, *in vivo* time-series data provides a dose-response relationship between AChE activity and ACh and show that AChE inhibition through a variety of inhibitors results in the progressive accumulation of extracellular ACh (Kosasa et al., 1999). Additionally, pharmacokinetic data and multiple pharmacokinetic/pharmacodynamic (PKPD) models are available that simulate the time-course and concentration of AChE inhibitors and predict changes in free AChE throughout their compartments (Chen & Seng, 2012; Maxwell et al., 1988).

ACh Accumulation leads to Activation, mAChRs (KER 2). With accumulation of ACh comes excessive binding of post-synaptic receptors. In the context of AOP 281, mAChRs are at the center of organophosphate poisoning through ACh accumulation. Quantitatively, binding kinetics for ACh on mAChRs have been determined through radiolabeled assays, and computational models have been developed that show neuronal responses to activation of M1 mAChRs using ACh (Kellar et al., 1985; Mergenthal et al., 2020; Uchida et al., 1978).

Activation, mAChRs leads to Occurrence, Focal Seizure (KER 3). Activation of excitatory mAChRs result in enhanced excitability of the post-synaptic neuron through inhibition of the M-current, a voltage-dependent K^+ current responsible for modulation of cellular excitability (Marrion, 1997). In the case of AOP 281, it is overactivation of the M1 subtype by which the pathology progresses. This has been demonstrated in experiments where transgenic mice lacking M1 mAChR show resistance to seizure activity in response to administration of pilocarpine, an mAChR agonist (Hamilton et al., 1997). In another experiment, pretreatment with pirenzepine, an M1-specific antagonist, prevented cholinergically induced seizure activity (Cruickshank et al., 1994).

Occurrence, Focal Seizure leads to Increased, glutamate (KER 4). Upon firing, glutamatergic neurons release glutamate. In cases of excessive and hypersynchronous activity such as during seizure activity, there is increased Glu release, with experiments showing increasing levels of extracellular Glu after the start of cholinergically induced seizure activity (Lallement et al., 1991). More recent quantitative experimentation of seizure induction through various methods (Meurs et al., 2008; O'Donnell et al., 2011) measures both seizure activity through EEG and Glu dialysate through microdialysis experiments.

Increased, glutamate leads to Overactivation, NMDARs (KER 5). As NMDA receptors are glutamatergic, it follows that increased Glu results in increased binding of NMDA receptors. Michaels and Rothman (1990) showed that excessive Glu is excitotoxic to neurons and results in cell death. More specifically, they demonstrated that it was mediated through NMDA receptor

activation as dizocilpine (MK-801), an NMDA receptor antagonist, prevented said cell death (Michaels & Rothman, 1990).

Overactivation, NMDARs leads to Status epilepticus (KER 6). Continuously sustained seizure activity is considered to become status epilepticus after lasting longer than five minutes (Lowenstein & Alldredge, 1998). NMDA receptor activation has been demonstrated to be involved in this extended seizure activity that ultimately leads to status epilepticus. For example, in status epilepticus induced models of seizure activity, NMDA receptor antagonists such as ketamine or MK-801 were used to terminate seizures (Borris et al., 2000; Braitman & Sparenborg, 1989; Sparenborg et al., 1992).

Status epilepticus leads to Increased, glutamate (KER 7). As status epilepticus is prolonged seizure activity, this KER is similar to the previously defined KER 4. In the context of AOP 281, KER 7 is separate from KER 4 based on the length of time since seizure activity, spreading of seizure activity from focal to generalized, and lastly that seizures during the phase of status epilepticus appears to be resistant to anticholinergic therapy (McDonough & Shih, 1997).

Overactivation, NMDARs leads to Increased, Intracellular Calcium overload (KER 8). There is a considerable amount of evidence associating NMDA receptor activation and calcium influx. For example, in an *in vitro* experiment it was shown that activation of NMDA receptors using either NMDA or Glu resulted in increased intracellular calcium, with the change in calcium absent under extracellular Ca2+ free conditions (Liu et al., 2013). Similarly, in another *in vitro* experiment, increases in intracellular calcium using Glu was prevented with pre-treatment of MK-801 (Michaels & Rothman, 1990). Quantitatively, there have been models developed that simulate calcium influx upon NMDA receptor activation in dendritic spines (Hu et al., 2018).

Status epilepticus leads to Increased, Intracellular Calcium overload (KER 9). Intracellular calcium increases during status epilepticus through a variety of mechanisms, such as NMDA receptor activation, VDCCs, and release from intracellular calcium stores (Deshpande et al., 2010; Deshpande et al., 2014; Pal et al., 1999). Additionally, intracellular calcium levels appear to remain elevated days later following status epilepticus onset (Raza et al., 2004). Intracellular

calcium levels have been shown to increase through *in vitro* models of status epilepticus as well (Nagarkatti et al., 2010; Pal et al., 1999).

Increased, Intracellular Calcium overload leads to Cell injury/death (KER 10). Calcium signaling mechanisms are known to exist that induce cell death (Zhivotovsky & Orrenius, 2011). Quantitatively, *in vivo* experiments have shown the relationship between increased intracellular calcium and cell death (Deshpande et al., 2014). In another study, Hartley et al. (1993) demonstrated the relationship between increased intracellular calcium and cell death after exposure to varying concentrations of Glu over time, and that MK-801 prevented calcium influx and reduced cell death.

Cell injury/death leads to N/A, Neurodegeneration (KER 11). As cell death is considered a marker of neurodegeneration, this relationship involves a broader scope involving cell death in the form of neurodegeneration in the context of an organ system rather than individual cell death. Terminal deoxynucleotidyl transferase dUTP nick end labeling (TUNEL) positive cells (as a marker of cellular injury through DNA damage) increased after three weeks of daily domoic acid (DA) injections, while neuronal nuclei protein (NeuN)-positive cells (a marker of living neurons) remained the same (Lu et al., 2012). Four weeks of DA injections, however, resulted in decreased NeuN-positive cells, showing an incidence concordance between cell injury or death and overall neurodegeneration.

1.4 Discussion

The literature review for the quantitative data available for KERs differs from searching for qualitative evidence for KEs. KER quantitative data specifically require an experimenter to have measured both related KEs while also being in the context of the AOP in question. Using Figure 1.2 as an example, quantitative data for KER 10 would involve a study measuring both increased intracellular calcium and some form of neuronal cell death while initiating these changes through perturbation of the MIE by inhibiting AChE. Ideally, it would be time-series or dose-response data amenable for qAOP model development. Such data are not common, however, as few experimenters are publishing data with AOP development or qAOP modeling in mind. As the

prevalence of AOPs increases, gaps in our understanding of biological processes will continue to be revealed, which will ideally lead to more experiments with AOP development in mind.

While AOPs by definition are intended to by chemically agnostic, studies show that some chemicals that produce the same AO do so via distinct mechanisms (Braitman & Sparenborg, 1989; Deshpande et al., 2010; Sparenborg et al., 1992). During the literature review process, conflicting evidence was found involving some AChE inhibitors and their resulting pathology upon exposure. Rats exposed to diisopropylfluorophosphate (DFP) manifested SE and did not respond to treatment with MK-801 (Deshpande et al., 2010). This contrasts with other similar experiments which showed a marked attenuation of seizure activity after MK-801 treatment in soman exposed rats (Braitman & Sparenborg, 1989; Sparenborg et al., 1992). There have also been conflicting results regarding increased Glu levels in some cholinergic seizure-inducing chemicals, and in one paper experimenters showed that sarin resulted in increasing Glu levels post-seizure onset while VX resulted in no changes (O'Donnell et al., 2011). DFP, soman, and VX are potent AChE inhibitors, but the specific processes through which each chemical progresses the pathology appear to be distinct enough to result in different methods of pathway progression and, in some cases, unresponsiveness to similar treatment. Despite the fact that the AOP does not account for these chemically specific differences, these separate mechanisms should be considered in the future.

AOPs are a simplification of biology's complexity and determining the appropriate KEs or KERs depends on how that biology can be best simplified while meeting the requirements of KEs. Doing so necessitates a specialist's knowledge in that field and therefore requires collaboration with experts. The prior iteration of AOP 281 originally had KER 7, calcium overload leading to SE (see Figure 1.1). This KER was originally proposed due to the fact that NMDA receptors are calcium permeable channels and NMDA receptor antagonism has been found to prevent SE in rat studies (Borris et al., 2000; Braitman & Sparenborg, 1989; Sparenborg et al., 1992). It was later discovered through further review and expert consultation that this KER lacked support in literature, and it was determined that KERs 6 and 9 in Figure 1.2 better defined the biology based

on literature evidence. As previously stated, AOPs are considered ‘living’ documents, and thus are expected to change with time as new evidence supporting or even rejecting AOPs emerges (OECD, 2018). As such, AOP development is an iterative process, and additional changes to AOP 281 may occur in the future. The construction of a qAOP model based on the quantitative data obtained from the literature review is the next step for AOP 281 development. The following chapter discusses in more detail the development of the quantitative model.

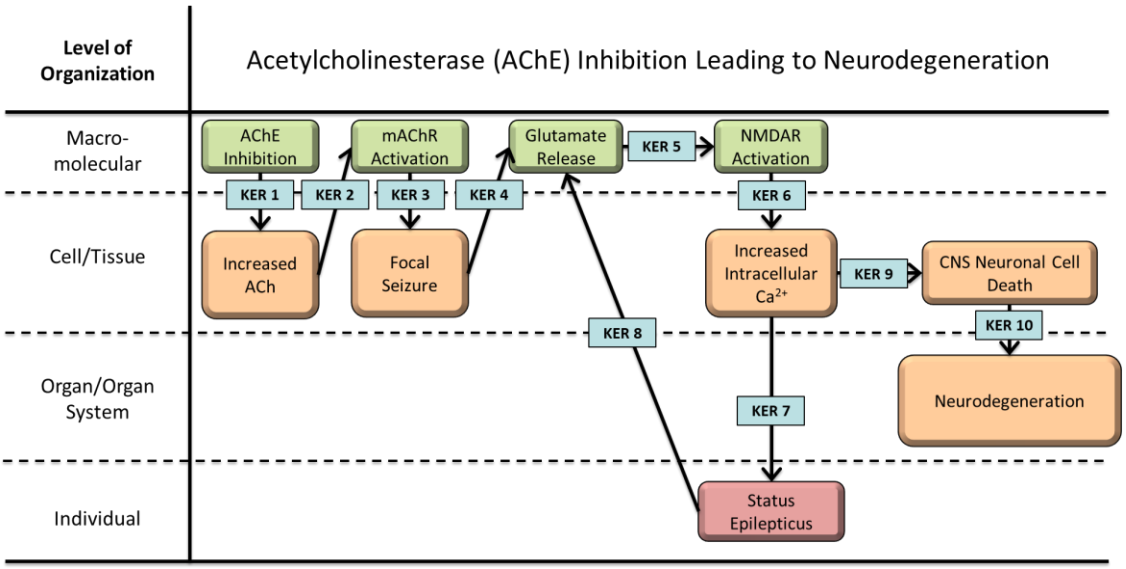

Figure 1.1. Prior Iteration of AOP 281 Conceptual Model. This shows AOP 281 (AChE Inhibition Leading to Neurodegeneration) without NMDAR activation leading to SE and SE leading to increased intracellular calcium (Conrow et al., 2021). AChE = Acetylcholinesterase. ACh = Acetylcholine. mAChR = Muscarinic Acetylcholine Receptor. NMDAR = N-methyl-D-aspartate Receptor.

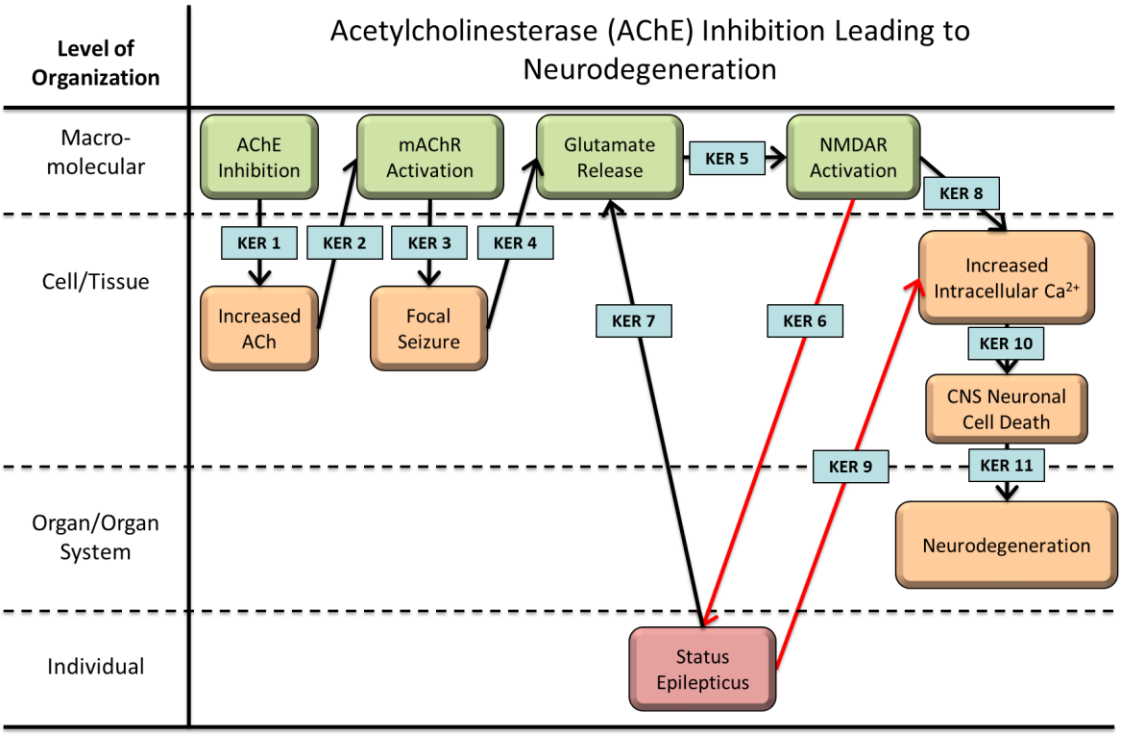

Figure 1.2. Conceptual Model Diagram of AOP 281: AChE Inhibition Leading to Neurodegeneration (Conrow et al., 2022). AChE = Acetylcholinesterase. ACh = Acetylcholine. mAChR = Muscarinic Acetylcholine Receptor. NMDAR = N-methyl-D-aspartate Receptor. The red lines indicate the newly added KERs.

CHAPTER 2

A QUANTITATIVE ADVERSE OUTCOME PATHWAY FOR ACETYLCHOLINSTERASE INHIBITION LEADING TO NEURODEGENERATION

2.1 Introduction

A qAOP is a mathematical model built upon the quantitative understanding of KERs that form the relationships between KEs. Given a perturbation in the MIE, a qAOP will be able to predict changes in the downstream KEs and AO. Depending on the level of quantitative understanding and available data, a qAOP can represent the relationships in a variety of ways, ranging from simple linear regression equations to biologically based models utilizing differential equations (Conolly et al., 2017). I chose to develop a biologically based model to represent the MIE (AChE inhibition) through KE 7 (increased intracellular calcium) because both positive (self-sustaining seizure through status epilepticus) and negative (interneuron inhibition) feedback loops influence the time-dependent changes in the pathway (Figure 1.2). In some cases, it is possible to model the feedback loop of a system as a response-response relationship. This is a mathematical relationship describing how a change in an upstream KE will impact the downstream KE, and includes models such as linear regression equations (OECD, 2018). This can be done if the system involved is assumed to reach and remain at steady-state (Sinitsyn et al., 2022; Zgheib et al., 2019). However, I am explicitly interested in perturbing the system and capturing its time-dependent dynamics, not steady-state.

A robust quantitative model for AChE inhibition can reduce the resources and time spent for chemical toxicity testing related to AChE inhibitors and is ultimately needed in order to reduce animal testing, provide accurate predictions of the AO for previously untested compounds, and extrapolate available *in vitro* data related to the pathway to *in vivo* settings. While time-series data of AChE activity or free remaining AChE may potentially be used as input for the model, there would be limitations to consider, as these time-series data would be specific to the chemical toxicant used, its route of exposure, and its concentration. This naturally would require the

availability of relevant chemical and toxicological data from experimental studies, or if available, existing PKPD models that may be integrated for model development. Thus, a qAOP can benefit from the integration of existing models such as these PKPD models as it would then enable the model to make predictions for unmeasured doses on the distribution and toxic effects of the chemical upon exposure. Doing so aligns well with the goals of a robust qAOP model as described above. Furthermore, due to the modular nature of AOPs, utilization of existing models and other models that represent an AOP's KER(s) can significantly improve the overall pace of qAOP development. The following section describes the qAOP model development process.

2.1.2 Modeling AChE Inhibition

I chose to model the impact of soman (CASRN 96-64-0) on the system as it is known to be a potent AChE inhibitor and has multiple PKPD models available (Chen & Seng, 2012; Langenberg et al., 1997; Maxwell et al., 1988; Sweeney et al., 2006). More specifically, I chose to adapt a PKPD model by Chen and Seng (2012) for use in the larger qAOP model because it predicts the level of free AChE in the brain after soman exposure through multiple routes including intramuscular (IM), intravenous (IV), and subcutaneous (SC), thus enabling the model to compare its predictions to data collected under different experimental conditions.

Figure 2.1 provides the schematic diagram used for the model and a brief overview of the model by Chen and Seng (2012) follows. Input parameters for the model are: (i) concentration of soman (ug/kg); (ii) rat weight (g); (iii) method(s) of injection, which include intramuscular (IM), subcutaneous (SQ), and intravenous (IV); and (iv) length of infusion for IV (s), which can be used to represent a slower introduction of soman into the system. As shown in the figure, soman is either injected directly into the venous blood compartment through IV administration, or injected into the subcutaneous compartment, which is then absorbed into the muscle compartment at a rate determined by the absorption rate constant. Soman flows through the system following the diagram before reaching the individual compartments representing the body systems and organs. Soman is removed from the system when it inhibits AChE or carboxylesterase (CaE) and is additionally removed through hydrolysis by diisopropyl-fluorophosphatase (DFPase). Soman

hydrolysis was considered to be significant in the arterial, venous, kidneys and liver compartment and is modeled through first-order elimination rate constants. Lastly, soman is not a single unique compound, but instead exists in an equal mixture of four stereoisomers, labeled C(-)P(-), C(-)P(+), C(+)P(-), and C(+)P(+). The individual isomers differ from one another in their ability to bind and inhibit AChE and in their rates of hydrolysis, with the P(-) isomer pair showing a significantly increased ability to inhibit AChE and *in vivo* toxic effects (Maxwell et al., 1988). Thus, the PKPD model simulates the individual stereoisomers rather than treating soman as a single molecule.

2.1.3 Modeling Neurons

Now with the PKPD model integrated, allowing for the prediction of free AChE in response to soman exposure, the remaining KEs can be modeled. As the KEs in the AOP are specific to the brain and involve neurophysiological processes such as neurotransmitters, receptor-ligand interactions, and intracellular calcium, I chose to work with a spiking neuron model that is able to incorporate these characteristics. Fundamentally, neurons respond to activation through receptors by firing or spiking, also known as an action potential. This process occurs with changes in the neuron's membrane potential, which is the electrical voltage across the cell's membrane. This voltage changes in response to various ion currents that are modulated by the activation of receptors. An action potential in turn releases neurotransmitters, thereby resulting in changes in the concentration of extracellular neurotransmitters. For the purposes of the AOP I chose to work with a neuron model that could simulate the enhanced excitability that has been demonstrated to occur through mAChR activation (Marrion, 1997). Specifically, mAChR activation leads to the inhibition of the M-current, a potassium ion current responsible for a process known as spike-frequency adaptation or spike adaptation (Marrion, 1997). This is an inhibitory process that reduces the frequency of action potentials in response to excitatory events. Consequently, inhibition of this process ultimately results in the neurons enhanced excitability and overall increased firing rate (Otto et al., 2006).

Existing models for spiking neurons range from the biologically detailed Hodgkin Huxley (HH) neuron model to simpler-integrate-and fire models with fewer parameters (Burkitt, 2006; Hodgkin

& Huxley, 1952). A neuron model that can account for changes in spike frequency adaptation via M-current inhibition by mAChRs was developed by Brette and Gerstner (2005). Originally based on an HH-model of a pyramidal neuron that incorporated M-current, the model simplifies the HH-model by instead accounting for M-current spike frequency adaptation with a generic adaptation variable that varies based on both the subthreshold membrane potential and after each action potential event (Brette & Gerstner, 2005). Brette and Gerstner (2005) found that the reduced formulation with fewer parameters is less computationally intensive than its HH counterpart and predicted on average 96% of the spikes of the HH-model (Brette & Gerstner, 2005). Thus, I chose to use this model in the qAOP as it would allow for the modeling of M-current inhibition through mAChR activation and the resulting enhanced excitability, ultimately leading to an overall increased rate of firing.

2.1.4 Modeling Synaptic Transmission

With increased Glu concentration as a KE in AOP 281, the qAOP model should also be able to predict extracellular glutamate. Destexhe et al. (1994a) report that Glu release and uptake is a rapid process, with Glu remaining in the synaptic cleft for a very brief amount of time, with estimates in the sub-millisecond scale (Clements et al., 1992). As such, I chose to model Glu release assuming it to be an instantaneous process occurring with each action potential event.

Binding of Glu to post-synaptic receptors ultimately result in the modulation of the post-synaptic neuron's membrane potential through changes in currents evoked by receptor activation. Receptor kinetic models by Destexhe et al. (1994b) were adapted for use in the qAOP model as they included receptor-ligand interactions and the consequent depolarization or hyperpolarization of a neuron's membrane potential. Specifically, models for excitatory AMPA-Kainate (AK) receptors for depolarization and action potential generation and inhibitory Gamma-aminobutyric acid type A ($GABA_A$) receptors for membrane hyperpolarization were adapted. M1 mAChR binding kinetics were adapted from Mergenthal et al. (2020) as their model was calibrated to match the behavior of rat CA1 pyramidal neurons in response to M1 mAChR activation through binding of ACh. M1 mAChR kinetics were simplified in the model to include the forward and

reverse binding rate kinetics. An NMDA receptor kinetic model was adapted from Hu et al. (2018) as part of their intracellular calcium model, which will be described in further detail below. The integration of these kinetic models thus allows for the modeling of synaptic transmission and prediction of both neurotransmitter concentration and receptor activation.

2.1.5 Modeling Calcium Dynamics

Intracellular calcium homeostasis is a tightly regulated process and involves many mechanisms of calcium influx and efflux (Barhoumi et al., 2010; Case et al., 2007). Hu et al. (2018) recently developed a model of post-synaptic calcium dynamics at the dendritic spine of a CA1 pyramidal neuron, where the dendritic spine refers to the protrusion of synaptic membrane that includes the post-synaptic membrane and its associated membrane-bound receptors and intracellular mechanisms. I chose to adapt the model by Hu et al. (2018) as the model is able to show changes in intracellular calcium due to both NMDA receptor and VDCC activation, which reflects the multiple methods of calcium entry as shown in the AOP through KER 8 and KER 9. The model, however, could not be reproduced in whole as not all parameter values were provided in the original publication, and I was unable to obtain these values from the author. To address this issue of missing parameters, I chose to simplify the calcium model and instead adjust the reduced parameters to align with the intracellular calcium data used in the original model's calibration. Figure 2.2 provides a schematic diagram of the simplified model. Calcium influx occurs via two channels, NMDA receptors and VDCCs. NMDA receptors follow an eight-state kinetic receptor model by Hu et al. (2018) that represents the free, bound, desensitized and open states of an NMDA receptor (see Hu et al. (2018) Supplementary Figure 1). NMDA receptors generate calcium influx dependent on the total number of bound and open receptors and the calcium potential difference between intracellular and extracellular calcium. Through Glu binding, NMDA receptors open and increase the rate of calcium influx. VDCCs are dependent on both the post-synaptic membrane and calcium potential difference, opening more frequently with further membrane depolarization. The calcium currents due to NMDA and VDCC activation were modified to include a conversion factor and tuned to fit experimental data and will be discussed in

more detail in the methods section. Additionally, calcium buffering and efflux has been simplified due to the missing parameters and is instead modeled solely as calcium efflux following first-order elimination. Through these above mechanisms the model simulates changes in intracellular calcium in response to changes in membrane potential (VDCCs) and receptor activation (NMDARs).

2.1.6 Description of the qAOP Model

Figure 2.3A shows a conceptual model for the qAOP. The model was designed to capture the salient biological features of the AOP and its KERs. The model is specifically of a group of neurons located in the CA1 hippocampal region in the rat brain, shown in Figure 2.3B. The CA1 region was selected as it is one of the most extensively studied regions and there is evidence showing that neuronal cell death occurs in this region following exposure to AChE inhibitors and subsequent SE (Deshpande et al., 2010; Deshpande et al., 2014; Deshpande et al., 2008). Neuron 0 in Figure 2.3B is modeled as the cholinergic input onto Neuron 1. Biologically, its soma is situated in the medial septum and projects to the CA1 region and is therefore not represented in the figure. This cholinergic neuron was selected as they are known for their cholinergic input into this region (McKinney et al., 1983). Neuron 1 is modeled as a CA1 excitatory pyramidal neuron. These are glutamatergic neurons that are known for receiving cholinergic input through their post-synaptic mAChRs, to which they respond by entering a hyperexcitable state (Dasari & Gulledge, 2011). M1 mAChRs were chosen as they have been shown to be the major excitatory muscarinic receptor involved in the neuron entering this excitable state (Cruickshank et al., 1994; Hamilton et al., 1997). Neuron 2 is an inhibitory interneuron that is modeled as an Oriens-Lacunosum-Moleculare (OLM) interneuron, a GABAergic interneuron known for its involvement in feedback inhibition in the hippocampal region (McKinney et al., 1983). Neuron 2 receives glutamatergic input from Neuron 1 through the binding of post-synaptic AMPA and Kainate receptors. For the purposes of this model, AMPA and Kainate receptors fulfill the same role, thus the receptors are combined as AMPA-Kainate (AK) receptors based on the work by Destexhe et al. (1994b). Neuron 3 is also modeled as an excitatory CA1 pyramidal neuron. This neuron

receives glutamatergic input through NMDA receptors resulting in calcium influx, with additional calcium influx occurring through activation of VDCCs.

The majority of Figure 2.3A aligns with the AOP shown in Figure 1.2, however, additions in the form of negative feedback loops were included to account for the time delays seen to occur in the pathology. These modifications are highlighted as orange-dashed lines, and account for the negative-feedback inhibition and delay in seizure activity occurring prior to the onset of focal seizure activity that is seen in the biology, also referred to as the breakdown of the inhibitory surround (Kandel et al., 2013a). The qualitative AOP does not include these specific mechanisms as KE 3 (onset of focal seizures) would encompass these biological processes that occur as part of a focal seizure. Neuron 2 fires and releases GABA in response to synaptic activation from Neuron 1, thereby modeling this inhibitory feedback mechanism. The AOP contains two KEs regarding seizure activity: Onset of focal seizure and status epilepticus. While these events can be measured through methods such as EEG activity, firing rate is instead used in the model as a substitute for these events as it has been shown that individual neurons increase in firing rate upon recruitment to the seizure (McKinney et al., 1983; Merricks et al., 2021). Furthermore, *in vivo* seizure activity is a complex biological process, making it challenging to study the cellular impacts of SE, however studies that initiate *in vitro* status epilepticus, defined as continuous high-frequency activity, using neuronal cultures have been able to show the relationship between seizure duration and changes in both intracellular calcium and neuronal death (Deshpande et al., 2007; Pal et al., 1999).

2.2 Methods

2.2.1 Data Collection

The literature review conducted for the development of the AOP was utilized for the development of the qAOP. While the AOP is meant to be a general framework that is applicable to any species adversely affected by this pathway, the qAOP requires species-specific data for model development because species differ in various aspects of the AOP (Pereira et al., 2014).

Therefore, *Rattus norvegicus* was chosen as the species for model development due to the amount of data available compared to other species. A further literature review, using the same databases and search engines as with the prior review, was conducted to identify relevant models, model equations, and parameter values required for qAOP model development that were not applicable as quantitative data for any specific KER in the AOP, such as individual neuron models or AK and GABA receptor binding kinetics. Initially, an exploratory literature review was conducted with 'neuron models' to gain a better understanding of the available variety of models before further refining the searches to 'adaptive integrate-and-fire neuron models' that were specific to the qAOP model's needs. Additionally, a literature review of receptor binding kinetics in rats involved using paired terms such as 'AMPA receptors' or 'AMPAR binding kinetics' combined with rats or related variations. After gathering the necessary data, relevant models, and model equations from both the AOP and qAOP literature reviews, the information was integrated to form the qAOP model, which is detailed below.

2.2.2 AChE Inhibition Model Formulation

The PKPD soman model by Chen and Seng (2012) was integrated into the qAOP model to simulate AChE inhibition, as previously stated. More specifically, I adapted the PKPD model in a reduced format, focusing on the initial reaction between AChE and soman while excluding the formation of the downstream products, which include the inhibited AChE-soman complex and aged AChE-soman complex as these are considered irreversible steps and thus there is no feedback between these products and the initial reaction. Furthermore, there are no available data to validate the dynamics of these products. The remaining components of the model by Chen and Seng (2012) are used as provided by the authors, with no changes to the formulation of the equations. Note that some variable names have been modified to maintain consistency between the model equations and model code. Specifically, CpPp, CpPm, CmPp, and CmPm represent the concentration of the individual soman stereoisomers whereas the original authors used C(+)P(+), C(+)P(-), C(-)P(+), and C(-)P(-), respectively. As the purpose of the model is to determine AChE activity in the brain, and with the above information in mind, the remaining focus

of soman and its effects on the system presented will be on the brain and its relevant compartment. AChE is inhibited through soman, and free AChE in the brain is modeled as:

$$\frac{dC_{\mathrm{AChE_{Br}}}}{dt} = K_{\mathrm{SYN}} - K_{\mathrm{DEG}} * C_{\mathrm{AChE_{Br}}} - C_{\mathrm{AChE_{Br}}} * (\mathrm{CpPp_{Br}} * k_{\mathrm{CpPp_{AChE}}} + \mathrm{CpPm_{Br}} * k_{\mathrm{CpPm_{AChE}}} + \mathrm{CmPp_{Br}} * k_{\mathrm{CmPp_{AChE}}} + \mathrm{CmPm_{Br}} * k_{\mathrm{CmPm_{AChE}}}) , \quad (1)$$

where $\mathrm{CpPp_{Br}}$, $\mathrm{CpPm_{Br}}$, $\mathrm{CmPp_{Br}}$, and $\mathrm{CmPm_{Br}}$ (μM) represent the concentration of the individual soman stereoisomers C(+)P(+), C(+)P(-), C(-)P(+), and C(-)P(-), respectively in the brain. K_{SYN} (=3.056e-12 μM ms^{-1}) and K_{DEG} (=1.64e-10 ms^{-1}) represent the 0th order synthesis rate constant and 1st order degradation rate constant for AChE, respectively. $C_{\mathrm{AChE_{Br}}}$ (μM) represents the concentration of free AChE in the brain.

Next, it was assumed that soman inhibits AChE evenly throughout the brain, which allows AChE in the hippocampus to be based on the remaining free AChE concentration as modeled by the PKPD model Chen and Seng (2012) , and is defined as:

$$C_{\mathrm{AChE}} = \mathrm{C_{AChE_T}} * \left(\frac{C_{\mathrm{AChE_{Br}}}}{C_{\mathrm{AChE_{Br\_T}}}}\right) , \quad (2)$$

Where $C_{\mathrm{AChE_{Br\_T}}}$ (=3.78e-2 μM) is the initial concentration of AChE in the brain, $\mathrm{C_{AChE_T}}$ (=3e-4 mM) is the initial synaptic concentration of AChE in the hippocampus, and C_{AChE} (mM) represents the current concentration of AChE in the hippocampus at any time *t*. Doing so creates a separation of AChE concentrations; one for the concentration of whole brain free AChE ($C_{\mathrm{AChE_{Br}}}$), and another for the synaptic AChE concentration in the hippocampus (C_{AChE}). This is done as AChE is not evenly distributed throughout the whole-brain but rather is localized to specific regions (Das et al., 2001). Therefore, using the measured value of whole brain free AChE from tissue homogenate would not be appropriate when modeling synaptic concentrations of AChE. Two assumptions are required here, however: Changes in free hippocampal AChE due to inhibition by soman directly correlates to changes in whole-brain free AChE. This assumption is supported by multiple authors

demonstrating that overall changes in AChE in the brain follows a similar trend regardless of the region measured (Fosbraey et al., 1990; Kassa & Bajgar, 1998). Changes in synaptic AChE concentration in the hippocampus will not affect total whole brain tissue homogenate AChE concentration, as the prior represents an overall smaller concentration of AChE compared to whole brain AChE.

2.2.3 Accumulation of ACh and M1 mAChR Activation

As the concentration of free AChE decreases due to inhibition by soman, the neurotransmitter ACh begins to increase in the synaptic cleft as rate of hydrolysis decreases. ACh is modeled as shown in Eq (3).

$$\frac{\mathrm{d}C_{\mathrm{ACh}}}{\mathrm{d}t} = k_{\mathrm{rM1}} * C_{\mathrm{M1_B}} - k_{\mathrm{fM1}} * C_{\mathrm{ACh}} * C_{\mathrm{M1}} - k_{\mathrm{AChE}} * C_{\mathrm{ACh}} * C_{\mathrm{AChE}} \text{ , and} \quad (3)$$

At spike time (V_0 > -40.4 mV):

$C_{\mathrm{ACH}} = C_{\mathrm{ACh}} + \mathrm{ACh}_{\mathrm{Release}}$,

where k_{AChE} (=150 mM^{-1} ms^{-1}) is the bimolecular rate constant for hydrolysis of ACh by AChE. ACh is added to the system through $\mathrm{ACh}_{\mathrm{Release}}$ (=2 mM) at regular intervals based on the firing rate of Neuron 0. Based on the basal firing rate values for neurons, this was determined to be 0.4 Hz (Simon et al., 2006). Spike time is defined as the time at which an action potential occurs, where the membrane potential of Neuron 0 reaches -40.4 mV. Additionally, Neuron 0 was assumed to maintain a constant basal firing rate in the model due to a lack of experimental data on changes in individual firing rates during seizure activity of medial septum cholinergic neurons.

In the synaptic cleft, ACh binds to free M1 mAChRs, and is modeled as

$$C_{\mathrm{M1}} = C_{\mathrm{M1}_T} - C_{\mathrm{M1}_B} \text{ , and} \quad (4)$$

$$\frac{\mathrm{dC_{M1B}}}{\mathrm{d}t} = k_{\mathrm{fM1}} * \mathrm{C_{ACh}} * \mathrm{C_{M1}} - k_{\mathrm{rM1}} * C_{\mathrm{M1}_B} \text{ ,} \quad (5)$$

Where C_{M1} and C_{M1_B} (mM) represent free and bound M1 mAChRs, and C_{M1_T} (=2.25e-2 mM) is the total concentration of M1 mAChRs. k_{fM1} (=2.78 $\mathrm{mM^{-1}\ ms^{-1}}$) and k_{rM1} (=2.15e-3 $\mathrm{ms^{-1}}$) are the forward and reverse binding rate constants for ACh binding to M1 mAChR.

2.2.4 Neuron 1 Membrane Potential Model Formulation

Neuron 1 follows an integrate-and-fire model containing an adaptation equation *w* and exponential spiking mechanism (Brette & Gerstner, 2005). The membrane potential for Neuron 1 evolves over time following the equation

$$\mathrm{CM}_1 \frac{dV_1}{dt} = I_{\mathrm{leak1}} + g_L * \Delta_{T1} * \exp\left(\frac{V_1 - V_{T1}}{\Delta_{T1}}\right) - I_{\mathrm{GABA}} + I_{\mathrm{injectN1}} - w\ , \tag{6}$$

where, V_1 (mV) is the membrane potential for Neuron 1, CM_1 (=281 pF) is the membrane capacitance, g_L(=30 nS) is the leak conductance, V_{T1} (=-50.4 mV) is the threshold potential, and Δ_{T1} (=2 mV) is the slope factor. I_{leak1}, I_{GABA}, and w (pA) are variable currents defined by their own functions. I_{injectN1} (= 580 pA) is a constant applied current used to establish a basal firing rate of approximately 1 Hz based on *in vivo* recordings of CA1 pyramidal neurons at rest (Wiener et al., 1989).

The leak current, responsible for establishing resting membrane potential in the neurons, is defined as

$$I_{\mathrm{leak1}} = g_L\ *\ (E_L - V_1)\ , \tag{7}$$

where E_L (=-70.6 mV) is the resting potential. In addition to M1 mAChRs, Neuron 1 also contains inhibitory $\mathrm{GABA_A}$ receptors, responsible for modulating the firing rate through binding by the neurotransmitter GABA, released by Neuron 2. $\mathrm{GABA_A}$ receptor binding is modeled as the fraction of bound receptors following first-order kinetics, with the equations and estimated rate constants obtained from Destexhe et al. (1994b).

$$\frac{dr_{GABA_A}}{dt} = k_{f\mathrm{GABA_A}} * C_{\mathrm{GABA}} * \left(1 - r_{\mathrm{GABA_A}}\right) - k_{r\mathrm{GABA_A}} * r_{\mathrm{GABA_A}}\ , \tag{8}$$

where r_{GABA_A} (unitless) is the fraction of bound $GABA_A$ receptors, while $k_{f\mathrm{GABA_A}}$(=5 mM^{-1} ms^{-1}) and $k_{r\mathrm{GABA_A}}$(=1.8e-1 ms^{-1}) are the forward and reverse rate constants, respectively, and where C_{GABA}(mM) is the concentration of the GABA neurotransmitter in the synaptic cleft. With the fraction of bound $GABA_A$ receptors known, the post-synaptic current I_{GABA_A} can be modeled as

$$I_{\mathrm{GABA}_A} = \mathrm{g}_{\mathrm{GABA}_A} * r_{\mathrm{GABA}_A} * \left(V_1 - E_{\mathrm{GABA}_A}\right), \tag{9}$$

where $\mathrm{g}_{\mathrm{GABA}_A}$(7.25e-1 nS) is the maximal conductance and E_{GABA_A}(=-80 mV) is the reversal potential of $GABA_A$ receptors. The reversal potential is the membrane potential at which point the current changes direction, and biologically relates to a specific ion's net flow across a cell membrane, in this case chloride (Cl^-) ions.

In Eq. 6, the variable current w is the adaptation current and represents the adaptive inhibitory effect of the M-current on Neuron 1. The adaptation current is modified from Brette and Gerstner (2005) to include the relationship between mAChR activation and change in membrane potential, and is modeled as

$$\tau_w * \frac{dw}{dt} = \left(1 - \frac{C_{\mathrm{M1_B}}}{C_{M1_T}}\right) * a * (V_1 - E_{\mathrm{L}}) - w, \tag{10}$$

At spike time (V_1 > -40.4 mV):

$$V_1 = V_{1r}$$

$$w = w + b * (1 - \frac{C_{\mathrm{M1_B}}}{C_{M1_T}})$$

Where τ_w(=144 ms) is the time constant and a (nS) is the subthreshold adaptation. Additionally, w is increased by $b * (1 - \frac{C_{\mathrm{M1_B}}}{C_{M1_T}})$ after each firing event, which represents the spike-triggered adaptation of the integrate-and-fire model (Brette & Gerstner, 2005), where V_{1r} (=-70.6 mV) is the resting membrane potential, and b (=80.5 pA) is a constant modified by $(1 - \frac{C_{\mathrm{M1_B}}}{C_{M1_T}})$. Thus, $b * (1 -$

$\frac{C_{\mathrm{M1B}}}{C_{M1_T}}$) is added to the *w* variable after each spiking event, representing spike-triggered adaptation as mentioned above. The equation *w* from Brette and Gerstner (2005) was modified by including a proportionality term ($1 - \frac{C_{\mathrm{M1B}}}{C_{M1_T}}$), which scales *w* based on bound M1 receptors. When mAChR activation occurs, it causes the neuron to enter a hyperexcitable state (Dasari & Gulledge, 2011). This is done biologically by ultimately reducing the inhibitory effect of the M-current, as mentioned above. This is modeled between bound mAChRs and the *w* variable using the proportionality term ($1 - \frac{C_{\mathrm{M1B}}}{C_{M1_T}}$) in Eq. 10.

2.2.5 Formulation of Glutamate Mass Balance and Release

Upon each firing event, Neuron 1 releases a set amount of Glu similar to a vesicle of Glu released during an action potential (see #1 in Figure 2.4). Glu release occurs simultaneously in both synapses between Neuron 1 and Neurons 2 and 3. The Glu mass balance in the synapse between Neuron 1 and 2 is modeled as

$$\frac{dC_{\mathrm{GluN2}}}{dt} = \mathrm{k_{rAK2}} * \left(r_{\mathrm{AK2}} * \mathrm{C}_{AK2_T}\right) - k_{\mathrm{fAK2}} * C_{\mathrm{Glu_{N_2}}} * \left(C_{AK2_T} * (1 - r_{\mathrm{AK2}})\right) - k_{\mathrm{elimGlu}} * C_{\mathrm{Glu_{N_2}}} \quad (11)$$

At spike time (V_1 > -40.4 mV):

$$C_{\mathrm{Glu_{N_2}}} = C_{\mathrm{Glu_{N2}}} + \mathrm{Glu_{Release}},$$

where $C_{\mathrm{Glu_{N_2}}}$ (mM) is the concentration of Glu in the synapse between Neurons 1 and 2. The constants k_{rAK2} (=1.9e-1 ms^{-1}) and k_{fAK2} (=1.1 mM^{-1} ms^{-1}) are the reverse and forward binding rate constants for Glu binding to AK receptors (see #2 in Figure 2.4). $\mathrm{C}_{AK_{2T}}$ (=1.1e-1 mM) is the total (free plus bound) AK receptor concentration in the synapse, while r_{AK2} (unitless) represents the fraction of bound AK receptors at time *t*. Next, k_{elimGlu} (=5 ms^{-1}) is a first-order rate constant representing the clearance rate of Glu from the synapse and encompasses known biological mechanisms of clearance such as re-uptake by neighboring glial cells, diffusion out of the synapse, and degradation. Glu entering the synapse occurs when Neuron 1 fires an action

potential upon reaching threshold (V1 > -40.4 mV). $\mathrm{Glu}_{\mathrm{Release}}$ (13.0 mM) is the instantaneous release of Glu into the synapse. $\mathrm{Glu}_{\mathrm{Release}}$ was calculated based on an assumption of 10,000 molecules released (Destexhe et al., 1994b) in a synaptic cleft volume of 1.26e^{-3} μm^3 (Hübel et al., 2017). This results in an increased concentration of Glu by 13.17mM after each firing event.

Glu release and the mass balance between Neuron 1 and 3 is modeled similarly. Upon firing, Neuron 1 releases Glu instantaneously and follows the same release amount and volume assumptions outlined above. In this synapse, Glu binds to post-synaptic NMDA receptors on Neuron 3. The NMDA receptor is modeled as an 8-state kinetic model as following the model by Hu et al. (2018). Glu mass balance for the synapse between Neuron 1 and 3 is modeled as:

$$\frac{d\mathrm{C}_{\mathrm{Glu}_{N3}}}{dt} = k_{\mathrm{off}_{\mathrm{NMDA}}} * C_{\mathrm{RA}} + 2 * k_{\mathrm{off}_{\mathrm{NMDA}}} * C_{\mathrm{RA2}} - 2 * k_{\mathrm{on}_{\mathrm{NMDA}}} * C_{\mathrm{Glu}_{\mathrm{N3}}} * C_R - k_{\mathrm{on}_{\mathrm{NMDA}}} * C_{\mathrm{Glu}_{\mathrm{N3}}} * C_{\mathrm{RA}} - k_{\mathrm{elimGlu}} * C_{\mathrm{Glu}_{\mathrm{N3}}} \quad (12)$$

where $k_{\mathrm{off}_{\mathrm{NMDA}}}$ (=1.01 ms^{-1}) and $k_{\mathrm{on}_{\mathrm{NMDA}}}$ (=31.6 mM^{-1} ms^{-1}) are the reverse and forward binding rate constants, respectively, for Glu binding to either the *R* or RA states or unbinding from the RA or RA2 states of the NMDA receptors (see Hu et al. (2018) Supplementary Figure 1). These are denoted as C_R, C_{RA}, and C_{RA2} (mM), representing the concentration of R, RA, and RA2 states.

2.2.6 Neuron 2 Feedback Inhibition and Release of GABA

Neuron 2 AK receptor activation by Glu causes Neuron 2 to fire in a similar integrate-and-fire model as seen in Neuron 1, modeled as

$$\frac{dr_{\mathrm{AK2}}}{dt} = k_{\mathrm{fAK2}} * C_{\mathrm{Glu}_{\mathrm{N2}}} * (1 - r_{\mathrm{AK2}}) - k_{\mathrm{rAK2}} * r_{\mathrm{AK2}} \text{ , and} \quad (13)$$

$$\mathrm{CM}_2 * \frac{dV_2}{dt} = I_{\mathrm{leak2}} - I_{\mathrm{AK2}} + g_L * \Delta_{\mathrm{T2}} * \exp\left(\frac{V_2 - V_{\mathrm{T2}}}{\Delta_{\mathrm{T2}}}\right) + I_{\mathrm{injectN2}} \text{ ,} \quad (14)$$

where V_2 (mV) is the membrane potential for Neuron 2, I_{leak2} (pA) is the leak current for Neuron 2 and follows the same formulation as Eq. 7. I_{injectN2} (=553 pA), Δ_{T2} (=2 mV), V_{T2} (=-50.4 mV) are the injected current, slope factor, and threshold potential for Neuron 2, following the same

functions as with Neuron 1 in Eq. 6. I_{AK2} (pA) is the excitatory current due to AK receptor activation. I_{AK2} is determined by Eq. (15),

$$I_{\mathrm{AK2}} = g_{\mathrm{AK2}} * r_{\mathrm{AK2}}(V_2 - E_{\mathrm{AK2}}) \,, \tag{15}$$

where g_{AK2} (6.75e-1 nS) is the maximal conductance of current due to AK2 receptor activation, and E_{AK} (0 mV) is the reversal potential for AK receptor currents. Upon firing, Neuron 2 releases GABA and the mass balance for the GABA concentration (C_{GABA}) follow kinetics similar to Glu from Neuron 1 and Eq. 11.

$$\frac{dC_{\mathrm{GABA}}}{dt} = k_{\mathrm{rGABAA}} * C_{\mathrm{GABA}_{A_b}} - k_{\mathrm{fGABAA}} * C_{\mathrm{GABA}} * C_{\mathrm{GABA}_A} - k_{\mathrm{elimGABA}} * C_{\mathrm{GABA}} \,, \tag{16}$$

At spike time (V_2 > -40.4 mV):

$C_{\mathrm{GABA}} = C_{\mathrm{GABA}} + \mathrm{GABA}_{\mathrm{Release}}$,

where k_{rGABAA} (=1.8e-1 ms^{-1}) and k_{fGABAA} (=5 mM^{-1} ms^{-1}) is the reverse and forward binding rate constant for GABA binding to $GABA_A$ receptors, k_{elimGABA} (=5 ms^{-1}) is the firsr-order clearance rate of GABA from the synaptic cleft, and $C_{\mathrm{GABA}_{A_b}}$, C_{GABA}, and C_{GABA_A} (mM) are the concentrations of bound $GABA_A$ receptors, free GABA neurotransmitter, and free $GABA_A$ receptors, respectively. When the membrane potential of V_2 (mV) reaches spike threshold, the constant value, $\mathrm{GABA}_{\mathrm{Release}}$ (mM), for lack of data on how much GABA is released, is assumed to be an equal concentration to $\mathrm{Glu}_{\mathrm{Release}}$, and is instantaneously added to the pool of GABA in the synaptic cleft. Once in the synaptic cleft, GABA is able to bind to $GABA_A$ receptors following Eq. 8, resulting in the feedback inhibition due to the change in current from Eq. 9.

2.2.7 Neuron 3 and Calcium Dynamics

As previously mentioned, the calcium model adapted from Hu et al. (2018) has been simplified as the model could not be reproduced in its original state due to missing parameter values. All changes made to the model equations are described in detail below. However, other

aspects of the model that were incorporated, but remained unchanged from the original model, will be described briefly and referenced appropriately.

On firing, Neuron 1 releases Glu into the synaptic cleft between Neuron 1 and 3. Glu stays in the synaptic cleft following Eq. 12 and binds to the NMDA receptors located on Neuron 3. The membrane potential of Neuron 3, V_3 (mV) follows similarly to Neuron 1 and 2 with the addition of an NMDA current, and is modeled as:

$$\mathrm{CM}_3 * \frac{dV_3}{dt} = I_{\mathrm{leak3}} + g_L * \Delta_{T3} * \exp\left(\frac{V_3 - V_{T3}}{\Delta_{T3}}\right) - I_{\mathrm{NMDA}} + I_{\mathrm{injectN3}} \ , \tag{17}$$

where I_{NMDA} (pA) is the excitatory current due to NMDA receptor activation. I_{leak3} (pA) is the leak current for Neuron 3 and again follows the same formulation as Eq. 7. I_{injectN3} (=0 pA), Δ_{T3} (=2 mV), V_{T3} (=-50.4 mV) are the injected current, slope factor, and threshold potential for Neuron 3, and follow the same functions as in Eq. 6. I_{injectN3} is currently set to 0 because the model does not currently simulate the positive glutamatergic feedback loop in the AOP between NMDA receptor activation, SE, and Glu. Setting I_{injectN3} to 0 removes the basal firing rate of the neuron and allows the model to specifically predict influx of intracellular calcium due NMDA receptor activation. This corresponds to KER 8 in the AOP. The I_{NMDA} current has been modified from the Hu et al. (2018), and is now modeled as

$$I_{\mathrm{NMDA}} = \mathrm{CF}_{\mathrm{NMDA}} * g_{\mathrm{total}_{\mathrm{NMDA}}} * V_{\mathrm{Ca}} \ , \tag{18}$$

where $\mathrm{CF}_{\mathrm{NMDA}}$ (=6, unitless) is a conversion factor applied to the NMDA current as calcium influx due to NMDA receptor activation could not be reproduced as done by the original model due to the previously stated missing parameters. This parameter was fit based on experimental measurements of changes in intracellular calcium from Sabatini et al. (2002) in response to NMDA receptor activation. V_{Ca} (mV) is the voltage for calcium ions, and follows the original equations proposed by Hu et al. (2018). However, changes to some variable names have been made and therefore will be explained in detail. V_{Ca} is modeled as

$$V_{\mathrm{Ca}} = -\frac{R_{\mathrm{con}} * T_{\mathrm{con}}}{2 * F_{\mathrm{con}}} * \log\left(\frac{C_{\mathrm{Ca}_{\mathrm{EC}}}}{C_{\mathrm{Ca}_{\mathrm{spine}}}}\right), \quad (19)$$

where R_{con} (=8.31 J mol^{-1} K^{-1}) is the molecular gas constant, T_{con} (=299.5 K) is the temperature in kelvin, and F_{con} (=9.65e4 C mol^{-1}) is Faraday's constant. $C_{\mathrm{Ca}_{\mathrm{EC}}}$ (=2 mM) is the extracellular calcium concentration which is assumed to remain constant. $C_{\mathrm{Ca}_{\mathrm{spine}}}$ (mM) is the intracellular calcium concentration in the spine compartment. The variable $g_{\mathrm{total}_{\mathrm{NMDA}}}$ (pS) (Eq. 18) is the maximal possible conductance for NMDA receptors and is modeled as

$$g_{\mathrm{total}_{\mathrm{NMDA}}} = g_{\mathrm{NMDA}} * n_{\mathrm{NMDA}}, \quad (20)$$

where g_{NMDA} (pS) is the NMDA conductance for NMDA receptors and n_{NMDA} (=10, unitless) is the total number of NMDA receptors within the post-synaptic density (PSD) compartment (see Figure 2.2). The variable g_{NMDA} (pS) is dependent on magnesium ion binding, which in turn is dependent on the neuron's membrane potential. Magnesium ions bind to and act as a blockade to NMDA receptors, preventing the flow of current. The variable g_{NMDA} is modeled as

$$g_{\mathrm{NMDA}} = g_{\mathrm{max}} * \frac{C_O}{C_{NMDA_T}}, \quad (21)$$

where g_{max} (pS) is the current conductance for NMDA receptors that is dependent on membrane potential and magnesium binding, while C_O (mM) is the concentration of NMDA receptors in the open state and is part of the 8-state kinetic model, and C_{NMDA_T} (=1.66e-4 mM) is the total concentration of NMDA receptors, regardless of state, in the PSD compartment. Both g_{max} and the NMDA 8-state kinetic model by Hu et al. (2018) have been incorporated into the qAOP model as presented in their original work and are therefore not included as part of the set of equations described here.

Next, calcium influx is dependent on both NMDA receptor and VDCC activation. As mentioned previously, the calcium dynamics of the model by Hu et al. (2018) were simplified to include only calcium influx through tuned NMDA and VDCCs and efflux through a first-order

elimination rate constant. Following Figure 2.2, calcium is divided into two compartments. Calcium influx into the spine compartment is modeled as

$$\frac{dC_{\mathrm{Ca_{spine}}}}{dt} = D_{\mathrm{Ca}} * \frac{A_{\mathrm{surfArea}}}{d_{\mathrm{dist}} * V_{\mathrm{spine}}} * \left(\mathrm{C}_{\mathrm{Ca_{PSD}}} - C_{\mathrm{Ca_{spine}}}\right) + \frac{I_{\mathrm{VDCC}}}{2 * F_{\mathrm{Con}} * V_{\mathrm{spine}}} - k_{\mathrm{elim}_{Ca}} * C_{\mathrm{Ca_{spine}}} , \quad (22)$$

where $C_{\mathrm{Ca_{spine}}}$ and $\mathrm{C}_{\mathrm{Ca_{PSD}}}$ (mM) are the concentrations of intracellular calcium in the dendritic spine and the PSD, respectively. Calcium diffusion occurs between these two compartments, where D_{Ca} (=2.25e-1 μm^2 ms^{-1}) is the calcium diffusion coefficient, A_{surfArea} (=5e-2 μm^2) is the surface area between the PSD and spine compartment, d_{dist} (=7e-1 μm) is the distance between the midpoints of two compartments, and V_{spine} (=1e-1 μm^3) is the volume of the spine compartment. Calcium elimination was simplified from the Hu et al. (2018) model and is modeled here through the first-order elimination rate constant $k_{\mathrm{elim}_{Ca}}$ (=7e-1 ms^{-1}), which was manually tuned to fit experimental data from Sabatini et al. (2002). The variable I_{VDCC} (pA) is the calcium influx current due to VDCC activation, and is modeled as

$$I_{\mathrm{VDCC}} = \mathrm{CF}_{\mathrm{VDCC}} * g_{\mathrm{con}_{\mathrm{VDCC}}} * m^2 * h * \mathrm{dvf}_{\mathrm{VDCC}} , \quad (23)$$

Where $g_{\mathrm{con}_{\mathrm{VDCC}}}$ (=7.5 pS) is the single-channel conductance for VDCC channels, and $\mathrm{CF}_{\mathrm{VDCC}}$ (=2.3e4, unitless) is the conversion factor applied to the VDCC current. In the same manner as with the NMDA current, $\mathrm{CF}_{\mathrm{VDCC}}$ was manually tuned to fit experimental measurements of changes in intracellular calcium from Sabatini et al. (2002), specifically due to VDCC activation. As I_{VDCC} is a voltage-dependent current, Hu et al. (2018) chose to model this following a Hodgkin and Huxley formalism (Hodgkin & Huxley, 1952), where m (unitless) and h (unitless) are voltage-dependent gating variables which range from 0 to 1; the product of the two ultimately determine the total channel conductance. The VDCC current is further modified by $\mathrm{dvf}_{\mathrm{VDCC}}$ (V) which is the equilibrium potential that is dependent on membrane potential and the internal and external calcium concentration. The equations that define the m , h , and $\mathrm{dvf}_{\mathrm{VDCC}}$ variables and parameters were taken from Hu et al. (2018) without modification. Lastly, $C_{\mathrm{Ca_{PSD}}}$ in Eq. 22

represents the intracellular calcium concentration in the PSD. The PSD compartment models calcium influx through NMDA receptors and is modeled similarly to the spine compartment in Eq. 22. Intracellular calcium in the PSD compartment is modeled as

$$\frac{dC_{\mathrm{Ca_{PSD}}}}{dt} = \frac{-I_{\mathrm{NMDA}}}{2*F_{\mathrm{Con}}*V_{\mathrm{PSD}}} - \mathrm{D_{Ca}} * \frac{A_{\mathrm{surfArea}}}{d_{\mathrm{dist}}*V_{\mathrm{PSD}}} * \left(C_{\mathrm{Ca_{PSD}}} - C_{\mathrm{Ca_{spine}}}\right) , \quad (23)$$

where the influx of calcium through NMDA receptors is included here as I_{NMDA}, and V_{PSD} (3.2e-3 μm^3) is the volume of the PSD compartment. Overall, the simplified Hu et al. (2018) calcium model included the tuning of the unknown parameters $\mathrm{CF_{NMDA}}$, $\mathrm{CF_{VDCC}}$, and $k_{\mathrm{elim}_{Ca}}$, as described above. These parameters were manually tuned using the same experimental data from Sabatini et al. (2002) that were used in the validation of the original model by Hu et al. (2018), thus allowing the simplified model predictions to be compared to original model output provided in Hu et al. (2018).

2.2.8 Neurotransmitter Dialysate Model

The incorporation of the above neurotransmitter and receptor kinetic models enable the model to simulate changes in neurotransmitter concentration in the synapse at a small timescale on the order of milliseconds. However, since experimental measurements of neurotransmitter concentration are often performed using microdialysis, which has limited temporal resolution, I have incorporated a 'microdialysis' compartment into the model. Specifically, this compartment mimics the process of microdialysis and accounts for relevant parameters including the flow rate of the dialysate and collection interval that are provided in the experimental methods. The microdialysis compartment equations for both Glu and ACh include:

$$\frac{dX_{dialysate}}{dt} = \mathrm{flowRate} * C_X , \text{ and} \quad (24)$$

$$\frac{\mathrm{d}V_{\mathrm{liq}}}{dt} = \mathrm{flowRate} , \quad (25)$$

where $X_{dialysate}$ (mmol) is the amount of neurotransmitter in the collection tube, either ACh or Glu, $\mathrm{flowRate}$ (=3.33e-11 L ms^{-1}) is the rate at which the dialysate is pumped through, C_X (mM) is the neurotransmitter concentration in the synaptic cleft, and V_{liq} (L) is the total volume of liquid accumulated in the collection tube. At the end of each collection interval, the concentration of the dialysate in the collection tube is calculated and the above variables reset to 0. The inclusion of this compartment now allows the model to make predictions of larger scale changes in neurotransmitter concentration observed under microdialysis experiments (Lallement et al., 1992; Tonduli et al., 1999).

2.2.9 Model Implementation and Simulation Environment

Model simulations were performed using the open-source integrated development environment (IDE) Spyder (Raybaut, 2009) in Python, version 3.8.8. To solve the system of ordinary differential equations (ODEs) that define the model, I used the solve_ivp function using the Runge-Kutta 45 (RK45) integration method, available in the SciPy library (Virtanen et al., 2020). The model was run using the following computer specifications: Windows 10 Operating System (OS), Intel Core i7-8700K, 6 cores, 3.70 GHz, and 16 GB DDR4 3200 MHz RAM.

2.2.10 Model Evaluation

To evaluate the model, the qAOP model predictions were compared against the original model output provided by Chen and Seng (2012) and compared to the observed data reported in Maxwell et al. (1988) and Chen and Seng (2012) for changes in free AChE and arterial soman stereoisomer after soman exposure, respectively. A mean squared error (MSE) was calculated to quantify the differences between model predictions and data, following:

$$\mathrm{MSE} = \frac{1}{\mathrm{n}}\sum_{i=1}^{n}\left(Y_i - \widehat{Y}_i\right)^2, \tag{26}$$

where Y_i is the observed value from the data, $\widehat{Y}_i$ is the predicted value from the model, and n is the total number of data points. Next, a model evaluation was performed by comparing model

predictions of free AChE, ACh and Glu dialysate, and calcium to available experimental data, totaling seven independent sets of data. Specifically, free AChE was compared to data provided by Maxwell et al. (1988), Tonduli et al. (1999), Reddy et al. (2021), and Kassa and Bajgar (1998), while hippocampal ACh and Glu dialysate was compared to data by Lallement et al. (1992). As mentioned previously, studies have demonstrated that there are comparable levels of AChE inhibition across different brain regions, and therefore the data provided by Tonduli et al. (1999), which measured AChE inhibition in frontal cortex tissue, and Reddy et al. (2021), which measured AChE inhibition in cerebral cortex tissue, were considered suitable for model evaluation.

Additionally, model predictions of ACh dialysate were compared to hippocampal ACh dialysate data, as it has been demonstrated that there is a region-dependent difference in both basal ACh content and its accumulation upon soman exposure (Fosbraey et al., 1990).This is further supported by the significant differences reported in ACh dialysate given the same experimental procedure and similar dose of soman between Tonduli et al. (1999) and Lallement et al. (1992). Therefore, as the qAOP model is a model of the hippocampal region, ACh dialysate was compared to data reported by Lallement et al. (1992) because they measured changes in hippocampal dialysate. Specifically, Lallement et al. (1992) first measured basal neurotransmitter concentrations, followed by SC injection of soman, noting seizure activity to begin on average 13 minutes post-injection. Their first dialysate sample was then collected 10 minutes post-seizure onset. This resulted in Lallement et al. (1992) effectively measuring their first dialysate point 23 minutes post-soman injection. In order to align the qAOP model to the data, I chose to introduce soman at the 17-minute mark, ensuring that I can both collect a basal neurotransmitter concentration followed by 10-minute collection intervals as done so by the authors. This allows the fourth collection point to be 23 minutes post-soman injection, thus corresponding to the first 10-minute post-seizure dialysate sample in the paper. This approach allows the model predictions to be compared to the observed data at the appropriate time points.

As previously mentioned, firing rate is used as a substitute in the model for seizure activity as it has been shown that individual neurons increase in firing rate upon recruitment to the seizure (McKinney et al., 1983; Merricks et al., 2021). Tonduli et al. (1999) demonstrated that the fraction of animals developing seizures in response to soman exposure is dose dependent. Tonduli et al. (1999) were able to demonstrate that seizures were triggered in 0% and 100% of rats given a SC injection of 79 and 152 µg/kg soman, respectively. Additionally, they reported that seizure onset occurred between 10 to 49 minutes post-soman administration. Thus, I evaluated the qAOP model's ability to predict the onset of seizure activity by comparing the model's firing rates within that window of time under the two dosing scenarios: 79 and 152 µg/kg soman, SC. Specifically, firing rate in the model is defined as the number of action potentials per second (Hz), and was calculated by counting the number of action potentials per one second interval. While the model predicts the firing rate of each neuron individually, it is the firing rate of Neuron 1 that will be evaluated in order to determine the model's ability to predict onset of seizure activity. This is because Neuron 1 represents the excitatory CA1 pyramidal neurons with mAChRs, which become hyperexcited upon receptor activation (Dasari & Gulledge, 2011). If the model reaches a firing rate given a 152 µg/kg soman, SC dose that was not observed under the 79 µg/kg dose, it will indicate that this distinct firing rate reached is indicative of seizure activity. Conversely, if firing rates overlap and no distinct value is reached, the model cannot reliably predict the onset of seizure activity. Under these conditions, the model can be evaluated in order to determine if it can predict the onset of seizure activity based on firing rate.

Next, although there are a lack of experimental data measuring intracellular calcium after soman exposure, other organophosphates, notably diisopropyl fluorophosphate (DFP) and paraoxon, have been demonstrated to cause similar increases in intracellular calcium after the onset of SE, with respective increases to approximately 6.5e4 mM and 7.5e4 mM 1-hour post-exposure. The qAOP model currently simulates changes in increased intracellular calcium in response to NMDA receptor activation, corresponding to KER 8. The qAOP model currently does not reproduce SE. However, the experimental data measures intracellular calcium after inducing

SE, which implicitly involves more than NMDA receptor activation. Additionally, the integrated calcium model is specifically of intracellular calcium of dendritic spine, while the above data are of measurements of whole-cell intracellular calcium. To make the comparison between the experimental data and model predictions requires the assumption that changes in intracellular calcium in the dendritic spine of the neuron reflects its changes in whole-cell intracellular calcium. Despite these differences, this comparison is still valuable to make in order to evaluate the model's current calcium predictions. Therefore, model predictions of intracellular calcium are evaluated with the reported range of intracellular calcium values under the conditions of SC injection of soman (152 ug/kg), which as previously mentioned have been shown to elicit seizures in 100% of animals tested (Tonduli et al., 1999).

Lastly, although there are no experimental data available to evaluate the model at the smaller timescale for model predictions regarding membrane potential, pulses of neurotransmitter concentration in the synapse, and receptor activation dynamics, examining the model's predictions here is still valuable as it is these underlying dynamics and their change over time that ultimately shape the larger-scale changes in the model. Thus, I chose to examine the qAOP model's predictions within the first and final seconds of a 1-hour simulation following a 100 µg/kg SC injection of soman, given a 250g rat weight.

2.2.11 Sensitivity Analysis

As the model includes several unknown parameters, a sensitivity analysis was conducted to examine the impact changes in these parameters would have on model output. The selected values for these unknown parameters were chosen based on assumptions made about the underlying biology due to a lack of data specific to those parameters. While there are additional parameters whose values were otherwise fit or optimized as part of some of the adapted models, I specifically considered parameters to be unknown if they were: (i) created independently of prior models; (ii) modified to better fit experimental data; (iii) had no biologically relevant range of values due to lack of data. A sensitivity analysis was performed by adjusting each parameter by ±40%, with the methods following a local sensitivity analysis (Hamby, 1994).

I chose a ±40% variation in parameters over the more commonly used ±20% as some of the unknown parameters had a potential range broad enough that the ±20% variation did not adequately cover the range of parameter values tested, as shown in Table 2.1. The model conditions chosen for the analysis were a 60-minute simulation given a SC injection of soman (100 ug/kg) assuming a 250g mass for the rat and a 10-minute dialysate collection interval with a flow rate of 3.33e-11 L / ms. Model predictions of free AChE (% of basal) and ACh concentration (mM) and Glu concentration (mM) in dialysate at 30-minutes and 60-minutes post-soman injection were recorded in order to calculate relative sensitivity. Additionally, a 1-second average calcium (mM) concentration was recorded at 60-minutes post-soman injection. While using an average calcium value here obscures the dynamics of calcium seen in the model, it is still informative to use to assess the sensitivities of these unknown parameters. Multiple timepoints were selected for the sensitivity analysis in order to highlight the variations seen in the model's response to changes in these unknown parameters based on the timepoint selected. I specifically chose to combine the relative sensitivity from both the increased and decreased parameter to assess the overall variation seen in the model. The relative sensitivity (RS) helps identify which parameters had the most impact on model output and therefore help inform future work for parameter estimation and validation. The RS was then calculated for each endpoint at 30-minutes and 60-minutes post-soman injection following the equation:

$$RS = \frac{\left(\frac{\left|Y_{+40\%} - Y_{-40\%}\right|}{Y_0}\right)}{0.8}, \tag{27}$$

where $Y_{-40\%}$ and $Y_{+40\%}$ are the values of endpoint Y when unknown parameter X is decreased or increased by 40%, respectively, Y_0 is the original value of Y when no parameters are changed, and 0.8 is the normalized range of variation in X, as a ±40% change divided by the original parameter value X corresponds to 0.8. The relative sensitivity of each unknown parameter can then be determined based on the resulting value, where an RS of >1 or <1 would imply there is greater than 40% or less than 40% variation in the model output given a ±40% change in

parameter X, respectively. The parameters of each endpoint that were determined to be sensitive were then visualized as figures to show the dynamic changes in endpoints throughout the run of the model. 20 timepoints were selected over an evenly spaced interval for AChE as this allows for a better visualization of the changes in free brain AChE post-soman injection. The timepoints for the ACh and Glu dialysates are based on the collection interval used and thus are presented at 10 minutes intervals. Lastly, the fluctuations seen in intracellular calcium occur at a smaller timescale relative to the changes in the other endpoints. Thus, I chose to use 101 timepoints over an evenly spaced interval in the last second of the model run to better visualize this behavior.

2.3 Results

The qAOP model currently simulates the MIE to KE 7, with the exception of SE (KE 6). The model can simulate IM, SC, and IV injection of soman. Appendix C provides the Python code for the model implementation, evaluation, and sensitivity analysis. Appendix D provides the list of dependent variables and parameters that define the model. Under the given computer specifications, 1 minute of simulation time takes approximately 10 minutes of real-time computation. Below are the results of model evaluation using available experimental datasets. These results include predictions of free AChE, ACh and Glu concentrations measured through microdialysis, and intracellular calcium concentrations. Also included are model predictions of the changes occurring at the smaller timescales, such as changes in membrane potential, pulses of neurotransmitter concentration in the synapse, and receptor activation dynamics given a SC injection of soman (100 µg/kg) within the first and final one to 10 seconds of a 1-hour simulation. Finally, the results of the sensitivity analysis of the unknown parameters are included to determine their significance and impact on the model's behavior.

2.3.1 Comparison of AChE Model Predictions with Experimental Data

The model is able to output predictions of tissue AChE concentrations upon exposure to soman. Figure 2.5 shows a comparison between the model predictions versus experimental data from Maxwell et al. (1988), and compares free AChE as a percentage of total initial AChE (% free

AChE) after inhibition by an intramuscular injection of 90 ug/kg of soman. Each subfigure has an associated mean squared error (MSE) to quantify the differences between model prediction and data by comparing model output at the timepoints measured in Maxwell et al. (1988). Overall, the comparison between model output and experimental data demonstrates that while most of the tissue compartment predictions align well and show agreement with the measured data, there are compartments, specifically the liver and kidney (Figures 2.5C and F), where the model does not predict the experimental data well. Among the compartments, diaphragm AChE follows most closely to the data with a MSE of 70, followed by heart, brain, and lung AChE with MSEs of 180, 190 and 190, respectively, while the kidney and liver AChE compartments align least closely with respective MSEs of 1100 and 2000. Overall, this suggests that the model may benefit from further refinement. However, as brain AChE is used as the input for the remaining elements of the model, it's relatively good fit helps ensure the reliability of the model's downstream predictions.

It is important to note that the Chen and Seng (2012) model was calibrated in part with the data from Maxwell et al. (1988), however the current model output deviates from the output provided in the original paper. Using the same MSE methods as described above, the model output, experimental data, and output provided by Chen and Seng (2012) were compared. Figures 2.6A and 2.6B shows the same model output as with Figure 2.5 overlayed with the output provided by Chen and Seng (2012) for the brain and diaphragm compartment. The model predictions extracted from Figure 5 in Chen and Seng (2012) yield MSEs of 240 and 69 with respect to the brain and diaphragm compartments (compared to MSEs of 190 and 70 for qAOP model output as above). Model predictions for free brain AChE fits to the experimental data better than the original model predictions. The comparison of the diaphragm compartment is nearly identical. Figures 2.6C and 2.6D show model predictions for two of the four soman stereoisomers, C(+)P(-) and C(-)P(+) following an IV injection of soman. This was compared to the model output provided by Chen and Seng (2012) with experimental measurements extracted from Figure 4 in the paper. The differences between the model predictions are more noticeable here than with the brain and diaphragm compartments. In both 2.6C and 2.6D, the model output from the Chen and

Seng (2012) model fits to the experimental data better than the qAOP model. The qAOP model underpredicts the C(+)P(-) soman isomer and overpredicts the C(-)P(+) soman isomer in the arterial compartment. Overall, as the model's equations were taken from Chen and Seng (2012) unmodified, these differences warrant further investigation into their underlying cause.

2.3.2 Comparison of Calcium Model Predictions with Experimental Data

The model by Hu et al. (2018) was simplified as stated previously, and the qAOP model predictions of intracellular calcium in response to NMDA receptor and VDCC activation were compared to the output provided by Hu et al. (2018) and experimental data by Sabatini et al. (2002), and is shown in Figures 2.7A and 2.7B, respectively. The qAOP model is able to predict the peak calcium concentrations reached under the experimental conditions, but it was unable to simulate the slower decay of calcium concentration observed in the experimental data. Instead, the qAOP model underpredicted calcium concentration as it decreased from its peak value. In contrast, the model output by Hu et al. (2018) aligned more closely to the experimental data. This indicates that the qAOP model's simplified representation of calcium dynamics is not sufficient to capture the underlying mechanisms responsible for the observed rate of decay at this timescale. However, despite the limitations in predicting the decay rate at this scale, the primary focus of the qAOP model lies in the long-term calcium behavior, which is more relevant to the AOP. Thus, the model was also compared to experimental data on a longer timescale and is presented below.

2.3.3 Model Evaluation with AChE Experimental Data

The qAOP model's predictions of brain AChE inhibition after soman exposure were evaluated against four independent data sets (Kassa & Bajgar, 1998; Maxwell et al., 1988; Reddy et al., 2021; Tonduli et al., 1999) and included both SC and IM administration scenarios. Figure 2.8 shows the results of qAOP model predictions after SC administration compared against data provided by Tonduli et al. (1999). Figure 2.8A shows that given an SC injection of soman (103 µg/kg), the model predicts near maximal inhibition of AChE, with <1% of free AChE at 100 minutes post-soman exposure (equal to approximately 140 minutes on Figure 2.8A), while the

observed data show free AChE reaches approximately 30% at that same point in time. Furthermore, the model predicts a faster rate of inhibition, reaching maximal AChE inhibition approximately 10 minutes post-soman injection (equal to approximately 50 minutes on Figure 2.8A), while the observed data show 50% free AChE at that same timepoint. Figure 2.8B shows a similar overall trend given a SC dose 90 µg/kg, with the model predicting both a greater maximal and rate of inhibition of AChE compared to the experimental data. Reddy et al. (2021) demonstrated a similar reduction in free AChE after a SC injection of 154 µg/kg of soman. Figure 2.9 shows that under these conditions the qAOP model behaves similarly and overpredicts the rate of inhibition and underpredicts the free AChE 60 minutes post-soman injection. In summary, the model consistently overestimates the rate and extent of AChE inhibition following doses of soman ranging from 90-154 µg soman/kg under SC administration compared to what has been observed based on the experimental data.

The fourth evaluation data set used IM administration scenarios. Figure 2.10 compares qAOP model predictions of free AChE with data provided from Maxwell et al. (1988) and Kassa and Bajgar (1998) 30-minutes after IM injection of 107 µg soman/kg and 1-hour after IM injection of 48 µg soman/kg, respectively. Predictions of free AChE in each tissue compartment in Figure 2.10A follow a similar trend as seen in Figure 2.5, where the qAOP model underpredicts the free AChE in liver and lung tissue and aligns well with the observed data in diaphragm tissue. In both Figures 2.10A and B, the qAOP model overpredicts the percent of free brain AChE after soman injection. Although time-series data were not available for these specific doses, evaluating the model at these individual timepoints of 30-minutes and 1-hour post-soman injection shows that the model overpredicts free brain AChE under IM administration scenarios.

2.3.4 Evaluation with Experimental Data – ACh and Glutamate

Model predictions were evaluated against hippocampal neurotransmitter concentration data provided by Lallement et al. (1992), and are presented in Figure 2.11, where predictions in both ACh and Glu dialysate concentrations are compared to the observed data. In both cases, the model overpredicts ACh and Glu dialysate concentrations. Furthermore, the model greatly

overpredicts the observed pattern of change in both ACh and Glu dialysate, where both neurotransmitters appear to temporarily decrease approximately 40 minutes post-soman injection (at 50 minutes in Figure 2.10A and 60 minutes in Figure 2.10B) before increasing again. Although these notable differences exist, one key similarity can be observed. Lallement et al. (1992) demonstrated that hippocampal ACh reaches a higher maximum percent increase (approximately 500% of basal levels) compared to Glu (approximately 330% of basal levels). The qAOP model exhibits a similar behavior as ACh dialysate is seen to increase to a greater peak percentage than Glu. Overall, the significant differences between the model predictions and experimental data seen here highlight the need for parameter optimization and model refinement.

2.3.5 Evaluation with Experimental Data – Determining Seizure Activity

Figures 2.12A and B show the model's predicted changes in firing rate in response to 79 µg/kg and 152 µg/kg of soman, injected SC. Neurons 1, 2 and 3 are shown for reference, however as stated previously it is the firing rate of Neuron 1 that will determine if the model can predict onset of seizure activity. In both dosing scenarios, the model predicts a peak firing rate of 17.5 Hz in Neuron 1 soon after soman exposure. Figure 2.12C overlays both dosing scenarios to better compare the firing rate predictions of Neuron 1. The small and large doses result in a peak firing rate reached after approximately 4 and 7 minutes, respectively. The qAOP model does not predict a different firing rate in response to the larger dose of soman; in both cases the firing rate remains the same through the 10–49-minute window. Thus, as a change in firing rate is not obtained in this time window, the changes in model-predicted firing rates cannot be used to predict the onset of seizure activity.

2.3.6 Evaluation with Experimental Data – Calcium

Figure 2.13 shows the results of the model predictions of intracellular calcium 1-hour after a SC injection of 152 ug soman/kg compared to the observed intracellular calcium of neurons in animals after receiving either DFP or paraoxon. Figure 2.13A shows the qAOP model predictions within the last second of a 1-hour model simulation after soman injection. The model is shown to

consistently fluctuate between 1.2e-4 and 2.5e-4 mM occurring in response to the dynamics of NMDA receptors and first-order elimination kinetics. To reiterate, Neuron 3 is not firing as there is no injected current, thus VDCCs which respond to changes in membrane potential are not active, therefore the influx of calcium is due to NMDA receptor activation. The average response over that 1 second period is shown in comparison to experimental data on Figure 2.13B. The model underpredicts intracellular calcium compared to the experimental observations, predicting an average of 1.8e-4 mM 1-hour post exposure, demonstrating that the model requires further refinement and additional considerations to predict the long-term calcium concentrations more accurately, as NMDA receptor activation alone is not enough to accurately predict intracellular calcium.

2.3.7 Smaller Timescale Components of the Model

Figures 2.14A and B show the first and last seconds, respectively, of a 1-hour simulation following a 100 µg/kg SC injection of soman and assuming a 250g rat weight. Figure 2.14A shows up to the first 10 seconds of the model simulation, and soman is not yet significantly inhibiting brain AChE, with brain AChE remaining 100% free during this window (figure not shown). Therefore, the changes observed here in these neuronal components are representative of the unperturbed conditions of the model. Synaptic ACh, Glu, and GABA concentration all follow a pulsatile behavior, quickly reaching a peak concentration based on their associated instantaneous release of neurotransmitter concentrations. AK and $GABA_A$ receptors respond with similar dynamics, quickly reaching their respective peak bound values before decreasing to 0. Conversely, mAChRs demonstrate a slower dissociation process which can be seen in the figure by the more gradual decline in bound mAChRs, reflecting the receptor's slower rate of unbinding, 0.00215 ms^{-1}, versus 0.19 ms^{-1} and 0.18 ms^{-1} for the dissociation rate of glutamate from AK and GABA receptors, respectively. Interestingly, Neuron 1 responds to mAChR activation at this basal rate by firing in pairs of action potentials. This is similar to a bursting firing rate behavior where neurons fire in rapid succession, however the timing between actions potentials required to define this behavior as bursting is less than 15 ms between spikes, whereas Neuron 1 fires with an

approximate delay of 80 ms between the pairs (Harris et al., 2001). This paired firing and subsequent release of glutamate in quick succession also exposes the desensitization kinetics that are part of the NMDA receptor model, whereby the second binding event of each pair results in a smaller peak percent bound due to receptor desensitization. This is due to the 8-state kinetic model containing desensitized states (see Supplementary Figure 1 in Hu et al. (2018)).

Next, Figure 2.14B shows the final seconds of the model simulation. Synaptic ACh dynamics are now much slower. There remains a constant presence of ACh in the synapse. For better context, the model predicts AChE decreasing to approximately 0.6% free AChE at this time (figure not shown). This increased ACh is clearly at a saturating concentration as mAChRs are persistently 100% bound during this window. In response to this, Neuron 1 is now firing at a much higher frequency and is no longer firing following that paired-spiking behavior. As mAChRs are 100% bound, this firing rate would be the maximum firing rate possible for the neuron to achieve, which is approximately 17.5 Hz. This saturation of mAChRs explains well why the model's overall changes in firing rate remained identical with regard to its ability to determine seizure activity from Figure 2.12. As the same 17.5 Hz firing rate is reached under both conditions, it indicates that mAChRs reach saturation under both of the low and high dose conditions. Under this persistent receptor activation, NMDA receptors are fluctuate around a lower (approximately 9% bound) range due to further desensitization. In both scenarios, GABA and $GABA_A$ receptors remain unchanged, exhibiting a constant pattern of release, binding, and elimination. This suggests that the portion of the model responsible for GABA may be insufficient as it has a limited range of behavior. Overall, examining the model behavior at this smaller timescale exposes interesting behaviors and helps to explain model predictions at longer timescales.

2.3.8 Sensitivity Analysis

A sensitivity analysis was performed with the endpoints free AChE, ACh and Glu dialysate concentration, and intracellular calcium concentration. Parameters were considered unknown if they were created independently of prior adapted models, were modified to better fit experimental data, or had no biologically relevant range of values. A total of 14 parameters fit these criteria.

Table 2.1 provides the list of unknown parameters along with their definition and assumptions made that informed their values. The results of the sensitivity analysis are presented in Tables 2.2 and 2.3, evaluated at 30-minutes and 60-minutes post-soman injection, respectively.

F_SC was determined to be the parameter that had the greatest sensitivity overall. This parameter had the strongest influence on free brain AChE concentration and showed a diminishing effect on the Glu and ACh dialysate concentration endpoints, with no effect on the intracellular calcium concentration endpoint. Additionally, F_SC had the greatest sensitivity regarding the ACh dialysate endpoint, followed by C_AChE_T at both 30 and 60-minutes. Regarding the Glu dialysate endpoint, k_elimGlu had the greatest sensitivity, followed next by F_SC. Lastly, k_elimCa showed the greatest sensitivity with regard to the average intracellular calcium endpoint with an RS of approximately 1.0. Although parameters cf_NMDA and cf_VDCC show comparably less sensitivity, with corresponding values of approximately 0.7 and 0.28, respectively in Table 2.3, they still show some degree of sensitivity in comparison to the remaining parameters with RS values of 0. Overall, the parameter F_SC had the greatest sensitivity given an adjustment of ±40% to its value.

The results of the sensitivity analysis for these parameters have been presented graphically in Figures 2.15 to 2.18 for each relevant endpoint, showing the changes in model behavior given a ±40% change in one of the unknown parameters. Figure 2.15 shows the impact F_SC has on model output for the free brain AChE endpoint, demonstrating that a 40% decrease in F_SC resulted in a greater change in model output than a 40% increase. Conversely in Figure 2.16, a 40% decrease in F_SC results in a smaller change in model behavior with regards to ACh dialysate, while most of the change in model output regarding Glu dialysate (Figure 2.17) is due to a 40% increase in F_SC. This asymmetrical response to changes in F_SC indicates a saturability in some of the model's mechanisms. The differences seen between the ±40% adjustments in free AChE best highlight this as the original model results in near maximal AChE inhibition at approximately 15 minutes (Figure 2.15). Thus, an increase in F_SC shows a limited effect on this endpoint, while a decrease in the parameter has more room for change and is

demonstrated by the asymmetry observed in the figure. As another example of this saturability, a 40% increase in F_SC results in a large change in ACh dialysate compared to the -40% output (Figure 2.16A), while there is only a correspondingly small change in Glu dialysate from this (Figure 2.17A). This can best be understood by referring back to Figure 2.14B, where it was demonstrated that mAChRs are saturated under these conditions. Therefore, as mAChRs are already fully saturated under the original model's conditions, further increases in ACh would have no additional influence on mAChR activation. Without overall changes in the behavior of mAChRs, the overall firing rate and ultimately release of Glu remains the same, which is what is observed in Figure 2.17A. Continuing on, changes in the parameter C_AChE_T results in expected model behavior, showing that an increase or decrease in the parameter results in an overall decrease or increase in ACh dialysate (Figure 2.16). Additionally, while C_AChE_T was determined to be insensitive at the 30 and 60-minute timepoints, minor changes in Glu dialysate at 10 and 20 minutes post-soman injection can be seen in response to a ±40% adjustment in C_AChE_T. This demonstrates that the model's response to adjustments in these parameters are dependent on the timepoint selected.

Lastly, Figure 2.18 presents the dynamic behavior in intracellular calcium seen in the last second of the 60-minute model run. The results here demonstrate that adjustments in parameters cf_NMDA, cf_VDCC, and k_elimCa result in two specific changes to calcium dynamics (Figure 2.18): I) Changes in the overall average calcium measured over the course of the one second interval, and II) changes in the amplitude of these intracellular calcium fluctuations, most noticeable with changes to k_elimCa, where an increase in k_elimCa results in an overall reduced average intracellular calcium value and an overall smaller amplitude. Overall, plotting the changes in model output in response to a ±40% change in a parameter demonstrates how changes in these parameters affect the model over time, and specifically highlights that the model's response varies based on the timepoint observed. These plots were additionally able to reveal the differences in model output within a parameter, as the changes in model output when the parameter was either increased or decreased was asymmetrical.

2.4 Discussion

2.4.1 Model Reproducibility and Simplification

The successful implementation of existing models into larger frameworks helps to streamline model development. In the context of the qAOP model, multiple models have been adapted for this purpose as the models predicted the endpoints used in the AOP. However, model reproducibility has been a concern. Adapting the PKPD model by Chen and Seng (2012) and comparing qAOP model output versus the output provided by Chen and Seng (2012) clearly showed there were differences between the two. A thorough review of the model implementation did not result in any model discrepancies, suggesting other potential causes. Variations in hardware or software used could potentially lead to differences between model output. Originally, Chen and Seng (2012) developed the model in MATLAB 7.8 (Matlab, 2012), while the qAOP model runs in Python. Additional differences could be due to the integration method used. The qAOP model uses RK45, while Chen and Seng (2012) did not specify their integration method. To better understand the cause of these differences, the model could be reconstructed in MATLAB to allow for a closer comparison between the outputs.

Next, the calcium model adapted from Hu et al. (2018) was ultimately simplified as the model also could not be reproduced due to missing parameter values. Simplifying a model to use fewer overall parameters can be beneficial if the model is still able to capture the salient features of the system, however oversimplification can result in a loss of accuracy, as was demonstrated when the qAOP model was compared against the experimental measurements from Sabatini et al. (2002) and the original model output reported by Hu et al. (2018). Despite these differences, the simplified model, while unable to simulate the finer scale changes in dendritic intracellular calcium, may still be used to predict changes in total intracellular calcium levels. Doing so would first require calibration of the parameters to experimental data of larger scale changes in intracellular calcium. However, data that measure changes in intracellular calcium concentration in response to soman exposure are not available, which limits development options.

Lastly, several challenges were encountered in the development of the qAOP model. While performing the sensitivity analysis, it was noted that changes in certain parameters resulted in changes in upstream endpoints despite the lack of any feedback mechanisms that could have led to that change. This behavior was attributed to the adaptive step size in the solve_ivp function. The model contains conditional triggers that result in instantaneous release of neurotransmitters. This abrupt change from what would otherwise have been a smooth derivative likely led to errors in the solution and ultimately this unintended behavior. This was solved by introducing a maximum timestep of 0.1 milliseconds. While this drastically slowed the computation time of the model, it successfully eliminated the unintended behavior. Next, decreasing the k_elimGABA parameter resulted in the model terminating early and was thus not shown as part of the sensitivity analysis. This was initially believed to be due to GABA potentially exceeding tolerable limits as a reduction in this parameter would be expected to result in increased GABA. If the parameter is reduced enough GABA could theoretically increase to infinite values as there is no mechanism to prevent this in the model. Upon further investigation, however, GABA appeared to remain controlled, and still behaved in an expected pulsatile manner. Thus, the cause of this early termination under this specific condition remains unknown.

2.4.2 Model Refinement and Sensitivity Analysis

Initially, two parameters were identified that could have an impact on the model's predictive capability for the free brain AChE endpoint: K_a_SC and F_SC. These parameters were considered unknown as they were originally tuned for guinea pigs, thereby requiring the assumption that the values for SC absorption and bioavailability of soman in guinea pigs follows the same pattern in rats. Interestingly, both K_a_SC (3.17e-5 ms^{-1}) and F_SC (0.68) were calculated to be larger than K_a_IM (4.33e-6 ms^{-1}) and F_IM (0.3). This is unusual as biologically an IM injection would be expected to have faster absorption and bioavailability than an SC injection due to the muscle tissue being more vascularized. Ultimately though, the sensitivity analysis revealed that K_a_SC was an insensitive parameter for the endpoints measured at 30 and 60 minutes and did not result in any calculable changes given a ±40% adjustment in its

value. As this was a local sensitivity analysis, however, it did not evaluate the potential interaction between the two parameters, therefore a simultaneous change in both K_a_SC and F_SC may still result in a more pronounced effect in the free brain AChE endpoint compared to only a change in F_SC. Overall, the univariate or local sensitivity analysis performed has inherent limitations in describing the model's overall behavior as it only evaluates the effect of each parameter on an individual basis, and thus does not account for the interactions between parameters. Furthermore, while the approach to combine the relative sensitivities of both the increased and decreased parameter changes into a single value helped to explain the parameters overall impact on the model, it ultimately concealed the differences between the two adjustments within a parameter. This was revealed when plotting the model's responses to each of the sensitive parameters. Therefore, calculating the relative sensitivities separately based the direction of adjustment would be more beneficial as it may reveal parameters that are more or less sensitive depending on the direction of change. Despite these limitations, multiple unknown parameters were determined to be sensitive based on the analysis, ultimately warranting formal parameter optimization. Additionally, parameter sensitivity differed based on the timepoint selected, as was demonstrated by the differences in F_SC sensitivity in the 30-minute versus 60-minute timepoints. To analyze this change over time, the sensitivities could be calculated at multiple timepoints and visualized by plotting those values over time. Sweeney et al. (2006) performed a similar analysis of their PKPD soman model and examined the changes in RS of model parameters over time. As part of future work, it could be valuable to perform a similar analysis as it would provide deeper insight into the time-dependent nature of relative sensitivities or highlight key points in time where certain parameters may show an enhanced sensitivity.

In addition to optimization, further refinement of the model may be beneficial. For example, the microdialysis compartment developed to mimic dialysate concentration could be improved by incorporating additional parameters such as dialysis efficiency, as it has been shown that the ratio between actual extracellular concentration and dialysate concentration is on average approximately 40% (Chefer et al., 2009). Additionally, the qAOP model currently assumes

constant basal release of ACh regardless of the conditions in the model. This is another example of oversimplification, as the model was unable to predict the dynamic changes seen in both hippocampal ACh and Glu as reported by Lallement et al. (1992). The dynamic changes were attributed to the existence of M2 mAChRs that act as autoreceptors in a negative feedback loop to ultimately inhibit and reduce the release of ACh (Quirion et al., 1994). Thus, incorporating such a behavior in the model would allow it to better predict these dynamic changes and have the model align more closely to the observed data. Ideally, the addition of the above-mentioned aspects of model refinement and formal parameter optimization would allow the model to better fit the experimental data and ultimately become a predictor of seizure activity based on firing rate. Future work would of course include continuing model development to incorporate the remaining KEs and KERs. A key feature to consider in future work would be the modeling of AMPA receptors on Neuron 3. Biologically, most glutamatergic synapses contain both AMPA and NMDA receptors, and AMPA receptors are known to be the primary drivers of synaptic transmission and membrane depolarization, which in turn lead to action potentials (Kandel et al., 2013b). Thus, modeling AMPA receptors on Neuron 3 to be used as the driving force for action potential generation would align more closely to what is seen biologically rather than using NMDA receptors alone. Additionally, activation of NMDA receptors is known to result in the modulation of AMPA and GABA receptors through calcium (Kapur, 2018). Incorporating the modeling of proteins involved in this modulation such as Phosphatase for AMPA upregulation and calmodulin-dependent protein kinase II (CaMKinase II) for $GABA_A$ downregulation in the model should be considered as it could potentially be a key factor in allowing the model to simulate the transition from cholinergic excitation to self-sustaining glutamatergic seizure activity (Kapur, 2018). Overall, further model refinement and parameter optimization is necessary in order for the model to align more closely with the observed data. With this in mind and the future work to the include the remaining KEs and KERs, the model would ideally be able to predict the neurodegeneration AO in response to AChE inhibition.

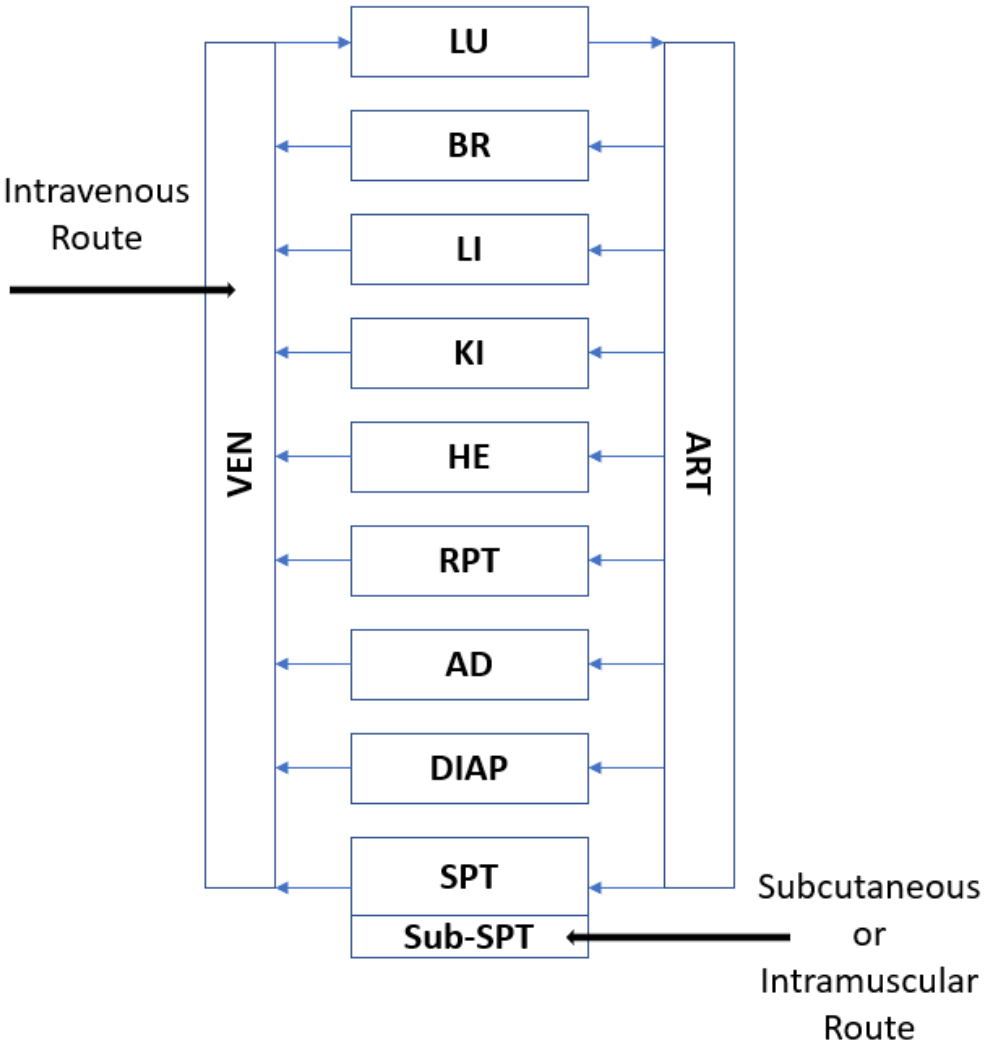

Figure 2.1. Schematic Diagram of the PKPD Model. Adapted from Figure 2 in Chen and Seng (2012). VEN = venous blood, ART = arterial blood, LU = lung, BR = brain, LI = liver, KI = kidney, HE = heart, RPT = rapidly perfused tissue, AD = adipose tissue, SPT = slowly perfused tissue, DIAP = diaphragm.

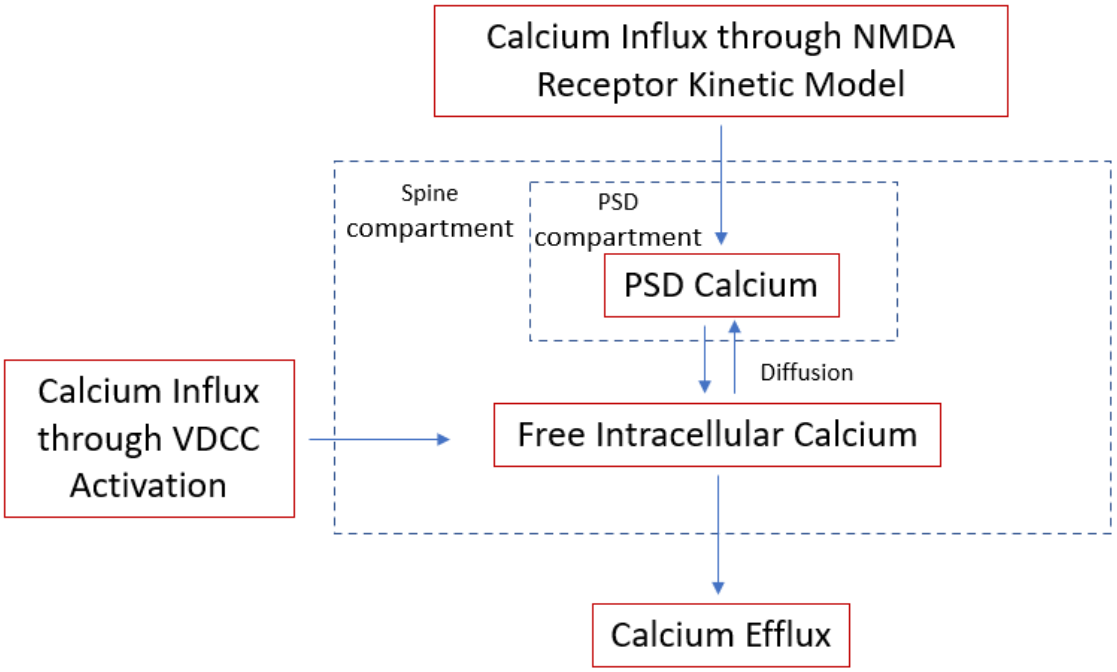

Figure 2.2. Schematic Diagram of the Calcium Model Influencing Intracellular Calcium Dynamics. Adapted from Hu et al. (2018). PSD = post-synaptic density. VDCC = voltage-dependent calcium channel.

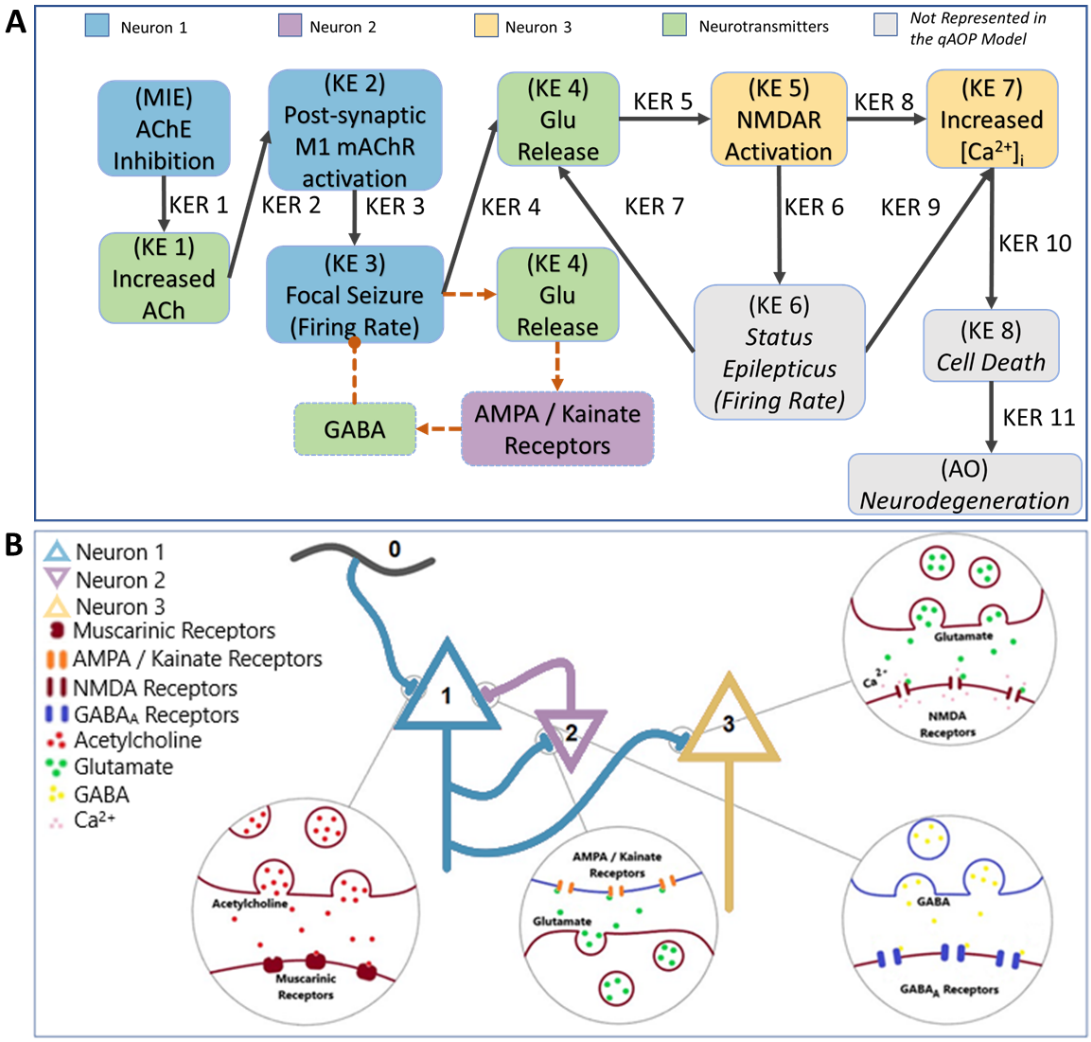

Figure 2.3. Schematic Diagram of the qAOP and Overall Model (A) Diagram of the conceptual model for the qAOP. KERs are aligned with the AOP 281. Dashed lines indicate feedback loops added to the qAOP model. *While the qAOP model simulates firing rate of Neuron 1, it is currently unable to determine onset of focal seizure. Additionally, status epilepticus, cell death, and neurodegeneration are not represented in the model. (B) Overall visual representation of the neurons, synapses, receptors, neurotransmitters, and ions present in the model.

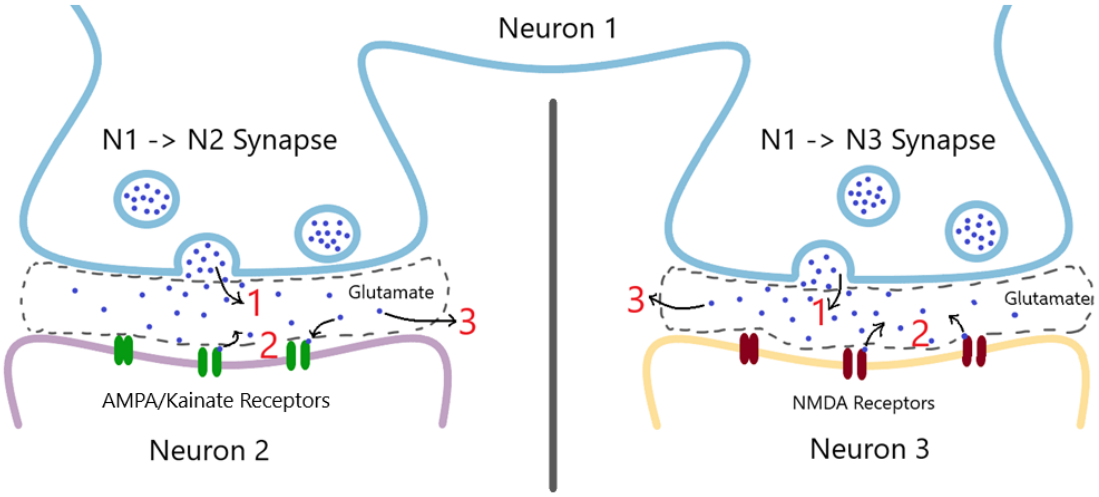

Figure 2.4. Conceptual Figure of Neuron Synapses in the Model. This shows the flow of glutamate (Glu) into and out of the pool (dashed lines). Neuron 1 (N1) forms two synapses, one with Neuron 2 (N2), as well as with Neuron 3 (N3). Glu enters the system through a release event at each action potential, releasing at both synapses (#1). Glu temporarily leaves the system through binding to either AMPA/Kainate or NMDA receptors (#2) , and through either diffusion, uptake, or degradation (#3).

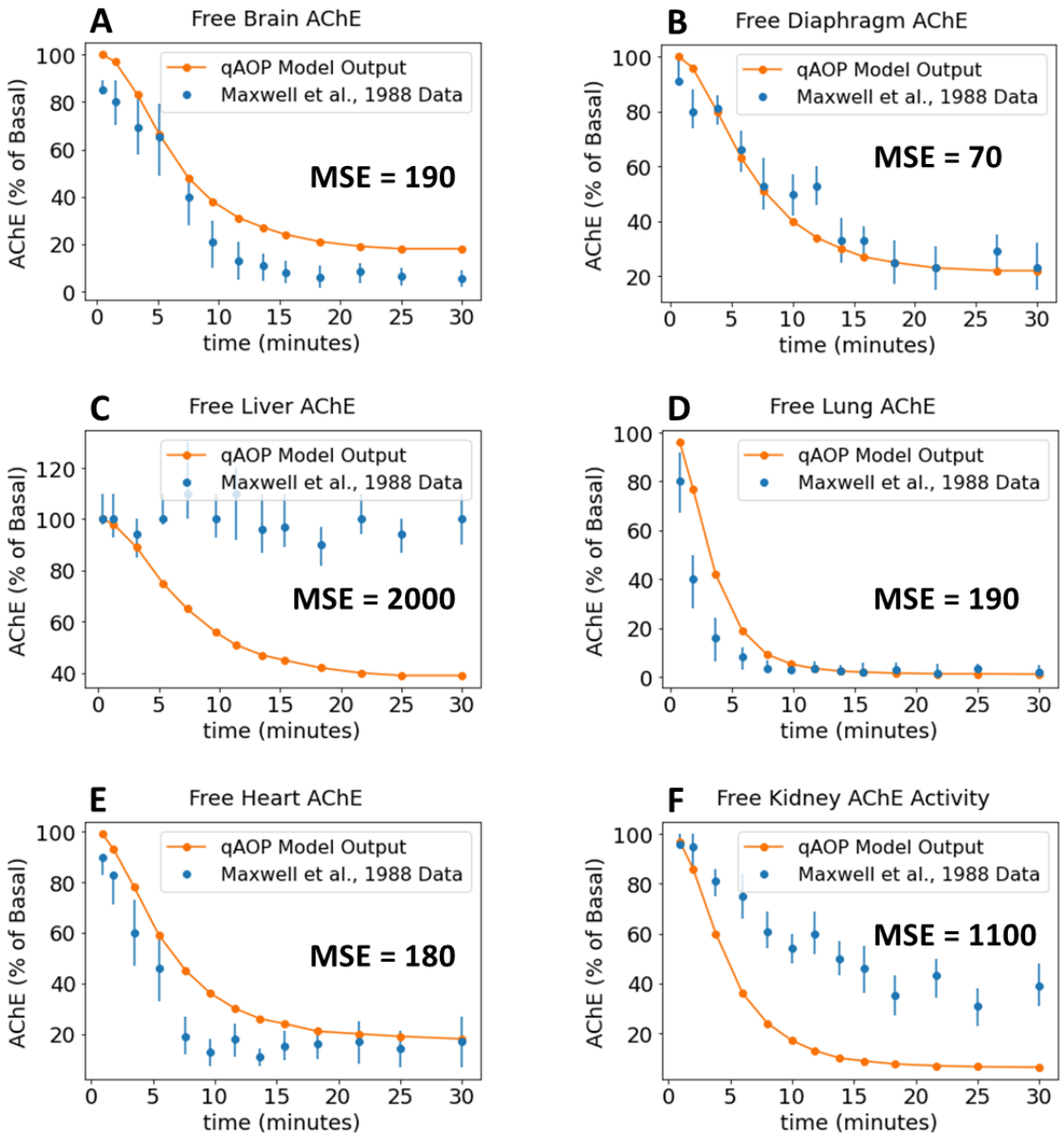

Figure 2.5. PKPD AChE Comparison with Maxwell et al. (1988) Data. These are model predictions with Maxwell et al. (1988) experimental measurements of the percent of free AChE following inhibition by intramuscular injection of 90 ug/kg of soman, simulating the same experimental conditions. AChE = Acetylcholinesterase. MSE = Mean Squared Error.

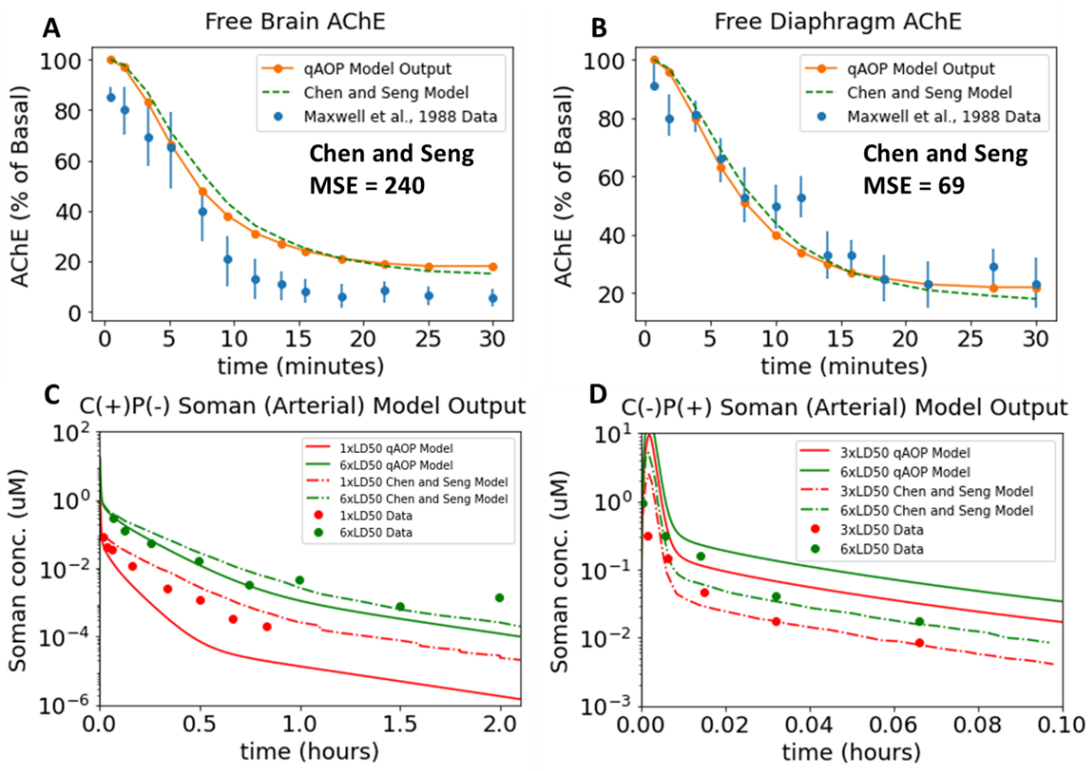

Figure 2.6. PKPD Model Output Comparison with Chen and Seng (2012). (A) Free Brain AChE model output versus Chen and Seng (2012) model output compared to experimental measurements in Maxwell et al. (1988), given 90 µg/kg soman IM. (B) Free Diaphragm AChE model output versus Chen and Seng (2012) model output compared to experimental measurements in Maxwell et al. (1988), given 90 µg/kg soman IM. (C) C(+)P(-) soman stereoisomer qAOP model predictions versus Chen and Seng (2012) model output compared to experimental measurements, given 82.5 µg/kg (1xLD50) and 495 µg/kg (6xLD50) soman IV. (D). C(-)P(+) soman stereoisomer qAOP model predictions versus Chen and Seng (2012) model output compared to experimental measurements, given 247.5 µg/kg (3xLD50) and 495 µg/kg (6xLD50) soman IV. Chen and Seng MSE = Mean Squared Error for the Chen and Seng output versus data from Maxwell et al. (1988).

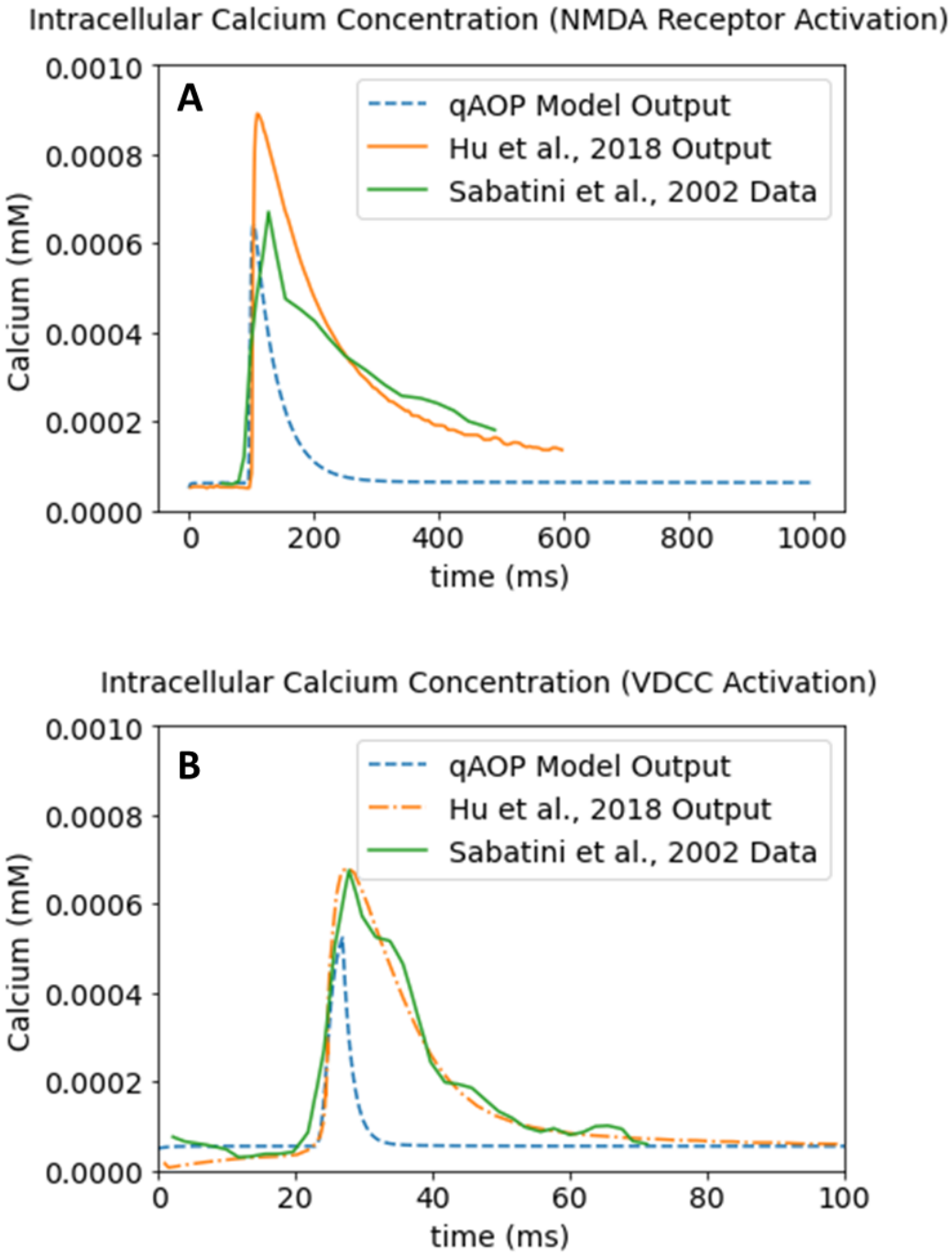

Figure 2.7. Calcium Model Comparison. (A) Comparison of qAOP model predictions with Sabatini et al. (2002) experimental measurements of intracellular calcium concentration in the dendritic spine of CA1 pyramidal neurons in response to NMDA receptor activation after a single Glu release event (Neuron 2 releasing Glu onto Neuron 3). (B) Comparison of qAOP model predictions with Sabatini et al. (2002) experimental measurements of intracellular calcium concentration in the dendritic spine of CA1 pyramidal neurons in response to VDCC activation after action potential induction of Neuron 3.

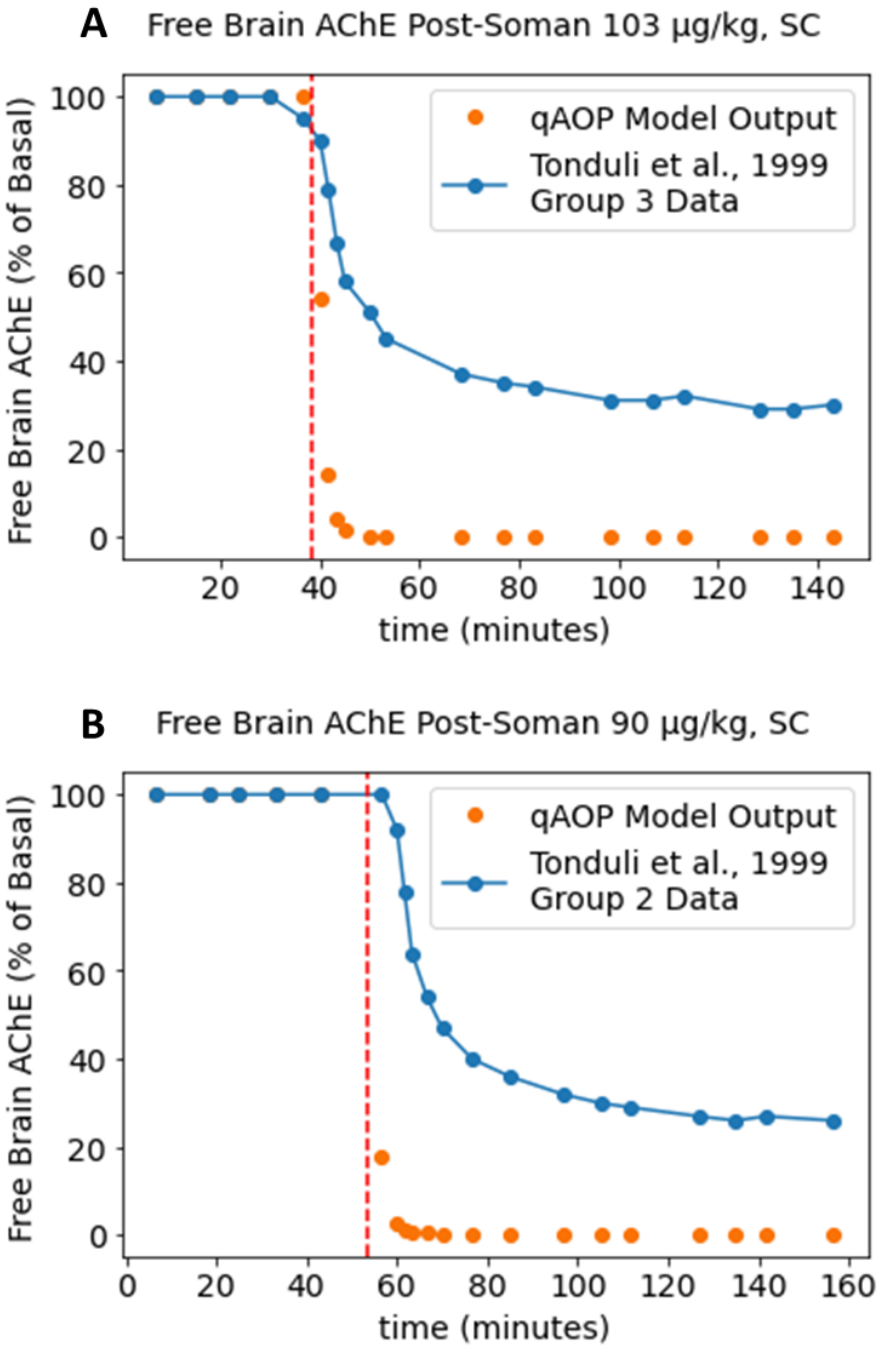

Figure 2.8. Model Predictions of Free Brain AChE Versus Tonduli et al. (1999) Data. The red-dashed line indicates the time at which soman was injected in both the model and the experimental data. (A) Model evaluation against AChE inhibition data from Tonduli et al. (1999) given SC injection of 103 µg/kg soman at approximately 38 minutes. (B) Model evaluation against AChE inhibition data from Tonduli et al. (1999) given SC injection of 90 µg soman/kg at approximately 53 minutes.

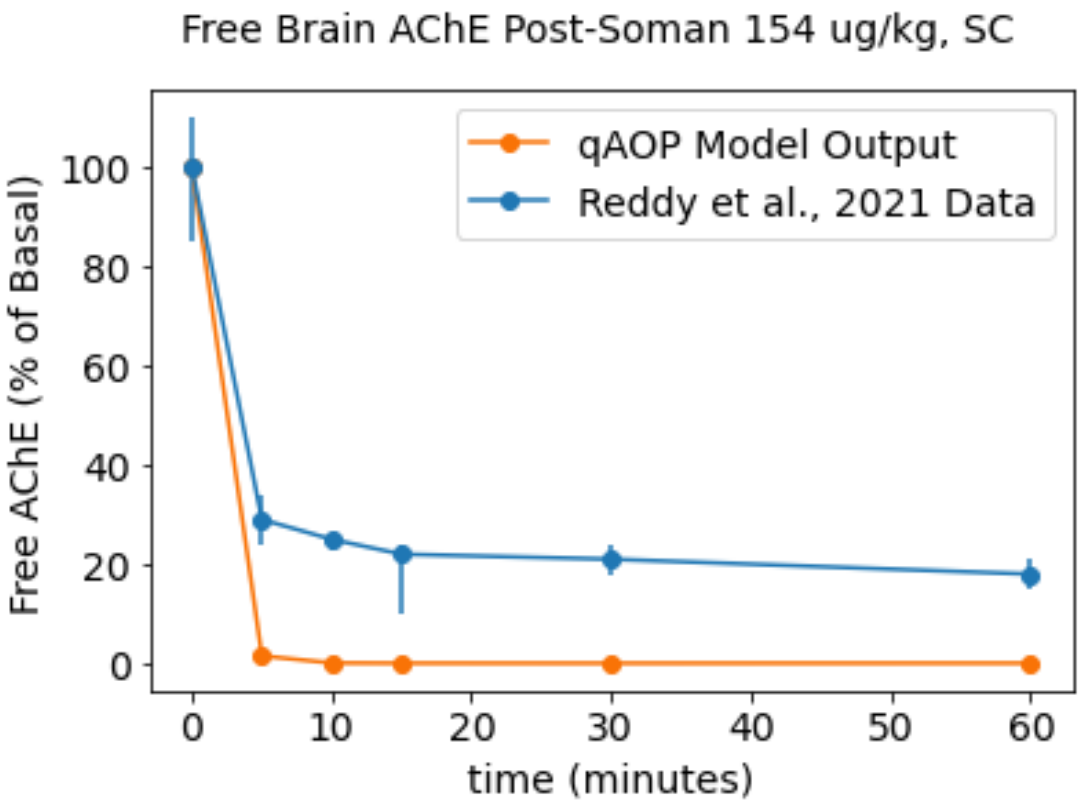

Figure 2.9. Model Predictions of Free Brain AChE Versus Reddy et al. (2021) Data. 154 µg soman/kg was injected SC and the model was evaluated against the data at the same timepoints from 0 to 60 minutes.

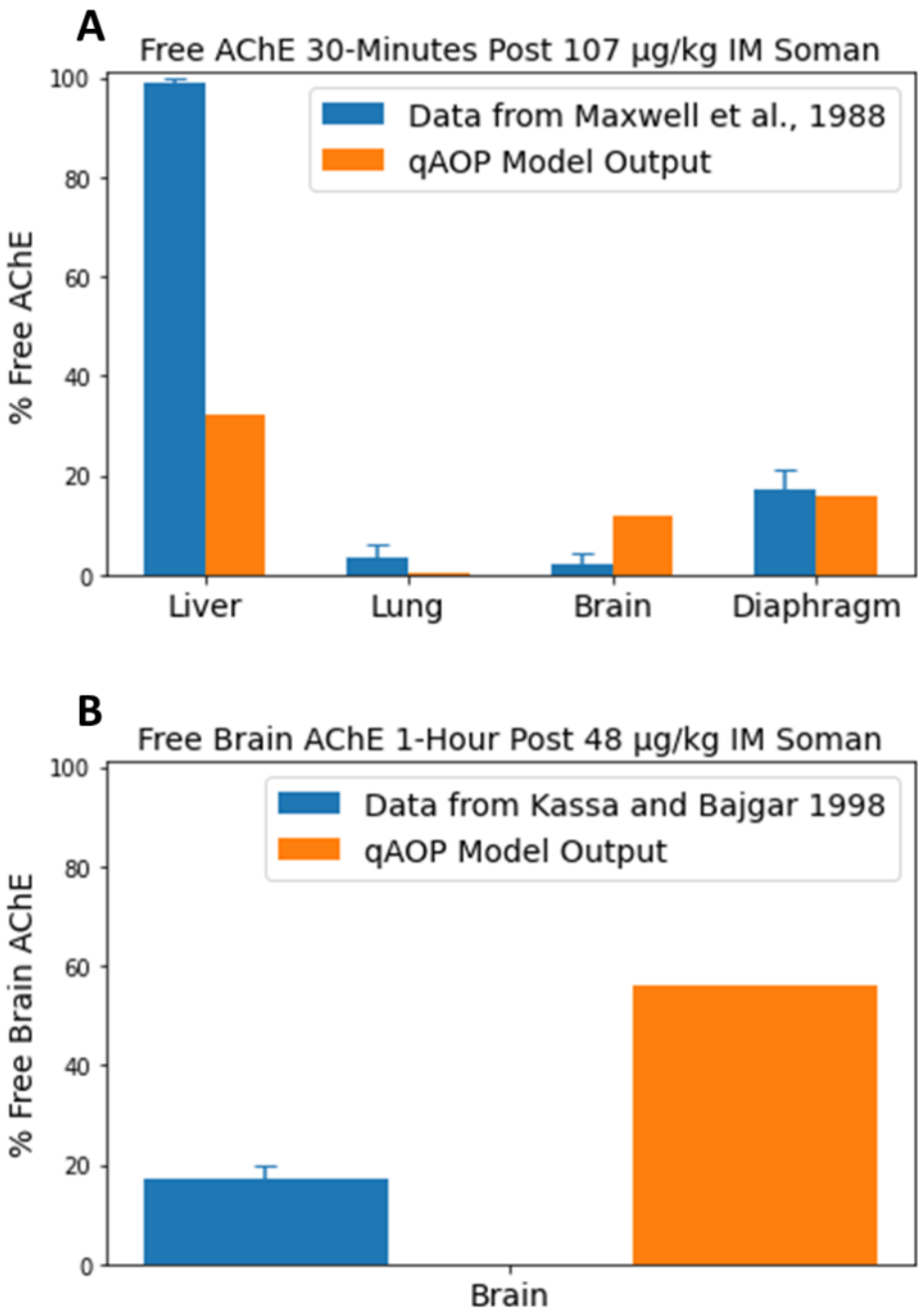

Figure 2.10. Model Predictions of Free Brain AChE 1-Hour Post-Soman Injection. This was compared against data provided by Maxwell et al. (1988) and Kassa and Bajgar (1998) under IM administration scenarios at the same timepoint. (A) Model predictions of free liver, lung, diaphragm, and brain AChE versus data from Maxwell et al. (1988) given an IM injection of 107 µg/kg soman. (B) Model predictions of brain AChE versus data from Kassa and Bajgar (1998) given an IM injection of 48 µg/kg soman.

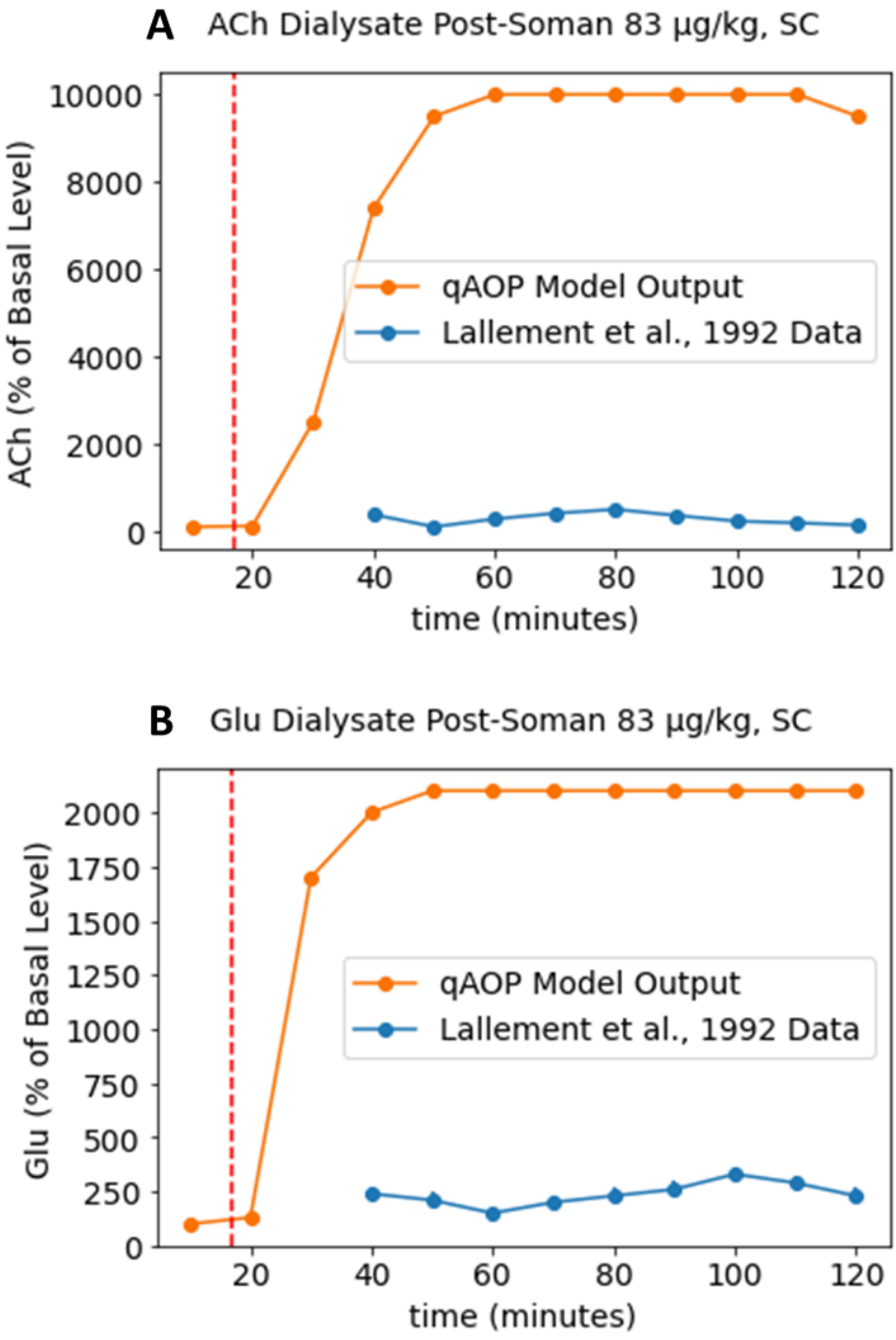

Figure 2.11. Dialysate Model Evaluation. Model predictions compared to experimental data from Lallement et al. (1992). The red dashed line indicates the time at which soman was injected (17 minutes). ACh = Acetylcholine. Glu = Glutamate. MSE = Mean squared error. (A) ACh dialysate as a percent of basal levels compared to observed data. Model Basal ACh = 1.4 mM, Data Basal ACh = 1.1e-6 mM. (B) Glu dialysate as a percent of basal levels compared to observed data. Model basal Glu = 4.5e-2 mM, data basal Glu = 2.9e-4 mM.

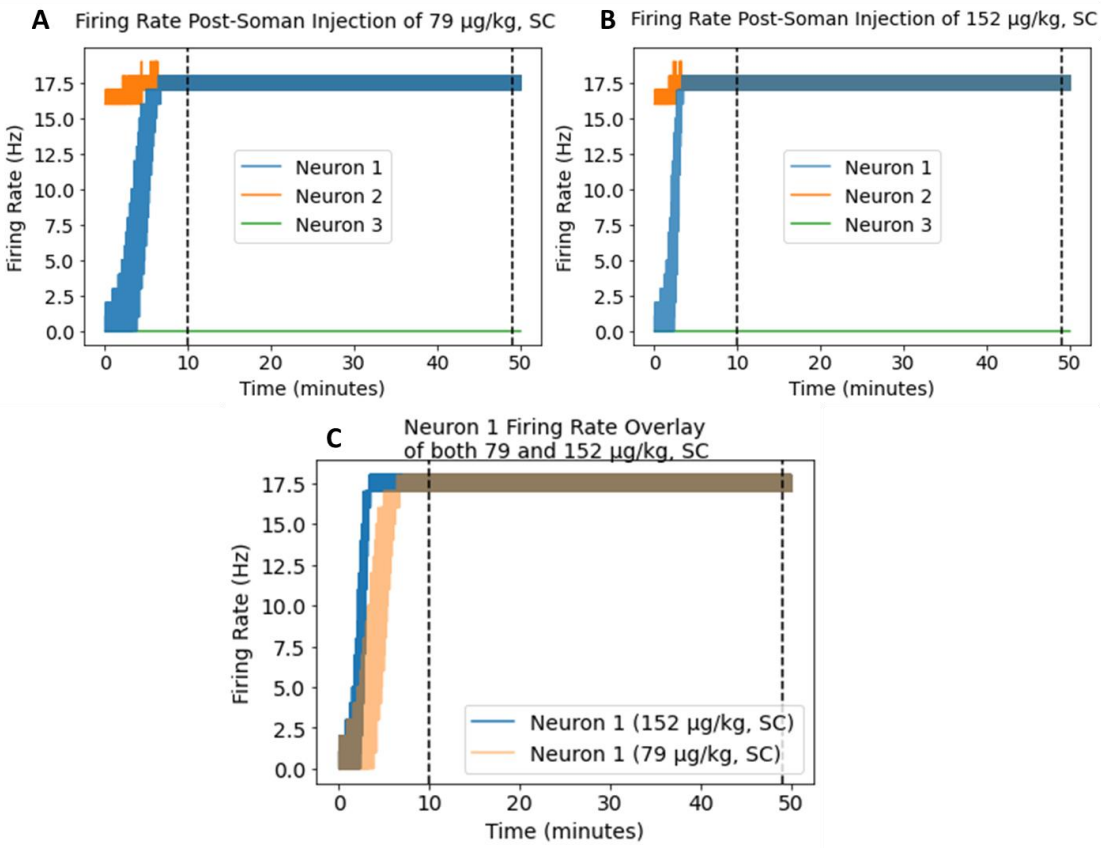

Figure 2.12. Changes in Firing Rates. This shows Neurons 1, 2 and 3 following SC injection of soman of either 79 or 152 µg/kg. Neuron 3 is currently not set to fire as described in the methods. The black dashed lines represent the total possible range of time (10-49 minutes post-soman injection) at which seizures were seen to occur based on the observed data in Tonduli et al. (1999). (A) Neuronal firing rates in response to 79 µg/kg soman, SC. (B) Neuronal firing rates in response to 152 µg/kg soman, SC. (C) Overlaying Neuron 1 firing rate under both conditions.

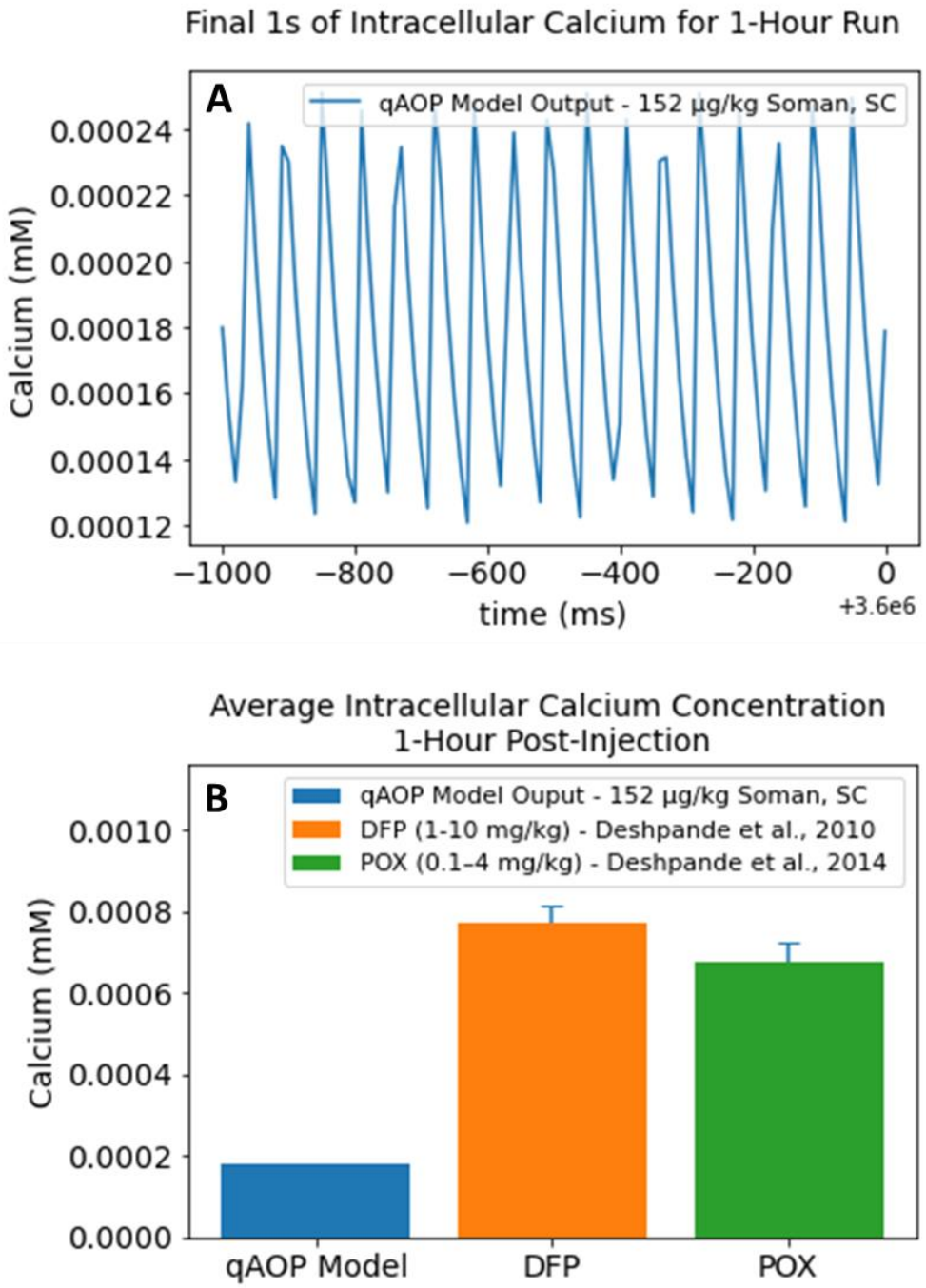

Figure 2.13. Calcium Model Evaluation. (A) Final 1s output of intracellular calcium 1-hour post-soman injection SC 152 ug/kg. (B) Bar graph comparing averaged output from A and data provided by Deshpande et al. (2010) and Deshpande et al. (2014), where intracellular calcium was measured 1-hour post-SE after injecting varying doses of either diisopropylfluorophosphate (DFP) or paraoxon (POX), both known organophosphates and AChE inhibitors.

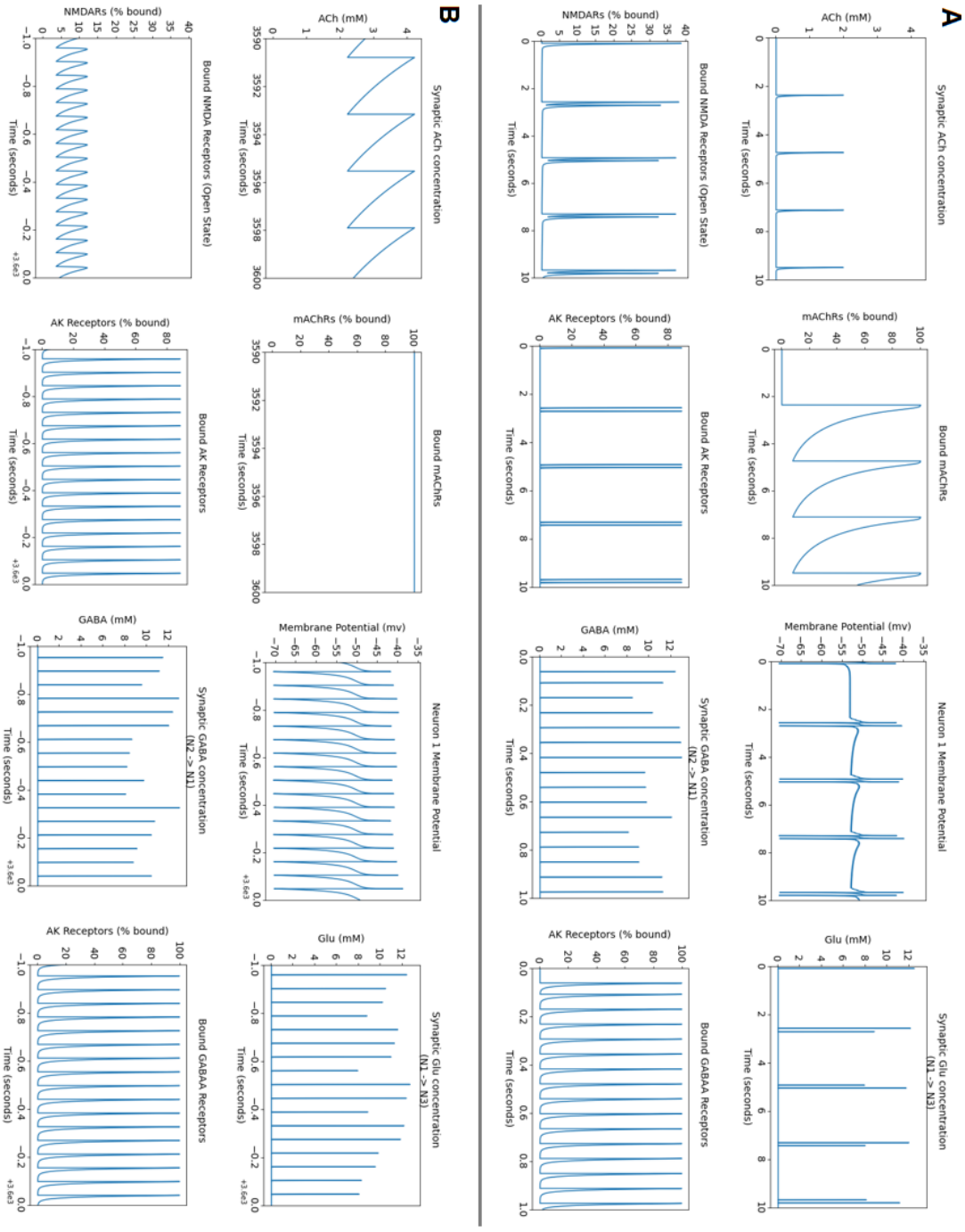

Figure 2.14. Model Output of Small Timescale Changes. This shows synaptic ACh concentration, bound mAChRs, membrane potential (Neuron 1), bound NMDARs, bound AK receptors, synaptic GABA concentration, and bound $GABA_A$ receptors after injection of 100 µg soman/kg, SC. (A) Small timescale changes within the first 1 or 10 seconds. (B) Small timescale changes within the final 1 or 10 seconds of the simulation.

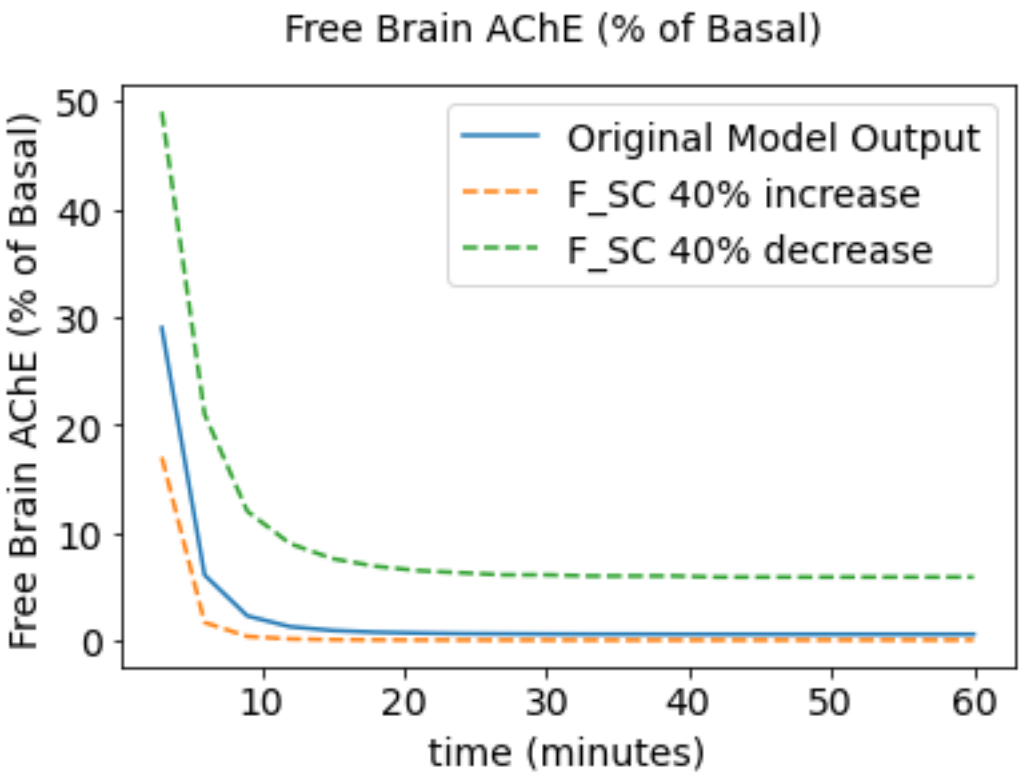

Figure 2.15. Changes in Free Brain AChE. This is over 1-hour post-soman SC injection of 100 µg/kg. This is given a ±40% change in the parameter F_SC. F_SC = The bioavailability constant for soman injected SC.

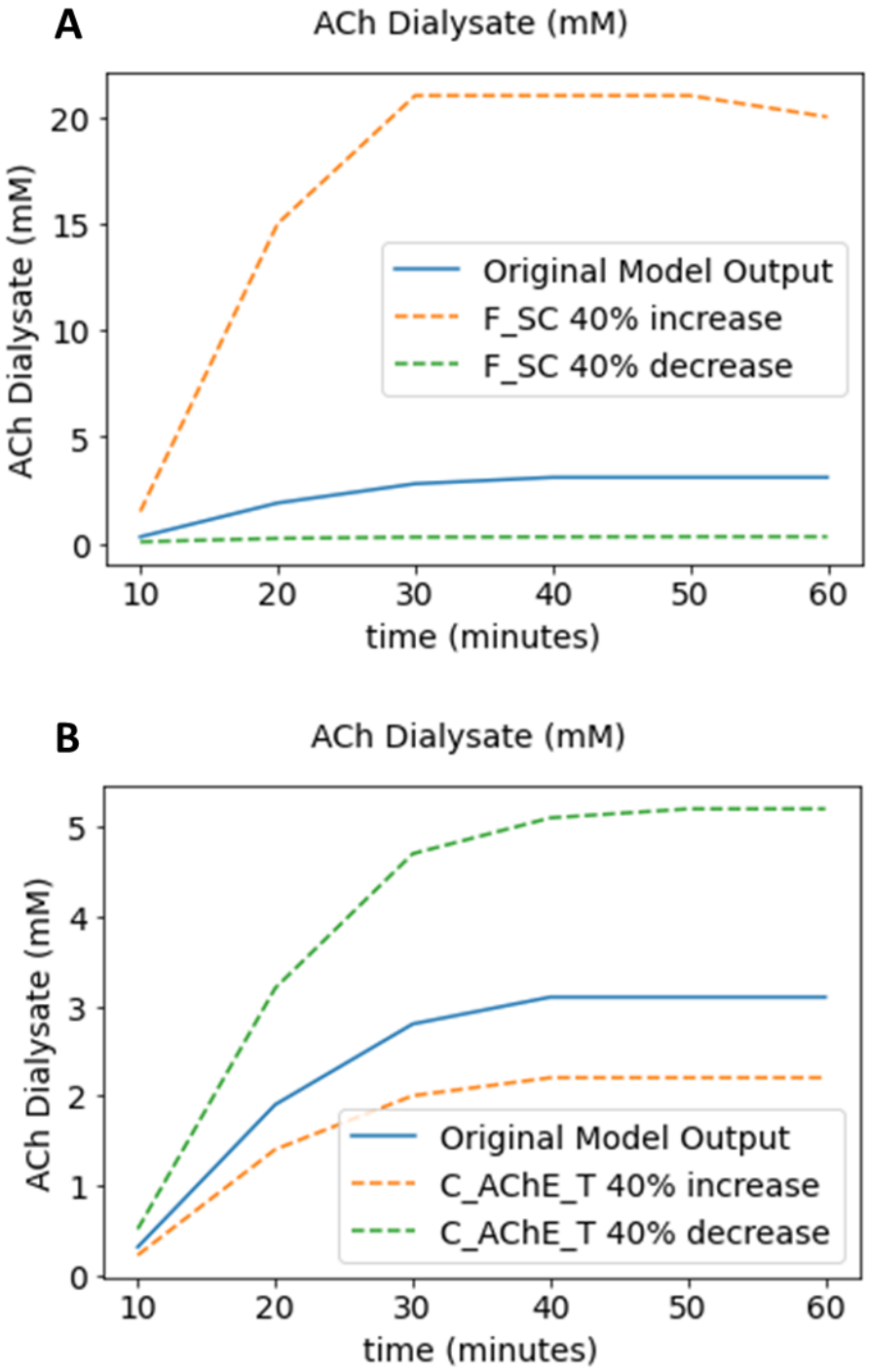

Figure 2.16. Changes in ACh Dialysate. This is 1-hour post-soman SC injection of 100 µg/kg. This is given a ±40% change in (A) F_SC, and (B) C_AChE_T. F_SC = The bioavailability constant for soman injected SC. C_AChE_T = The concentration of AChE in the synapse of the hippocampus.

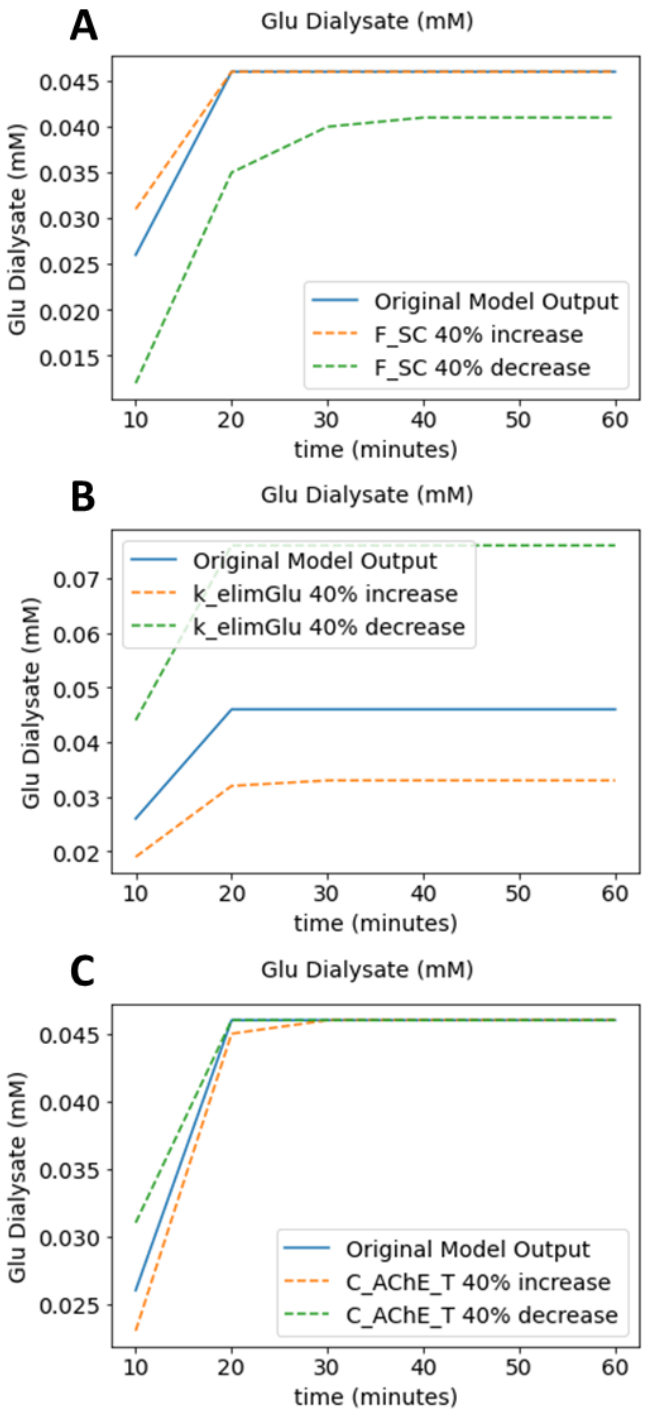

Figure 2.17. Changes in Glu Dialysate. This is over 1-hour post-soman SC injection of 100 µg/kg. This is given a ±40% change in (A) F_SC, (B) k_elimGlu, and (C) C_AChE_T. F_SC = The bioavailability constant for soman injected SC. k_elimGlu = First-order elimination rate of Glu in the synapse. C_AChE_T = The concentration of AChE in the synapse of the hippocampus.

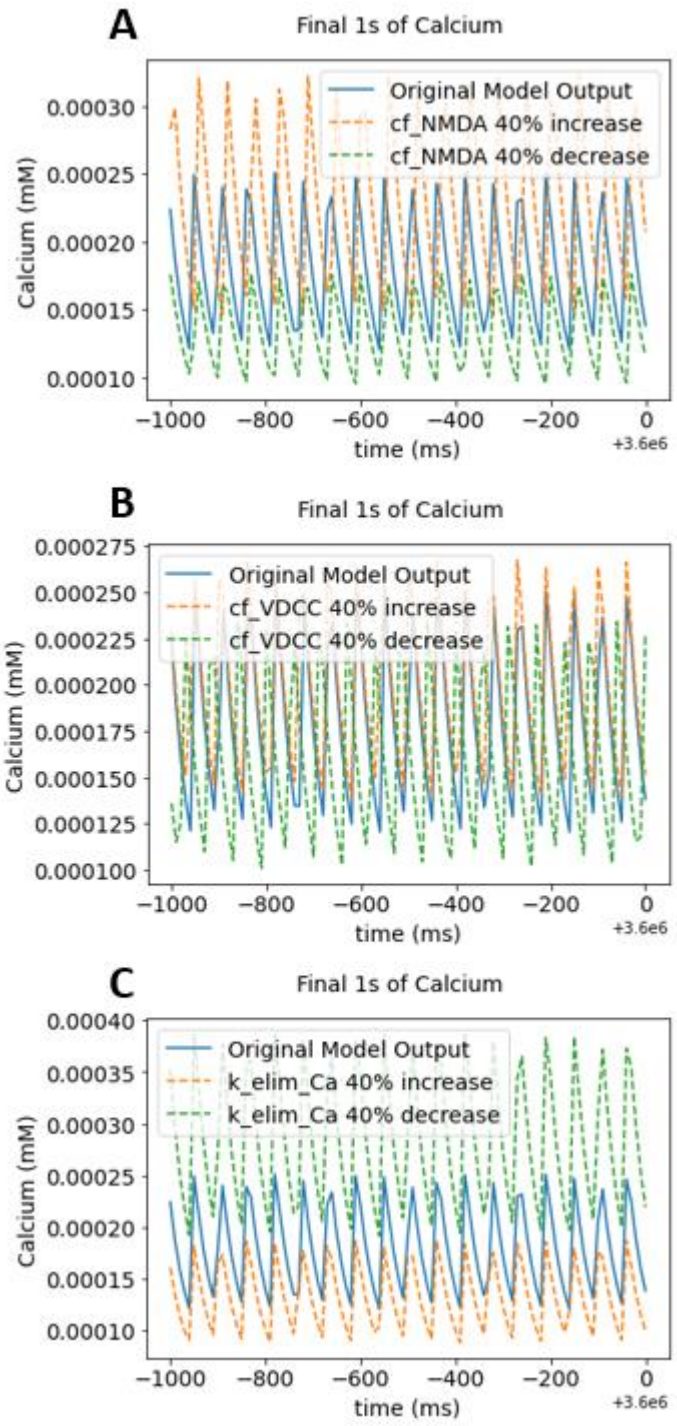

Figure 2.18. Changes in Intracellular Calcium in the Dendritic Spine. This is over the course of 1 second at the end of the model run, given a ±40% change in (A) cf_NMDA, (B) cf_VDCC, and (C) k_elim_Ca. cf_NMDA = NMDA current conversion factor. cf_VDCC = VDCC current conversion factor. k_elim_Ca = First-order elimination rate of intracellular calcium in the dendritic spine.

Table 2.1. List of Unknown Parameters. These were considered unknown if they were created independently of prior models, were modified to better fit experimental data, or had no biologically relevant range of values. The potential values, where indicated, describe other reasonable values from the referenced authors, and is given to provide an estimate for the possible range of values for that unknown parameter.

Unknown Parameter	Value	Potential value	Description	Reasoning and Assumptions (If applicable)
K_SYN	3.06E-12 uM/ms	N/A	AChE rate of synthesis	Original units unknown due to discrepancy (Chen and Seng (2012)).
K_a_SC	3.17E-05 ms^{-1}	1.16e-6 ms^{-1}	Subcutaneous absorption rate constant	Based on Guinea Pig data, assumed to be equivalent in rats (Chen and Seng (2012)). Potential value: K_a_SC recalculated using the same methods, instead using data by Tonduli et al. (1999)
F_SC	0.68 (unitless)	N/A	Subcutaneous bioavailablity	Subcutaneous assumed equivalent in rats, from Chen and Seng 2012)
C_AChE_T	0.0003 mM	N/A	Synaptic concentration of AChE	Striatal concentration of AChE in baboons and humans, assumed to be similar in rats (Blomqvist et al., 2001)
C_M1_T	0.0225 mM	N/A	Synaptic concentration of M1 mAChR	Calculated from the average density of M1 mAChRs over a neuron, and assuming similar concentrations in a synapse
k_elimGlu	5 ms^{-1}	10 ms^{-1}	Glu clearance from synapse	Modified from Destexhe et al., 1994b to better fit experimental data, originally set to 10.
k_elimGABA	5 ms^{-1}	10 ms^{-1}	GABA clearance from synapse	Modified from Destexhe et al., 1994b to better fit experimental data, originally set to 10.
gabaRelease	13 mM	N/A	Concentration of the instantaneous release of GABA	Assumed an equivalent release as Glu from Destexhe et al., 1994b.
C_GABAA_T	0.11 mM	N/A	Concentration of GABA_A Receptors in the synapse	Assumed an equivalent concentration to AK receptors from Destexhe et al., 1994b
A_surfArea	0.05 um^2	N/A	Surface area between the PSD and remaining spine volume	Estimated from Naoki et al., 2005
d_dist	0.7 um	N/A	Distance between the midpoints of the PSD and the spine compartments	Estimated from Naoki et al., 2005
cf_NMDA	6 (unitless)	N/A	NMDA current conversion factor	Calibrated to fit experimental intracellular calcium concentration changes (Sabatinit et al., 2002)
cf_VDCC	2.3e4 (unitless)	N/A	VDCC current conversion factor	Calibrated to fit experimental intracellular calcium concentration changes (Sabatinit et al., 2002)
k_elim_Ca	0.7 ms^{-1}	N/A	First-order elimination rate of intracellular calcium	Calibrated to fit experimental intracellular calcium concentration changes (Sabatinit et al., 2002)

Table 2.2. Relative Sensitivity of Unknown Parameters at 30-Minutes. Following 100 µg soman/kg soman, injected SC. This is for the free brain AChE, ACh dialysate, and Glu dialysate endpoints. Average intracellular calcium was only recorded at 60 minutes post exposure therefore it is not shown here. *Decreasing k_elimGABA by 40% led to model instability and crashing, however the parameter is insensitive when increased by 40%, resulting in no changes in model output. **The value 0.0446 for both K_SYN and K_a_SC is likely due to rounding error after rounding to two significant figures of model output at this timepoint, and therefore should be considered equivalent to 0. The shaded cells indicate the parameters that may have an impact on the endpoints, unshaded cells are expected to have a value of 0 as there is no feedback in the model that would result in changes to the above endpoints.

Relative Sensitivity at T = 30 Minutes			
	AChE	**ACh**	**Glu**
K_SYN	0	0.0446**	0
K_a_SC	0	0.0446**	0
F_SC	12.2	9.24	0.163
C_AChE_T	0	1.21	0
C_M1_T	0	0	0
k_elimGlu	0	0	1.17
k_elimGABA	N/A*	N/A *	N/A *
gabaRelease	0	0	0
C_GABAA_T	0	0	0
A_surfArea	0	0	0
d_dist	0	0	0
cf_NMDA	0	0	0
cf_VDCC	0	0	0
k_elimCa	0	0	0

Table 2.3. Relative Sensitivity of Unknown Parameters at 60-Minutes. Following 100 µg/kg soman injected SC. This is for the free brain AChE, ACh dialysate, Glu dialysate, and average intracellular calcium endpoints. *Decreasing k_elimGABA by 40% led to model instability and crashing, however the parameter is insensitive when increased by 40%, resulting in no changes in model output. **The value 0.0417 in K_SYN is likely due to rounding error after rounding to two significant figures of model output at this timepoint, and therefore should be considered equivalent to 0. The shaded cells indicate the parameters that may have an impact on the endpoints, whereas unshaded cells are expected to have a value of 0 as there is no feedback in the model that would result in changes to the above endpoints.

Relative Sensitivity at T = 60 Minutes				
	AChE	**ACh**	**Glu**	**Calcium**
K_SYN	0.0417**	0	0	0
K_a_SC	0	0	0	0
F_SC	12.2	7.94	0.136	0
C_AChE_T	0	1.21	0	0
C_M1_T	0	0	0	0
k_elimGlu	0	0	1.17	0
k_elimGABA	N/A*	N/A*	N/A*	N/A*
gabaRelease	0	0	0	0
C_GABAA_T	0	0	0	0
A_surfArea	0	0	0	0
d_dist	0	0	0	0
cf_NMDA	0	0	0	0.694
cf_VDCC	0	0	0	0.278
k_elimCa	0	0	0	1.04

CHAPTER 3

FROM QUALITATIVE TO QUANTITATIVE AOP: A CASE STUDY OF NEURODEGENERATION

3.1 Preface

The following text has been adopted from a published paper, Sinitsyn et al. (2022), and is included here as it discusses the overall challenges faced with regard to quantitative model development in the context of AOP 281. Specifically, it focuses on the transition from qualitative to quantitative AOP and provides overall recommendations made for the facilitation of qAOP development. As this was published in March of 2022, the text below presents a perspective from an earlier stage in the development process. There have since been changes made to both the AOP and qAOP, therefore, some of the text presented will not reflect the current state of the AOP and qAOP. However, the overall lessons learned, and recommendations made remain valid and pertinent. Presenting the text as is additionally demonstrates how the model has evolved over time, allowing the reader to compare the methods described below to the above methods and final model presented in the previous chapter.

3.2 Introduction

The ability to predict the potential hazard of chemicals is crucial to better understand and protect both human health and ecological receptors. Regardless of numerous international efforts to improve predictions, many challenges remain. The Adverse Outcome Pathway (AOP) framework (Ankley et al., 2010) is an increasingly accepted approach to link biological pathways at the molecular level to adverse outcomes. While the development of AOPs has increased substantially, the need for quantitative approaches using the AOP framework remains a challenge. It took years to develop what could be considered the first quantitative AOP (qAOP), and several approaches have been proposed to date (Conolly et al., 2017; Perkins, Gayen, et al., 2019). The development of qAOPs is arguably one of the main challenges remaining within the AOP framework, nevertheless necessary in order to improve risk and hazard prediction.

The development of a qAOP logically follows AOP development given its function as a mathematical representation of the key event relationships (KERs) in an AOP. Different approaches have been used including: (i) fitting functions to key event (KE) data bounding a KER(s) (response-response method) (Doering et al., 2019; Doering et al., 2018; Song et al., 2020; Zgheib et al., 2019); (ii) biologically based mathematical modeling using ordinary differential equations (aka systems biology modeling) (Conolly et al., 2017; Gillies et al., 2016; Muller et al., 2015; Zgheib et al., 2019); and recently (iii) a causal modeling approach using a Bayesian Network (Burgoon et al., 2020; Jeong et al., 2018; Moe et al., 2021; Paini et al., 2021; Perkins, Ashauer, et al., 2019; Zgheib et al., 2019). Bayesian Networks, in particular, are useful for describing complex AOPs involving multiple pathways leading to an AO as long as there are no feedback loops. The KEs of the AOP can be taken as the nodes of the network and can even be used to model time dependencies in the form of Dynamic Bayesian Networks (Zgheib et al., 2019). Note that in this article, response-response relationships are defined as mathematical functions determined by a regression analysis, whereas in other publications, e.g., Paini et al. (2021), the response-response relationship is defined more broadly to include biologically based models that quantitatively relate two KEs. The merits and pitfalls of the response-response approach and biologically based modeling have been discussed (Foran et al., 2019; Schultz & Watanabe, 2018; Spinu et al., 2020; Zgheib et al., 2019), but a significant barrier to the development of qAOPs in any form is the availability of quantitative data amenable for mathematical model development.

The goal of this article is to improve the efficiency of converting a qualitative AOP into a qAOP. A workflow for qAOP development, electronic resources, and three case studies are described in Paini et al. (2021) based on a recent Lorentz workshop. In the following, challenges to qAOP development were identified by reviewing AOPs with WPHA/WNT[1] endorsement by the

[1] Working Party on Hazard Assessment / Working Group of the National Coordinators of the Test Guidelines Programme

Organisation for Economic Co-operation and Development (OECD, 2021) in the AOPWiki[2], and through a case study on developing a qAOP for acetylcholinesterase (AChE) inhibition leading to neurodegeneration (Conrow et al., 2021). As the construction of AOPs are an ever-evolving process, and as we reviewed these AOPs in November 2021, it should be noted that the information contained in the list of endorsed AOPs and the information presented inside the AOPs may change over time, and what was available at the time of this review may not reflect what is available in the future. We selected AOPs with WPHA/WNT endorsement as it provided us with a relatively broad and manageable set of AOPs to review.

3.3 Review of AOPS with OECD Status

We performed a review of AOPs with OECD status to determine how readily other KER descriptions would facilitate conversion from AOP to qAOP, and explore any similar challenges shared between AOPs. Determining confidence in an AOP and its associated KERs is established through weight of evidence (WoE) evaluations based on modified Bradford-Hill criteria involving biological plausibility, empirical support, and quantitative understanding (OECD, 2018). The process of determining confidence through said criteria has been discussed previously (Becker et al., 2015), and while confidence in the supporting data may be considered high for a qualitative AOP, the next step of converting to a qAOP requires a more specific, quantitative set of data. Our goal in this case was to review the cited quantitative data and categorize the AOPs based on how readily a qAOP could be developed based on the presentation of information and WoE for the quantitative understanding section. Our review of AOPs with OECD status included only those that provided a WoE evaluation for KERs (see Table 3.1).

When quantitative data are available for a KER, a question arises as to how to go about extracting it for use in quantitative model development. Our review found that quantitative data are presented in a variety of ways, ranging from text with cited references to data presented in a

[2] https://aopwiki.org/

tabulated form along with relevant figures. The majority of the AOPs reviewed currently contain text with cited references in the KER quantitative understanding section, although AOP 131 supplements some of the text with a figure (Farhat et al., 2021). In contrast, AOP 3 provides text and relevant figures for all KERs and includes tables of quantitative data (Bal-Price et al., 2019). It is important to note that while the presentation of data in the quantitative understanding section of an AOP varies depending on the AOP in question, it does not reflect an AOP's capability to be converted to a qAOP. For example, AOP 25, Aromatase Inhibition Leading to Reproductive Dysfunction, has a qAOP while containing only text with cited references in the quantitative understanding sections (Villeneuve, 2021).

3.4 Case study: AChE Inhibition Leading to Neurodegeneration

AChE inhibition leading to neurodegeneration is AOP 281 in the AOP Wiki (Conrow et al., 2021) and is currently under development (see Figure 3.1). The molecular initiating event (MIE) is AChE inhibition resulting in an excess of acetylcholine (ACh) in the synapse (KER 1). The build-up of ACh overactivates muscarinic acetylcholine receptors (mAChR) within the brain (KER 2), initializing local (focal) seizures (KER 3). Spreading of the focal seizure through glutamate release (KER 4) and subsequent activation of n-methyl-D-aspartate (NMDA) receptors (KER 5) propagates the excitotoxicity and leads to elevated intracellular calcium levels (KER 6), status epilepticus (KER 7), and ultimately cell death (KER 8) and neurodegeneration (KER 9). Additionally, status epilepticus induces further release of glutamate (KER 10), forming a positive feedback loop. The following text outlines our methods used during the conversion process, and the challenges we encountered.

3.5 qAOP Development Methods

3.5.1 Literature Review

The first step in creating the qAOP was to examine the studies and data obtained during the construction of the qualitative AOP. We performed a comprehensive literature review that included the qualitative evidence previously obtained and examined additional studies found

through publicly available databases, totaling over 200 papers examined. Concluding the review, we gathered and grouped the data into two categories: (i) model development, and (ii) model evaluation. Ideally, model development data covers at least two adjacent key events, and if there is an abundance of data meeting this criterion then a dataset(s) could be set aside and used to evaluate the model's predictive ability. In cases where data are reported for non-adjacent KEs, two outcomes are possible: (i) If the qAOP is being developed on response-response relationships and all KEs need to be in the qAOP, then these data should be used for evaluating the qAOP. (ii) In a biologically based modeling context, data for non-adjacent KEs can be used for model development. However, as an example, given two datasets, one that contains data for three adjacent KEs, and another that only contains data for the first and third (non-adjacent) KE, we would use the first data set for model development and the latter for model evaluation.

3.5.2 Quantitative Model Development – Data Needs

We initially planned to use a response-response relationship approach for the construction of a modular qAOP, however, while there were data available for KER 1, data to develop response-response relationships for the remaining KERs were not available. Thus, we chose a hybrid approach that would combine a response-response model for KER 1 with a biologically based model spanning KERs 2 through 10. Response-response relationships are built upon dose-response data for adjacent KEs, and linear regression analysis was used KER 1. For the remaining KERs, response-response data were sparse, and a feedback loop in the AOP (KERs 5,6,7,10) precludes the use of response-response modeling and necessitates the development of a biologically based model. Of the papers reviewed for qAOP model development, approximately 10 studies in the primary literature resulted in useable quantitative data for model development (Falkenburger et al., 2010; Kim et al., 2003; Kosasa et al., 1999; Mergenthal et al., 2020; Michaels & Rothman, 1990), and model evaluation (Lallement et al., 1992; Marks et al., 1996; McDonough & Shih, 1997; Miller et al., 2015; Reddy et al., 2021).

Studies reporting data for non-adjacent KEs, while useful for model evaluation, are not ideal for developing quantitative models for KERs. For example, Miller et al. (2015) reported percent

AChE inhibition (MIE) and hippocampal volume loss, but did not report data for any KEs adjacent to these endpoints. In AOP 281, hippocampal volume loss is a potential measure of the neurodegeneration adverse outcome. Though it may not be the best measure to use in a response-response relationship, a biologically based model could predict this endpoint among other indicators of neurodegeneration and utilize the study for model evaluation. Similarly, Lallement et al. (1992)reported measurements of ACh and glutamate. In this case, we could not determine a response-response relationship relating ACh concentration to glutamate. However, the data can be used to evaluate predictions from a biologically based model that incorporates mechanistic processes representing the intermediate KEs. We acknowledge that the published studies discussed were not designed with qAOP model development in mind, though they provide as examples of where changes in experimental design and increased research funding could yield a more comprehensive understanding of underlying biological mechanisms.

Biological systems are often regulated by feedback loops, which requires development of a time-dependent biologically based model in contrast to a response-response relationship (Zgheib et al., 2019). At “steady-state”, when time dependencies are removed and derivatives with respect to time are set to zero, a response-response relationship could be used to relate the input into a feedback loop with the output, essentially ignoring the mathematical dynamics of the feedback loop (Zgheib et al., 2019). However, when a system is perturbed, and a feedback loop exists, a time-dependent biologically based model is needed to capture the system dynamics. Thus, biologically based models benefit from time series measurements of the associated KEs to identify model parameter values. In AOP 281, KERs 5, 6, 7, and 10 form a positive feedback loop requiring data to uniquely define model equations and parameter values. Response-response models work for linear pathways with one input and one output and are implemented sequentially through an AOP (Foran et al., 2019). In contrast, feedback loops involve more than one input/output for a KE (e.g., two inputs into the glutamate release KE and two outputs from the increased intracellular calcium KE), resulting in a non-linear pathway. As feedback loops are a

commonly used regulatory mechanism in nature, methods to develop quantitative models should be encouraged instead of avoided.

In the context of high-throughput chemical toxicity applications, KE measurements need to be made quickly and inexpensively. Some studies report excellent data obtained through sophisticated measurement techniques that are not practical for use in chemical toxicity testing and risk assessment due to cost and time constraints. Such techniques might be described as part of the evidence in a KE description though the technique is impractical for measuring a KE in high-throughput toxicity testing. With respect to the status epilepticus KE, researchers used quantitative MRI to predict hippocampal damage based on changes in the structure and volume of the hippocampus after inducing status epilepticus through overactivation of mAChR by pilocarpine (Choy et al., 2010). While the data obtained are informative, the tools (i.e., the MRI) required are likely to be costly and impractical for toxicity testing applications. Ultimately, this issue can be applied more generally to the time and financial costs required of in vivo experiments compared to in vitro.

Distribution of available data throughout an AOP differs for KERs. In the context of AOP 281, KER 1 was supported quantitative data that resulted in a response-response relationship. In contrast, data to develop a response-response relationship for KER 2 were not found. Similar data availability or lack thereof can be seen in many other AOPs. As an example, the quantitative understanding section of AOP 3 ranges from low to high depending on the KER in question (Bal-Price et al., 2019). This uneven distribution of data can be restrictive and prevent model developers from working with a single modeling approach to develop a qAOP. Thus, research funding that supports the collection of data for multiple (adjacent) endpoints in an AOP would facilitate qAOP model development tremendously.

3.5.3 Quantitative Model Development – Interspecies Differences in Biological Response

Consideration should also be given to interspecies differences in response to chemical stressors (Celander et al., 2011). Ideally, there should be equivalent measurable responses between the target species and the animal model(s) or in vitro assays that provide data. In the

case of AOP 281, we started with rat data because there were significantly more studies available across the AOP than other animal models. By definition, AOPs are independent of chemical stressor, however data required to develop a qAOP are obtained from in vivo and/or in vitro experiments using chemical(s), and interspecies differences in the measured responses may occur. For example, in response to OPs, rats respond similarly to humans, though they have a 3-6 fold higher LD_{50} compared to humans when administered sarin intravenously, and guinea pigs have a 1.7-fold higher LD_{50} (Pereira et al., 2014). Pereira et al. attribute the fold difference in LD_{50} values to differences in OP metabolism between species, and quantitatively, this can be addressed through toxicokinetic modeling and methods to quantify measurement uncertainty and biological variability (Bernillon & Bois, 2000; Gelman et al., 1996; Jager, 2021). In terms of our qAOP, guinea pig data may be better suited for predicting human responses, but the data spanning the qAOP are insufficient. Thus, we will rely upon data from other species and use principles of interspecies extrapolation and allometric scaling (Davidson et al., 1986) as needed. For regulatory use, interspecies differences in biological responses could be quantified along with measurement uncertainty and biological variability using methods cited above.

Reducing the number of animals used in toxicity testing is a benefit of new approach methodologies such as in vitro assays and in silico models. Given the considerations above regarding interspecies differences, a wider array of in vitro assays focused on non-model organisms should be developed for ecotoxicology purposes(Hecker, 2018), and to provide a knowledge base that will improve our quantitative understanding of interspecies differences in biological response.

3.5.4 Quantitative Model Development – Reuse of Quantitative Models

Accessibility and transferability of established quantitative models are important factors to consider for accelerating qAOP development. Currently, there are two models that simulate cellular response to mAChR activation (Greget et al., 2016; Mergenthal et al., 2020), which could be extended for use in our qAOP. Mergenthal et. al (2020) describe a computational model of cholinergic modulation of CA1 pyramidal cells developed in the NEURON simulation

environment, spanning KERs 2 to 3, while Greget et. al (2016) describes a simulation of a CA1 hippocampal cells responding to OP-induced neurotoxicity, spanning KERs 1 to 3. However, the model by Greget et al. (2016) was not accessible, and the NEURON simulation environment is too specialized for our qAOP. Thus, we will use Mergenthal et al. (2020) as a reference for KERs 2 and 3 to construct a biologically based model spanning KERs 2 to 10. The reuse of existing models can dramatically improve the pace of qAOP development, though access and cross-platform transferability are of concern. Additionally, models developed in proprietary or unfamiliar software can be restrictive to newer model developers. Tools built with user-friendly, open-source software and data exchange formats such as Systems Biology Markup Language (Hucka et al., 2003) are possible solutions.

3.6 Discussion

Overall, the process of converting an AOP to a qAOP is time and resource-intensive and requires an abundance of quantitative data for the associated KERs. Some of the challenges presented above are not expected to be resolved for the foreseeable future. Costly measurements and the uneven distribution of data will remain an issue and will decrease in significance over time if and when new methods are developed or when research bridges the knowledge gaps in areas lacking in quantitative understanding. A recommendation for these challenges would be best aimed toward funding agencies placing additional funding into the areas identified by modelers to be lacking in data. Below are four additional recommendations pertaining to the remainder of the challenges.

Regarding the review of the AOPs with OECD status and their presentation of quantitative data, we recommend that quantitative data be presented in a more easily accessible form to facilitate use in a qAOP. Additionally, we would also like to emphasize the importance of quality data reporting. Data that is not produced under OECD guidelines still need to follow a standard to be considered reliable for regulatory applications. Hartung et al. (2019) provides the reader with existing reporting guidelines and discusses the need for and what constitutes Good In Vitro Reporting Standards (GIVReSt). The majority of quantitative data in KER descriptions are

reported as in-text citations that requires a modeler to manually extract the data for qAOP development. This process could be shortened if the data were presented in a tabular form that combines data and quantitative relationships extracted from the cited sources. Factors that aide in this process include incorporating relevant figures from the cited studies with appropriate copyright permissions, tabulated data, and dose-response or response-response quantitative relationships. In the AOP Wiki, AOP 3 (Bal-Price et al., 2019) demonstrates these factors, as the KER description's quantitative evidence section contains significant and detailed information. The individual KERs contain relevant figures and tabulated information of the studies supporting the AOP. Presentation of information in this manner required a significant amount of effort by the AOP authors, which will ultimately improve the rate at which an AOP can be converted to a qAOP.

Concerning the biological differences between species, we would like to highlight the need to understand the physiology of the organism to be used in modeling, and more specifically to know which chemical stressors can be used if multiple species are involved in model development. Using AOP 3 as an example, 1-Methyl-4-phenyl-1,2,3,6-tetrahydropyridine (MPTP) is a compound commonly used in animal models of Parkinson's disease. More specifically, the AOP 3 authors mention that the effect on mice produces parkinsonian symptoms similar to that seen in humans, however rats are much less susceptible to MPTP, which would not be a good fit for a model (Bal-Price et al., 2019; Petroske et al., 2001). Understanding differences such as these are crucial to successful qAOP development. With the ultimate goal of 21st century toxicology moving away from in-vivo testing, greater emphasis should be placed on developing in vitro assays to be used as a replacement for animal studies (US EPA, 2021). In this case, research funding for the development of these assays and qAOPs would facilitate a move away from animal models by providing additional data sets for qAOP model development.

In the context of our case study, we would like to make recommendations for two of the challenges presented involving studies that measure multiple non-adjacent key events and model transferability. Currently, existing studies that measure non-adjacent key events are less ideal for

modeling and better suited for evaluation. This highlights the need for studies that measure multiple adjacent key events. There exists a similar need for models following a biologically based approach or AOPs that contain feedback loops. Biologically based models benefit most from having both dose-response and time series data of multiple key events, and studies that can provide that set of data would be invaluable to qAOP model developers and would aide in the transition from AOP to qAOP. Lastly, in a recommendation aimed toward model developers, we suggest keeping model transferability in mind when developing a model, as this would simplify the process for both developers and data scientists looking to adapt available models for their needs. Hosting models in repositories such as Github or SourceForge enables version tracking and would benefit model development by allowing multiple authors to modify existing models to meet new needs. Additionally, during the construction of either a qualitative or qAOP, the authors may come across raw data or models that could support qAOP development. In this case, we suggest hosting additional materials in the AOP Wiki to allow for better data management and efficient model development. To that end, we would also like to recommend development of modular qAOP models for KERs that can be shared and re-used to fit a developer's needs. Hosting of such models could take place in already existing repositories, such as BioModels (Malik-Sheriff et al., 2019).

In addition to their application in toxicity testing, AOPs and qAOPs have benefits beyond their original purpose. The design structure of AOPs can be helpful in other fields not associated with chemical risk assessment. The pharmacological and medical field could adapt the concept of AOPs to fit their needs. For example, recent efforts have begun in developing AOPs for COVID-19, known as the CIAO project[3]. Physicians could follow a similar modular approach in diagnosing and treating patients based on symptoms and treatment options. Additionally, AOPs can help identify knowledge gaps in a particular area (Leist et al., 2017). As AOPs are constructed from sources of published literature or sets of experimental data, their modular nature

[3] https://www.ciao-covid.net/

can easily highlight areas lacking in mechanistic understanding. Identification of these gaps will guide future studies and allow for a deeper understanding of the pathology in question (US EPA, 2020). Lastly, as progress continues in the development of AOPs and the addition of more qAOPs, the next logical step would be the integration of multiple qAOPs into qAOP networks. This might best be achieved with a Bayesian Network approach, as the structure of the AOPs and KEs naturally follow the form of the network (Perkins, Ashauer, et al., 2019). In conclusion, one may ask what specifically is needed to make these recommendations happen. Additional funding in the areas lacking in data suitable for model development would be a first major step, followed by a change in the culture of data sharing for better accessibility, and lastly, a change in best practices for how we write KE and KER descriptions. These changes will allow these recommendations to come to fruition and will facilitate the transition from AOP to qAOP.

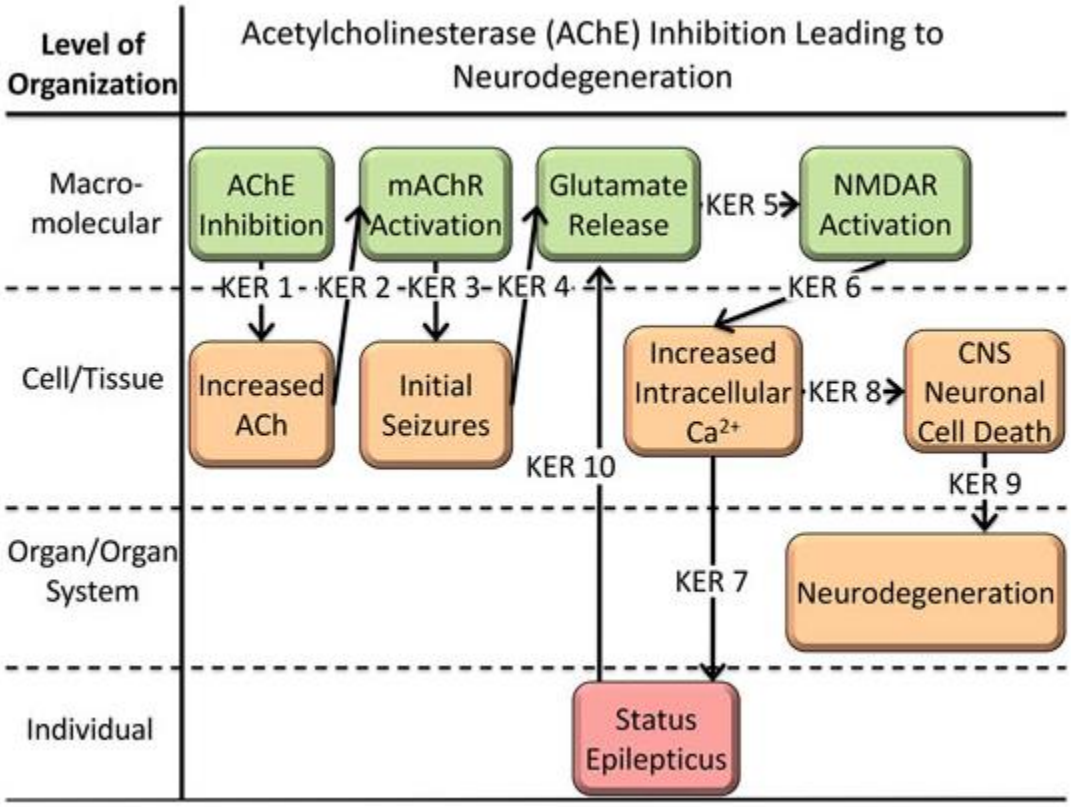

Figure 3.1. Graphical Representation of AOP 281: AChE Inhibition Leading to Neurodegeneration (Conrow et al., 2021). Each arrow represents the key event relationship (KER) between key events (KE) of the AOP.

Table 3.1. Categorization of AOPs with OECD Status based on presentation of quantitative data in the quantitative understanding section of the KER description. Total KERs include KERs between non-adjacent KEs. T = Written in text only with cited references, F = Includes figures extracted from articles, Ta = References are provided in a tabulated form. QU-WoE = Weight of Evidence under the quantitative understanding section.

AOP #	Title	QU-WoE for KERs in the AOP			Category
		Low	Moderate	High	
3	Inhibition of the mitochondrial complex I of nigro-striatal neurons leads to parkinsonian motor deficits	3	4	1	T, F, Ta
25	Aromatase inhibition leading to reproductive dysfunction	1	7	0	T
131	Aryl hydrocarbon receptor activation leading to uroporphyria	2	1	2	T, F
54	Inhibition of Na+/I- symporter (NIS) leads to learning and memory impairment	10	3	2	T
23	Androgen receptor agonism leading to reproductive dysfunction (in repeat-spawning fish)	8	5	0	T
21	Aryl hydrocarbon receptor activation leading to early life stage mortality, via increased COX-2	1	4	0	T
150	Aryl hydrocarbon receptor activation leading to early life stage mortality, via reduced VEGF	4	3	0	T
42	Inhibition of Thyroperoxidase and Subsequent Adverse Neurodevelopmental Outcomes in Mammals	7	5	0	T
10	Binding to the picrotoxin site of ionotropic GABA receptors leading to epileptic seizures in adult brain	0	3	2	T
6	Antagonist binding to PPARα leading to body-weight loss	2	4	2	T

REFERENCES

Ankley, G. T., Bennett, R. S., Erickson, R. J., Hoff, D. J., Hornung, M. W., Johnson, R. D., Mount, D. R., Nichols, J. W., Russom, C. L., Schmieder, P. K., Serrrano, J. A., Tietge, J. E., & Villeneuve, D. L. (2010). Adverse outcome pathways: A conceptual framework to support ecotoxicology research and risk assessment. *Environmental Toxicology and Chemistry*, *29*(3), 730-741. http://www.scopus.com/inward/record.url?eid=2-s2.0-77951118386&partnerID=40&md5=23562dfebf529c55ad1502553693629d

Bal-Price, A., M., L., S., S., F., T.-M., A., P., & A., T. (2019). *Inhibition of the mitochondrial complex I of nigro-striatal neurons leads to parkinsonian motor deficits*. AOP-Wiki. Retrieved November 18 from https://aopwiki.org/aops/3

Barhoumi, R., Qian, Y., Burghardt, R. C., & Tiffany-Castiglioni, E. (2010). Image analysis of Ca2+ signals as a basis for neurotoxicity assays: Promises and challenges [Article]. *Neurotoxicology and Teratology*, *32*(1), 16-24. https://doi.org/10.1016/j.ntt.2009.06.002

Becker, R. A., Ankley, G. T., Edwards, S. W., Kennedy, S. W., Linkov, I., Meek, B., Sachana, M., Segner, H., Van Der Burg, B., Villeneuve, D. L., Watanabe, H., & Barton-Maclaren, T. S. (2015). Increasing scientific confidence in adverse outcome pathways: Application of tailored Bradford-Hill considerations for evaluating weight of evidence. *Regul Toxicol Pharmacol*, *72*(3), 514-537. https://doi.org/10.1016/j.yrtph.2015.04.004

Bernillon, P., & Bois, F. Y. (2000). Statistical issues in toxicokinetic modeling: a bayesian perspective. *Environmental Health Perspectives*, *108*(Supplement 5), 883-893.

Berridge, M. J. (2012). Calcium signalling remodelling and disease. *Biochem Soc Trans*, *40*(2), 297-309. https://doi.org/10.1042/bst20110766

Borris, D. J., Bertram, E. H., & Kapur, J. (2000). Ketamine controls prolonged status epilepticus. *Epilepsy Res*, *42*(2-3), 117-122. https://doi.org/10.1016/s0920-1211(00)00175-3

Braitman, D. J., & Sparenborg, S. (1989). MK-801 protects against seizures induced by the cholinesterase inhibitor soman [Article]. *Brain Research Bulletin*, *23*(1-2), 145-148. https://doi.org/10.1016/0361-9230(89)90173-1

Brette, R., & Gerstner, W. (2005). Adaptive exponential integrate-and-fire model as an effective description of neuronal activity. *J Neurophysiol*, *94*(5), 3637-3642. https://doi.org/10.1152/jn.00686.2005

Burgoon, L. D., Angrish, M., Garcia-Reyero, N., Pollesch, N., Zupanic, A., & Perkins, E. (2020). Predicting the Probability that a Chemical Causes Steatosis Using Adverse Outcome Pathway Bayesian Networks (AOPBNs). *Risk Anal*, *40*(3), 512-523. https://doi.org/10.1111/risa.13423

Burkitt, A. N. (2006). A review of the integrate-and-fire neuron model: I. Homogeneous synaptic input. *Biol Cybern*, *95*(1), 1-19. https://doi.org/10.1007/s00422-006-0068-6

Case, R. M., Eisner, D., Gurney, A., Jones, O., Muallem, S., & Verkhratsky, A. (2007). Evolution of calcium homeostasis: from birth of the first cell to an omnipresent signalling system. *Cell Calcium*, *42*(4-5), 345-350. https://doi.org/10.1016/j.ceca.2007.05.001

Celander, M. C., Goldstone, J. V., Denslow, N. D., Iguchi, T., Kille, P., Meyerhoff, R. D., Smith, B. A., Hutchinson, T. H., & Wheeler, J. R. (2011). Species extrapolation for the 21st century. *Environmental Toxicology and Chemistry*, *30*(1), 52-63. http://www.scopus.com/inward/record.url?eid=2-s2.0-78650475538&partnerID=40&md5=7d5bdf790de858d40a2b7a13b8567702 https://setac.onlinelibrary.wiley.com/doi/10.1002/etc.382

Chefer, V. I., Thompson, A. C., Zapata, A., & Shippenberg, T. S. (2009). Overview of brain microdialysis. *Curr Protoc Neurosci*, *Chapter 7*, Unit7.1. https://doi.org/10.1002/0471142301.ns0701s47

Chen, K., & Seng, K. Y. (2012). Calibration and validation of a physiologically based model for soman intoxication in the rat, marmoset, guinea pig and pig. *J Appl Toxicol*, *32*(9), 673-686. https://doi.org/10.1002/jat.1671

Choi, D. W. (1988). Calcium-mediated neurotoxicity: relationship to specific channel types and role in ischemic damage. *Trends Neurosci*, *11*(10), 465-469. https://doi.org/10.1016/0166-2236(88)90200-7

Choy, M., Cheung, K. K., Thomas, D. L., Gadian, D. G., Lythgoe, M. F., & Scott, R. C. (2010). Quantitative MRI predicts status epilepticus-induced hippocampal injury in the lithium–pilocarpine rat model. *Epilepsy Research*, *88*(2), 221-230. https://doi.org/https://doi.org/10.1016/j.eplepsyres.2009.11.013

Clements, J. D., Lester, R. A., Tong, G., Jahr, C. E., & Westbrook, G. L. (1992). The time course of glutamate in the synaptic cleft. *Science*, *258*(5087), 1498-1501. https://doi.org/10.1126/science.1359647

Čolović, M. B., Krstić, D. Z., Lazarević-Pašti, T. D., Bondžić, A. M., & Vasić, V. M. (2013). Acetylcholinesterase inhibitors: Pharmacology and toxicology [Review]. *Current Neuropharmacology*, *11*(3), 315-335. https://doi.org/10.2174/1570159X11311030006

Conolly, R. B., Ankley, G. T., Cheng, W., Mayo, M. L., Miller, D. H., Perkins, E. J., Villeneuve, D. L., & Watanabe, K. H. (2017). Quantitative Adverse Outcome Pathways and Their Application to Predictive Toxicology. *Environ Sci Technol*, *51*(8), 4661-4672. https://doi.org/10.1021/acs.est.6b06230

Conrow, K., Ralduá, D., Garcia- Reyero, N., & Watanabe, K. H. (2019). *Using the AOP Wiki for the Development of an Acetylcholinesterase Inhibition Adverse Outcome Pathway* SETAC,

Conrow, K., Ralduá, D., Garcia- Reyero, N., & Watanabe, K. H. (2020). *An Adverse Outcome Pathway of Acetylcholinesterase Inhibition Leading to Neurodegeneration for Chemical Toxicity Assessment* SETAC,

Conrow, K., Sinitsyn, D., Ralduá, D., Garcia-Reyero, N., & Watanabe, K. H. (2021). *Acetylcholinesterase Inhibition Leading to Neurodegeneration*. Retrieved December 17 from https://aopwiki.org/aopwiki/snapshot/html_file/281-2021-12-17T23:09:50+00:00.html

Conrow, K., Sinitsyn, D., Ralduá, D., Garcia-Reyero, N., & Watanabe, K. H. (2022). *Acetylcholinesterase Inhibition Leading to Neurodegeneration*. Retrieved October 12 from https://aopwiki.org/aops/281

Cruickshank, J. W., Brudzynski, S. M., & McLachlan, R. S. (1994). Involvement of M1 muscarinic receptors in the initiation of cholinergically induced epileptic seizures in the rat brain [Article]. *Brain Research*, *643*(1-2), 125-129. https://doi.org/10.1016/0006-8993(94)90017-5

Das, A., Dikshit, M., & Nath, C. (2001). Profile of acetylcholinesterase in brain areas of male and female rats of adult and old age. *Life Sci*, *68*(13), 1545-1555. https://doi.org/10.1016/s0024-3205(01)00950-x

Dasari, S., & Gulledge, A. T. (2011). M1 and M4 receptors modulate hippocampal pyramidal neurons. *J Neurophysiol*, *105*(2), 779-792. https://doi.org/10.1152/jn.00686.2010

Davidson, I. W. F., Parker, J. C., & Beliles, R. P. (1986). Biological basis for extrapolation across mammalian species. *Regulatory Toxicology and Pharmacology*, *6*, 211-237.

Deshpande, L. S., Carter, D. S., Blair, R. E., & DeLorenzo, R. J. (2010). Development of a prolonged calcium plateau in hippocampal neurons in rats surviving status epilepticus induced by the organophosphate diisopropylfluorophosphate. *Toxicol Sci*, *116*(2), 623-631. https://doi.org/10.1093/toxsci/kfq157

Deshpande, L. S., Carter, D. S., Phillips, K. F., Blair, R. E., & DeLorenzo, R. J. (2014). Development of status epilepticus, sustained calcium elevations and neuronal injury in a rat survival model of lethal paraoxon intoxication [Article]. *NeuroToxicology*, *44*, 17-26. https://doi.org/10.1016/j.neuro.2014.04.006

Deshpande, L. S., Lou, J. K., Mian, A., Blair, R. E., Sombati, S., Attkisson, E., & DeLorenzo, R. J. (2008). Time course and mechanism of hippocampal neuronal death in an in vitro model of status epilepticus: role of NMDA receptor activation and NMDA dependent calcium entry. *Eur J Pharmacol*, *583*(1), 73-83. https://doi.org/10.1016/j.ejphar.2008.01.025

Deshpande, L. S., Lou, J. K., Mian, A., Blair, R. E., Sombati, S., & DeLorenzo, R. J. (2007). In vitro status epilepticus but not spontaneous recurrent seizures cause cell death in cultured hippocampal neurons. *Epilepsy Res*, *75*(2-3), 171-179. https://doi.org/10.1016/j.eplepsyres.2007.05.011

Destexhe, A., Mainen, Z. F., & Sejnowski, T. J. (1994a). An Efficient Method for Computing Synaptic Conductances Based on a Kinetic Model of Receptor Binding. *Neural Computation*, *6*(1), 14-18. https://doi.org/10.1162/neco.1994.6.1.14

Destexhe, A., Mainen, Z. F., & Sejnowski, T. J. (1994b). Synthesis of models for excitable membranes, synaptic transmission and neuromodulation using a common kinetic formalism. *J Comput Neurosci*, *1*(3), 195-230. https://doi.org/10.1007/bf00961734

Doering, J. A., Villeneuve, D. L., Poole, S. T., Blackwell, B. R., Jensen, K. M., Kahl, M. D., Kittelson, A. R., Feifarek, D. J., Tilton, C. B., LaLone, C. A., & Ankley, G. T. (2019). Quantitative Response-Response Relationships Linking Aromatase Inhibition to Decreased Fecundity are Conserved Across Three Fishes with Asynchronous Oocyte Development. *Environ Sci Technol*, *53*(17), 10470-10478. https://doi.org/10.1021/acs.est.9b02606

Doering, J. A., Wiseman, S., Giesy, J. P., & Hecker, M. (2018). A Cross-species Quantitative Adverse Outcome Pathway for Activation of the Aryl Hydrocarbon Receptor Leading to Early Life Stage Mortality in Birds and Fishes. *Environ Sci Technol*, *52*(13), 7524-7533. https://doi.org/10.1021/acs.est.8b01438

Falkenburger, B. H., Jensen, J. B., & Hille, B. (2010). Kinetics of M1 muscarinic receptor and G protein signaling to phospholipase C in living cells. *The Journal of General Physiology*, *135*(2), 81-97. https://doi.org/10.1085/jgp.200910344

Farhat, A., Manning, G., OBrien, J., & Kennedy, S. W. (2021). *Aryl hydrocarbon receptor activation leading to uroporphyria*. AOP-Wiki. Retrieved November 18 from https://aopwiki.org/aops/131

Foran, C. M., Rycroft, T., Keisler, J., Perkins, E. J., Linkov, I., & Garcia-Reyero, N. (2019). A modular approach for assembly of quantitative adverse outcome pathways. *Altex*, *36*(3), 353-362. https://doi.org/10.14573/altex.1810181

Fosbraey, P., Wetherell, J. R., & French, M. C. (1990). Neurotransmitter changes in guinea-pig brain regions following soman intoxication. *J Neurochem*, *54*(1), 72-79. https://doi.org/10.1111/j.1471-4159.1990.tb13284.x

Fukuto, T. R. (1990). Mechanism of action of organophosphorus and carbamate insecticides. *Environ Health Perspect*, *87*, 245-254. https://doi.org/10.1289/ehp.9087245

Gelman, A., Bois, F., & Jiang, J. (1996). Physiological pharmacokinetic analysis using population modeling and informative prior distributions. *Journal of the American Statistical Association*, *91*(436), 1400-1412.

Gillies, K., Krone, S., Nagler, J. J., & Schultz, I. R. (2016). A computational model of the rainbow trout hypothalamus-pituitary-ovary-liver axis. *PLoS Computational Biology*, *12*(4), Article e1004874. https://doi.org/10.1371/journal.pcbi.1004874

Greget, R., Dadak, S., Barbier, L., Lauga, F., Linossier-Pierre, S., Pernot, F., Legendre, A., Ambert, N., Bouteiller, J. M., Dorandeu, F., Bischoff, S., Baudry, M., Fagni, L., & Moussaoui, S. (2016). Modeling and simulation of organophosphate-induced neurotoxicity: Prediction and validation by experimental studies [Article]. *NeuroToxicology*, *54*, 140-152. https://doi.org/10.1016/j.neuro.2016.04.013

Haga, T. (2013). Molecular properties of muscarinic acetylcholine receptors [Review]. *Proceedings of the Japan Academy Series B: Physical and Biological Sciences*, *89*(6), 226-256. https://doi.org/10.2183/pjab.89.226

Hamby, D. M. (1994). A review of techniques for parameter sensitivity analysis of environmental models. *Environ Monit Assess*, *32*(2), 135-154. https://doi.org/10.1007/bf00547132

Hamilton, S. E., Loose, M. D., Qi, M., Levey, A. I., Hille, B., McKnight, G. S., Idzerda, R. L., & Nathanson, N. M. (1997). Disruption of the m1 receptor gene ablates muscarinic receptor-dependent M current regulation and seizure activity in mice. *Proceedings of the National Academy of Sciences*, *94*(24), 13311-13316. https://doi.org/10.1073/pnas.94.24.13311

Harris, K. D., Hirase, H., Leinekugel, X., Henze, D. A., & Buzsáki, G. (2001). Temporal interaction between single spikes and complex spike bursts in hippocampal pyramidal cells. *Neuron*, *32*(1), 141-149. https://doi.org/10.1016/s0896-6273(01)00447-0

Hartley, D. M., Kurth, M. C., Bjerkness, L., Weiss, J. H., & Choi, D. W. (1993). Glutamate receptor-induced 45Ca2+ accumulation in cortical cell culture correlates with subsequent neuronal degeneration. *J Neurosci*, *13*(5), 1993-2000. https://doi.org/10.1523/jneurosci.13-05-01993.1993

Hartung, T., De Vries, R., Hoffmann, S., Hogberg, H. T., Smirnova, L., Tsaioun, K., Whaley, P., & Leist, M. (2019). Toward Good In Vitro Reporting Standards. *Altex*, *36*(1), 3-17. https://doi.org/10.14573/altex.1812191

Hecker, M. (2018). Non-model species in ecological risk assessment. In *A Systems Biology Approach to Advancing Adverse Outcome Pathways for Risk Assessment* (pp. 107-132). https://doi.org/10.1007/978-3-319-66084-4_6

Hodgkin, A. L., & Huxley, A. F. (1952). A quantitative description of membrane current and its application to conduction and excitation in nerve. *J Physiol*, *117*(4), 500-544. https://doi.org/10.1113/jphysiol.1952.sp004764

Hu, E., Mergenthal, A., Bingham, C. S., Song, D., Bouteiller, J. M., & Berger, T. W. (2018). A Glutamatergic Spine Model to Enable Multi-Scale Modeling of Nonlinear Calcium Dynamics. *Front Comput Neurosci*, *12*, 58. https://doi.org/10.3389/fncom.2018.00058

Hübel, N., Hosseini-Zare, M. S., Žiburkus, J., & Ullah, G. (2017). The role of glutamate in neuronal ion homeostasis: A case study of spreading depolarization. *PLoS Comput Biol*, *13*(10), e1005804. https://doi.org/10.1371/journal.pcbi.1005804

Hucka, M., Finney, A., Sauro, H. M., Bolouri, H., Doyle, J. C., Kitano, H., Arkin, A. P., Bornstein, B. J., Bray, D., Cornish-Bowden, A., Cuellar, A. A., Dronov, S., Gilles, E. D., Ginkel, M., Gor, V., Goryanin, I. I., Hedley, W. J., Hodgman, T. C., Hofmeyr, J. H., . . . Wang, J. (2003). The systems biology markup language (SBML): A medium for representation and exchange of biochemical network models [Article]. *Bioinformatics*, *19*(4), 524-531. https://doi.org/10.1093/bioinformatics/btg015

Hulme, E. C., Birdsall, N. J., & Buckley, N. J. (1990). Muscarinic receptor subtypes. *Annu Rev Pharmacol Toxicol*, *30*, 633-673. https://doi.org/10.1146/annurev.pa.30.040190.003221

Jager, T. (2021). Robust Likelihood-Based Approach for Automated Optimization and Uncertainty Analysis of Toxicokinetic-Toxicodynamic Models [Article]. *Integrated Environmental Assessment and Management*, *17*(2), 388-397. https://doi.org/10.1002/ieam.4333

Jeong, J., Song, T., Chatterjee, N., Choi, I., Cha, Y. K., & Choi, J. (2018). Developing adverse outcome pathways on silver nanoparticle-induced reproductive toxicity via oxidative stress in the nematode Caenorhabditis elegans using a Bayesian network model [Article]. *Nanotoxicology*, *12*(10), 1182-1197. https://doi.org/10.1080/17435390.2018.1529835

Kandel, E., Schwartz, J., Jessell, T., Siegelbaum, S., & Hudspeth, A. J. (2013a). Seizures and Epilepsy. In *Principles of Neural Science, Fifth Edition* (pp. 1116-1139). McGraw-Hill Publishing. http://ebookcentral.proquest.com/lib/asulib-ebooks/detail.action?docID=4959346

Kandel, E., Schwartz, J., Jessell, T., Siegelbaum, S., & Hudspeth, A. J. (2013b). Synaptic Integration in the Central Nervous System. In *Principles of Neural Science, Fifth Edition* (pp. 210-235). McGraw-Hill Publishing. http://ebookcentral.proquest.com/lib/asulib-ebooks/detail.action?docID=4959346

Kapur, J. (2018). Role of NMDA receptors in the pathophysiology and treatment of status epilepticus. *Epilepsia Open*, *3*(Suppl Suppl 2), 165-168. https://doi.org/10.1002/epi4.12270

Kassa, J., & Bajgar, J. (1998). Changes of acetylcholinesterase activity in various parts of brain following nontreated and treated soman poisoning in rats. *Mol Chem Neuropathol*, *33*(3), 175-184. https://doi.org/10.1007/bf02815180

Kellar, K. J., Martino, A. M., Hall, D. P., Jr., Schwartz, R. D., & Taylor, R. L. (1985). High-affinity binding of [3H]acetylcholine to muscarinic cholinergic receptors. *J Neurosci*, *5*(6), 1577-1582. https://doi.org/10.1523/jneurosci.05-06-01577.1985

Kim, Y. K., Koo, B. S., Gong, D. J., Lee, Y. C., Ko, J. H., & Kim, C. H. (2003). Comparative effect of Prunus persica L. BATSCH-water extract and tacrine (9-amino-1,2,3,4-tetrahydroacridine hydrochloride) on concentration of extracellular acetylcholine in the rat hippocampus. *J Ethnopharmacol*, *87*(2-3), 149-154. https://doi.org/10.1016/s0378-8741(03)00106-5

Kosasa, T., Kuriya, Y., Matsui, K., & Yamanishi, Y. (1999). Effect of donepezil hydrochloride (E2020) on basal concentration of extracellular acetylcholine in the hippocampus of rats [Article]. *European Journal of Pharmacology*, *380*(2-3), 101-107. https://doi.org/10.1016/S0014-2999(99)00545-2

Kroemer, G., Galluzzi, L., Vandenabeele, P., Abrams, J., Alnemri, E. S., Baehrecke, E. H., Blagosklonny, M. V., El-Deiry, W. S., Golstein, P., Green, D. R., Hengartner, M., Knight, R. A., Kumar, S., Lipton, S. A., Malorni, W., Nuñez, G., Peter, M. E., Tschopp, J., Yuan, J., . . . Melino, G. (2009). Classification of cell death: recommendations of the Nomenclature Committee on Cell Death 2009. *Cell Death Differ*, *16*(1), 3-11. https://doi.org/10.1038/cdd.2008.150

Lallement, G., Carpentier, P., Collet, A., Pernot-Marino, I., Baubichon, D., & Blanchet, G. (1991). Effects of soman-induced seizures on different extracellular amino acid levels and on glutamate uptake in rat hippocampus [Article]. *Brain Research*, *563*(1-2), 234-240. https://doi.org/10.1016/0006-8993(91)91539-D

Lallement, G., Clarencon, D., Galonnier, M., Baubichon, D., Burckhart, M. F., & Peoc'h, M. (1999). Acute soman poisoning in primates neither pretreated nor receiving immediate therapy: value of gacyclidine (GK-11) in delayed medical support. *Arch Toxicol*, *73*(2), 115-122. https://doi.org/10.1007/s002040050595

Lallement, G., Denoyer, M., Collet, A., Pernot-Marino, I., Baubichon, D., Monmaur, P., & Blanchet, G. (1992). Changes in hippocampal acetylcholine and glutamate extracellular levels during soman-induced seizures: Influence of septal cholinoceptive cells [Article]. *Neuroscience Letters*, *139*(1), 104-107. https://doi.org/10.1016/0304-3940(92)90868-8

Langenberg, J. P., van Dijk, C., Sweeney, R. E., Maxwell, D. M., De Jong, L. P., & Benschop, H. P. (1997). Development of a physiologically based model for the toxicokinetics of C(+/-)P(+/-)-soman in the atropinized guinea pig. *Arch Toxicol*, *71*(5), 320-331. https://doi.org/10.1007/s002040050393

Leist, M., Ghallab, A., Graepel, R., Marchan, R., Hassan, R., Bennekou, S. H., Limonciel, A., Vinken, M., Schildknecht, S., Waldmann, T., Danen, E., van Ravenzwaay, B., Kamp, H., Gardner, I., Godoy, P., Bois, F. Y., Braeuning, A., Reif, R., Oesch, F., . . . Hengstler, J. G. (2017). Adverse outcome pathways: opportunities, limitations and open questions. *Arch Toxicol*, *91*(11), 3477-3505. https://doi.org/10.1007/s00204-017-2045-3

Liu, F., Patterson, T. A., Sadovova, N., Zhang, X., Liu, S., Zou, X., Hanig, J. P., Paule, M. G., Slikker, W., Jr., & Wang, C. (2013). Ketamine-induced neuronal damage and altered N-methyl-D-aspartate receptor function in rat primary forebrain culture. *Toxicol Sci*, *131*(2), 548-557. https://doi.org/10.1093/toxsci/kfs296

Lowenstein, D. H., & Alldredge, B. K. (1998). Status Epilepticus. *New England Journal of Medicine*, *338*(14), 970-976. https://doi.org/10.1056/nejm199804023381407

Lu, J., Wu, D. M., Zheng, Y. L., Hu, B., Cheng, W., & Zhang, Z. F. (2012). Purple sweet potato color attenuates domoic acid-induced cognitive deficits by promoting estrogen receptor-α-mediated mitochondrial biogenesis signaling in mice. *Free Radic Biol Med*, *52*(3), 646-659. https://doi.org/10.1016/j.freeradbiomed.2011.11.016

Malik-Sheriff, R. S., Glont, M., Nguyen, T. V. N., Tiwari, K., Roberts, M. G., Xavier, A., Vu, M. T., Men, J., Maire, M., Kananathan, S., Fairbanks, E. L., Meyer, J. P., Arankalle, C., Varusai, T. M., Knight-Schrijver, V., Li, L., Dueñas-Roca, C., Dass, G., Keating, S. M., . . . Hermjakob, H. (2019). BioModels—15 years of sharing computational models in life science. *Nucleic Acids Research*, *48*(D1), D407-D415. https://doi.org/10.1093/nar/gkz1055

Marks, J. D., Friedman, J. E., & Haddad, G. G. (1996). Vulnerability of CA1 neurons to glutamate is developmentally regulated. *Brain Res Dev Brain Res*, *97*(2), 194-206. https://pdf.sciencedirectassets.com/271045/1-s2.0-S0165380600X0020X/1-s2.0-S0165380696001496/main.pdf?X-Amz-Security-Token=AgoJb3JpZ2luX2VjEP7%2F%2F%2F%2F%2F%2F%2F%2F%2F%2FwEaCXVzLWVhc3QtMSJHMEUCIQCk2HmKS8iOaOFwbQkTYV%2FOOArdlqmZ%2FwageWQgSia40QIgYTCTfZWV7sa%2BRSSsNl3A3Hh9WyqZtz1PEV7%2BxXbloxMq4wMIl%2F%2F%2F%2F%2F%2F%2F%2F%2F%2F%2FARACGgwwNTkwMDM1NDY4NjUiDA4cQFOOngbkf7fbdyq3AwVmWTMfLue1axaBqHN312AE0j25%2FoOA4U4oHjKiwkVRpq4VFKhvzzljFNAUcGcMnCWt3kgun8hYioj4ACQqNdNIZdpuMESKkHpwJbAXIYz5vKCnERJTBqr8yaLjZmjcjJ3WBqB3r%2F%2B8oYbu0GmiIQO5XpzPaJgVqAQ%2FblEYUW4VX%2FfQPTEsj%2FoTmO%2B9OXE1R%2BdDGviIwRsAdCtgj%2BrhRhgBHRkTZNkBP0PrhqbcedXI%2FwSNqA5F84Jtka7n6zpgxXz4U2q%2F5Us8lxI2gerx4a0zGIFvmcuw6Oe41s4BfMwuKGWHdClYdJLAqgOw%2Bjy9yBjx%2F8o8hK9a0u%2BUBlfWTVV%2FmOC14ch0VH9JZ8esBZF3ZCid0X8y1dEe7ljy9gs0iAJPpYEQeuIAak0J%2B2JpmUxMhaRXGzVRR87bd4f8IAQJl%2B6Ek8kavKlmBJWzOKChJi7KITnsu9hGxaVsJ9%2BFbNZm1Mqeb2y0sTvT1orFf%2Bcb3wdribEXZYIPFwNnMROSDSw4mtMwOLf671THXuEb6hr2JrQUELUwDWXRwGN4fRrTgXPkREBXTErOyQK%2BzcnmJN112YJ%2FOJMwqa7s6gU6tAF6R0H8Ld%2FZtjpC3rjMLEn6BXnqDUdgXxiyyFSW9ZBscMbhsslAYM77zioX0kObyac68mbkEWpVO1aM%2Fa6dBfVtGGTAdlqC%2BMVxqaUE2KsxbiY1sNRoJV5ZtRAYVpvnRpYOPjN7ICNYcPa%2Fc5aki8WPqqBEE%2Bf40jEOavYKfaeBSa7AFKQIC4PIpcs8Sn7eFawmGCAEzuVyaM%2Flp3diyqaR6xyJvCuwoqdC%2BKmgvd2zpHj89l0%3D&X-Amz-Algorithm=AWS4-HMAC-SHA256&X-Amz-Date=20190819T223422Z&X-Amz-SignedHeaders=host&X-Amz-Expires=300&X-Amz-Credential=ASIAQ3PHCVTY446QTT6Q%2F20190819%2Fus-east-1%2Fs3%2Faws4_request&X-Amz-Signature=77393c6f0e6eac1970ad731b7a4ffcf6ae6757ab1102ec8ac459a15c2db46689&hash=05cdd681d82b31361a811c86e841bbe527570b4296be6fcec00df29409c17c2b&h

ost=68042c943591013ac2b2430a89b270f6af2c76d8dfd086a07176afe7c76c2c61&pii=S0165380696001496&tid=spdf-89fd21f8-8fc7-433c-8aec-94fba1bf871a&sid=6842a29a6c4454437b9baa20101520ee3b8bgxrqa&type=client

Marrion, N. V. (1997). Control of M-current. *Annu Rev Physiol*, *59*, 483-504. https://doi.org/10.1146/annurev.physiol.59.1.483

Matlab, S. (2012). Matlab. *The MathWorks, Natick, MA*.

Maxwell, D. M., Vlahacos, C. P., & Lenz, D. E. (1988). A pharmacodynamic model for soman in the rat. *Toxicol Lett*, *43*(1-3), 175-188. https://doi.org/10.1016/0378-4274(88)90027-6

McDonough, J. H., Jr., & Shih, T. M. (1997). Neuropharmacological mechanisms of nerve agent-induced seizure and neuropathology. *Neurosci Biobehav Rev*, *21*(5), 559-579. https://doi.org/10.1016/s0149-7634(96)00050-4

McKinney, M., Coyle, J. T., & Hedreen, J. C. (1983). Topographic analysis of the innervation of the rat neocortex and hippocampus by the basal forebrain cholinergic system. *J Comp Neurol*, *217*(1), 103-121. https://doi.org/10.1002/cne.902170109

Mergenthal, A., Bouteiller, J.-M. C., Yu, G. J., & Berger, T. W. (2020). A Computational Model of the Cholinergic Modulation of CA1 Pyramidal Cell Activity [Original Research]. *Frontiers in Computational Neuroscience*, *14*(75). https://doi.org/10.3389/fncom.2020.00075

Merricks, E. M., Smith, E. H., Emerson, R. G., Bateman, L. M., McKhann, G. M., Goodman, R. R., Sheth, S. A., Greger, B., House, P. A., Trevelyan, A. J., & Schevon, C. A. (2021). Neuronal Firing and Waveform Alterations through Ictal Recruitment in Humans. *J Neurosci*, *41*(4), 766-779. https://doi.org/10.1523/jneurosci.0417-20.2020

Meurs, A., Clinckers, R., Ebinger, G., Michotte, Y., & Smolders, I. (2008). Seizure activity and changes in hippocampal extracellular glutamate, GABA, dopamine and serotonin. *Epilepsy Res*, *78*(1), 50-59. https://doi.org/10.1016/j.eplepsyres.2007.10.007

Michaels, R. L., & Rothman, S. M. (1990). Glutamate neurotoxicity in vitro: antagonist pharmacology and intracellular calcium concentrations. *J Neurosci*, *10*(1), 283-292. https://doi.org/10.1523/jneurosci.10-01-00283.1990

Miller, S. L., Aroniadou-Anderjaska, V., Figueiredo, T. H., Prager, E. M., Almeida-Suhett, C. P., Apland, J. P., & Braga, M. F. M. (2015). A rat model of nerve agent exposure applicable to the pediatric population: The anticonvulsant efficacies of atropine and GluK1 antagonists [Article]. *Toxicology and Applied Pharmacology*, *284*(2), 204-216. https://doi.org/10.1016/j.taap.2015.02.008

Moe, S. J., Wolf, R., Xie, L., Landis, W. G., Kotamäki, N., & Tollefsen, K. E. (2021). Quantification of an Adverse Outcome Pathway Network by Bayesian Regression and Bayesian Network Modeling. *Integr Environ Assess Manag*, *17*(1), 147-164. https://doi.org/10.1002/ieam.4348

Muller, E. B., Lin, S., & Nisbet, R. M. (2015). Quantitative Adverse Outcome Pathway Analysis of Hatching in Zebrafish with CuO Nanoparticles. *Environ Sci Technol*, *49*(19), 11817-11824. https://doi.org/10.1021/acs.est.5b01837

Nagarkatti, N., Deshpande, L. S., Carter, D. S., & DeLorenzo, R. J. (2010). Dantrolene inhibits the calcium plateau and prevents the development of spontaneous recurrent epileptiform discharges following in vitro status epilepticus. *Eur J Neurosci*, *32*(1), 80-88. https://doi.org/10.1111/j.1460-9568.2010.07262.x

O'Donnell, J. C., McDonough, J. H., & Shih, T.-M. (2011). In vivo microdialysis and electroencephalographic activity in freely moving guinea pigs exposed to organophosphorus nerve agents sarin and VX: analysis of acetylcholine and glutamate. *Archives of Toxicology*, *85*(12), 1607-1616. https://doi.org/10.1007/s00204-011-0724-z

OECD. (2018). *Users' Handbook supplement to the Guidance Document for developing and assessing Adverse Outcome Pathways*. Retrieved December from https://www.oecd-ilibrary.org/content/paper/5jlv1m9d1g32-en

OECD. (2021). *Guidance Document for the Scientific Review of Adverse Outcome Pathways* (ENV/CBC/MONO(2021)22). (Series on Testing and Assessment, Issue. Inter-organization Programme for the Sound Management of Chemicals (IOMC). https://www.oecd.org/officialdocuments/publicdisplaydocumentpdf/?cote=ENV/CBC/MONO(2021)22&docLanguage=En

Otto, J. F., Yang, Y., Frankel, W. N., White, H. S., & Wilcox, K. S. (2006). A spontaneous mutation involving Kcnq2 (Kv7.2) reduces M-current density and spike frequency adaptation in mouse CA1 neurons. *J Neurosci*, *26*(7), 2053-2059. https://doi.org/10.1523/jneurosci.1575-05.2006

Paini, A., Campia, I., Cronin, M. T. D., Asturiol, D., Ceriani, L., Exner, T. E., Gao, W., Gomes, C., Kruisselbrink, J., Martens, M., Meek, M. E. B., Pamies, D., Pletz, J., Scholz, S., Schüttler, A., Spînu, N., Villeneuve, D. L., Wittwehr, C., Worth, A., & Luijten, M. (2021). Towards a qAOP framework for predictive toxicology - Linking data to decisions. *Computational Toxicology*, 100195. https://doi.org/https://doi.org/10.1016/j.comtox.2021.100195

Pal, S., Sombati, S., Limbrick, D. D., Jr., & DeLorenzo, R. J. (1999). In vitro status epilepticus causes sustained elevation of intracellular calcium levels in hippocampal neurons. *Brain Res*, *851*(1-2), 20-31. https://doi.org/10.1016/s0006-8993(99)02035-1

Pereira, E. F. R., Aracava, Y., DeTolla, L. J., Jr., Beecham, E. J., Basinger, G. W., Jr., Wakayama, E. J., & Albuquerque, E. X. (2014). Animal models that best reproduce the clinical manifestations of human intoxication with organophosphorus compounds. *The Journal of pharmacology and experimental therapeutics*, *350*(2), 313-321. https://doi.org/10.1124/jpet.114.214932

Perkins, E. J., Ashauer, R., Burgoon, L., Conolly, R., Landesmann, B., Mackay, C., Murphy, C. A., Pollesch, N., Wheeler, J. R., Zupanic, A., & Scholz, S. (2019). Building and Applying Quantitative Adverse Outcome Pathway Models for Chemical Hazard and Risk Assessment. *Environ Toxicol Chem*, *38*(9), 1850-1865. https://doi.org/10.1002/etc.4505

Perkins, E. J., Gayen, K., Shoemaker, J. E., Antczak, P., Burgoon, L., Falciani, F., Gutsell, S., Hodges, G., Kienzler, A., Knapen, D., McBride, M., Willett, C., Doyle, F. J., & Garcia-Reyero, N. (2019). Chemical hazard prediction and hypothesis testing using quantitative adverse outcome pathways. *Altex*, *36*(1), 91-102. https://doi.org/10.14573/altex.1808241

Petroske, E., Meredith, G. E., Callen, S., Totterdell, S., & Lau, Y. S. (2001). Mouse model of Parkinsonism: a comparison between subacute MPTP and chronic MPTP/probenecid treatment. *Neuroscience*, *106*(3), 589-601. https://doi.org/10.1016/s0306-4522(01)00295-0

Przedborski, S., Vila, M., & Jackson-Lewis, V. (2003). Neurodegeneration: what is it and where are we? *J Clin Invest*, *111*(1), 3-10. https://doi.org/10.1172/jci17522

Quirion, R., Richard, J., & Wilson, A. (1994). Muscarinic and nicotinic modulation of cortical acetylcholine release monitored by in vivo microdialysis in freely moving adult rats. *Synapse*, *17*(2), 92-100. https://doi.org/10.1002/syn.890170205

Raybaut, P. (2009). Spyder-documentation. *Available online at: pythonhosted. org*.

Raza, M., Blair, R. E., Sombati, S., Carter, D. S., Deshpande, L. S., & DeLorenzo, R. J. (2004). Evidence that injury-induced changes in hippocampal neuronal calcium dynamics during epileptogenesis cause acquired epilepsy. *Proc Natl Acad Sci U S A*, *101*(50), 17522-17527. https://doi.org/10.1073/pnas.0408155101

Reddy, D. S., Zaayman, M., Kuruba, R., & Wu, X. (2021). Comparative profile of refractory status epilepticus models following exposure of cholinergic agents pilocarpine, DFP, and soman. *Neuropharmacology*, *191*, 108571. https://doi.org/10.1016/j.neuropharm.2021.108571

Sabatini, B. L., Oertner, T. G., & Svoboda, K. (2002). The life cycle of Ca(2+) ions in dendritic spines. *Neuron*, *33*(3), 439-452. https://doi.org/10.1016/s0896-6273(02)00573-1

Sattler, R., & Tymianski, M. (2000). Molecular mechanisms of calcium-dependent excitotoxicity. *J Mol Med (Berl)*, *78*(1), 3-13. https://doi.org/10.1007/s001090000077

Schultz, I. R., & Watanabe, K. H. (2018). The Development of Quantitative AOPs. In N. Garcia-Reyero & C. A. Murphy (Eds.), *A Systems Biology Approach for Advancing Adverse Outcome Pathways for Risk Assessment* (pp. 263-280). Springer. https://doi.org/10.1007/978-3-319-66084-4_13

Sidell, F. R. (1994). Clinical effects of organophosphorus cholinesterase inhibitors. *J Appl Toxicol*, *14*(2), 111-113. https://doi.org/10.1002/jat.2550140212

Simon, A. P., Poindessous-Jazat, F., Dutar, P., Epelbaum, J., & Bassant, M. H. (2006). Firing properties of anatomically identified neurons in the medial septum of anesthetized and unanesthetized restrained rats. *J Neurosci*, *26*(35), 9038-9046. https://doi.org/10.1523/jneurosci.1401-06.2006

Sinitsyn, D., Garcia-Reyero, N., & Watanabe, K. H. (2022). From Qualitative to Quantitative AOP: A Case Study of Neurodegeneration. *Front Toxicol*, *4*, 838729. https://doi.org/10.3389/ftox.2022.838729

Society for Advancement of AOPs. (2022). AOP-Wiki. Retrieved October 31 from http://aopwiki.org

Song, Y., Xie, L., Lee, Y., & Tollefsen, K. E. (2020). De Novo Development of a Quantitative Adverse Outcome Pathway (qAOP) Network for Ultraviolet B (UVB) Radiation Using Targeted Laboratory Tests and Automated Data Mining. *Environ Sci Technol*, *54*(20), 13147-13156. https://doi.org/10.1021/acs.est.0c03794

Sparenborg, S., Brennecke, L. H., Jaax, N. K., & Braitman, D. J. (1992). Dizocilpine (MK-801) arrests status epilepticus and prevents brain damage induced by soman. *Neuropharmacology*, *31*(4), 357-368. https://doi.org/10.1016/0028-3908(92)90068-z

Spinu, N., Cronin, M. T. D., Enoch, S. J., Madden, J. C., & Worth, A. P. (2020). Quantitative adverse outcome pathway (qAOP) models for toxicity prediction. *Arch Toxicol*, *94*(5), 1497-1510. https://doi.org/10.1007/s00204-020-02774-7

Sweeney, R. E., Langenberg, J. P., & Maxwell, D. M. (2006). A physiologically based pharmacokinetic (PB/PK) model for multiple exposure routes of soman in multiple species. *Arch Toxicol*, *80*(11), 719-731. https://doi.org/10.1007/s00204-006-0114-0

The EndNote Team. (2013). *EndNote*. In (Version EndNote 20) [64 bit]. Clarivate.

Tonduli, L. S., Testylier, G., Marino, I. P., & Lallement, G. (1999). Triggering of soman-induced seizures in rats: multiparametric analysis with special correlation between enzymatic, neurochemical and electrophysiological data. *J Neurosci Res*, *58*(3), 464-473.

Uchida, S., Takeyasu, K., Ichida, S., & Yoshida, H. (1978). Muscarinic cholinergic receptors in mammalian brain: differences between bindings of acetylcholine and atropine. *Jpn J Pharmacol*, *28*(6), 853-862. https://doi.org/10.1254/jjp.28.853

US EPA. (2020). *New Approach Methods Work Plan: Reducing use of animals in chemical testing* (EPA 615B2001). U.S. Environmental Protection Agency.

US EPA. (2021). *New Approach Methods Work Plan (v2)* (EPA/600/X-21/209). U.S. Environmental Protection Agency.

Villeneuve, D. (2021). *Aromatase inhibition leading to reproductive dysfunction*. Retrieved November 18 from https://aopwiki.org/aops/25

Virtanen, P., Gommers, R., Oliphant, T. E., Haberland, M., Reddy, T., Cournapeau, D., Burovski, E., Peterson, P., Weckesser, W., & Bright, J. (2020). SciPy 1.0: fundamental algorithms for scientific computing in Python. *Nature methods*, *17*(3), 261-272.

Wiener, S. I., Paul, C. A., & Eichenbaum, H. (1989). Spatial and behavioral correlates of hippocampal neuronal activity. *J Neurosci*, *9*(8), 2737-2763. https://doi.org/10.1523/jneurosci.09-08-02737.1989

Yanagisawa, N., Morita, H., & Nakajima, T. (2006). Sarin experiences in Japan: acute toxicity and long-term effects. *J Neurol Sci*, *249*(1), 76-85. https://doi.org/10.1016/j.jns.2006.06.007

Zgheib, E., Gao, W., Limonciel, A., Aladjov, H., Yang, H., Tebby, C., Gayraud, G., Jennings, P., Sachana, M., Beltman, J. B., & Bois, F. Y. (2019). Application of three approaches for quantitative AOP development to renal toxicity [Article]. *Computational Toxicology*, *11*, 1-13. https://doi.org/10.1016/j.comtox.2019.02.001

Zhivotovsky, B., & Orrenius, S. (2011). Calcium and cell death mechanisms: A perspective from the cell death community [Review]. *Cell Calcium*, *50*(3), 211-221. https://doi.org/10.1016/j.ceca.2011.03.003

APPENDIX A

SPREADSHEET OF COLLECTED ARTICLES

[Consult Attached Files – “AppendixA-Spreadsheet_of_collected_articles.xlsx”]

Microsoft Excel is needed to open the file.

APPENDIX B

KER DESCRIPTION PAGES

[Consult Attached Files – “AppendixB-KER_Description_pages.pdf”]

APPENDIX C

PYTHON SCRIPT MODEL CODE

[Consult Attached Files – “AppendixC-Python_Script_Model_Code.pdf”]

APPENDIX D

TOTAL LIST OF VARIABLES

[Consult Attached Files – “AppendixD-List_of_Dependent_Variables_And_Parameters.pdf”]